

**CHARACTERIZING THRUST PERFORMANCE FOR FREE AND CONFINED  
OSCILLATING CANTILEVERS**

by

**Andrew Stephen Eastman**

B. S. in Mechanical Engineering, Seattle University, 2007

M. S. in Mechanical Engineering, University of Pittsburgh, 2013

Submitted to the Graduate Faculty of  
Swanson School of Engineering in partial fulfillment  
of the requirements for the degree of  
Doctor of Philosophy in Mechanical Engineering

University of Pittsburgh

2013

UNIVERSITY OF PITTSBURGH  
SWANSON SCHOOL OF ENGINEERING

This dissertation was presented

by

Andrew Stephen Eastman

It was defended on

November 22, 2013

and approved by

Ming King Chyu, PhD, Department Chair  
Department of Mechanical Engineering and Materials Science

Laura A. Schaefer, PhD, Associate Professor  
Department of Mechanical Engineering and Materials Science

Anirban Jana, PhD, Senior Scientific Specialist  
Pittsburgh Supercomputing Center, Carnegie Mellon University

Dissertation Director: Mark L. Kimber, PhD, Assistant Professor  
Department of Mechanical Engineering and Materials Science

Copyright © by Andrew Eastman

2013

# **CHARACTERIZING THRUST PERFORMANCE FOR FREE AND CONFINED OSCILLATING CANTILEVERS**

Andrew Stephen Eastman, PhD

University of Pittsburgh, 2013

Although not identical to the motion employed by nature's swimmers and flyers, the simple harmonic oscillations of cantilever-like structures have been shown to provide efficient low power solutions for applications ranging from thermal management to propulsion. However, in order to quantify their true potential, the resulting flow field and corresponding thrust must be better understood. In this experimental work, thin, flexible cantilevers vibrating in their fundamental mode are analyzed in terms of the flow field produced and the thrust generated. The actuation is achieved via a piezoelectric patch mounted near its base. An oscillating voltage tuned to the first resonance of the structure causes vibrations at the free end of the cantilever. The flow field is experimentally measured using Particle Image Velocimetry (PIV). Two dimensional flow fields are extracted from multiple  $x$ - $y$  and  $y$ - $z$  planes, and revealed that inward flow occurs upstream as well as above and below the flat face of the cantilever. It was also found that there is a net inward volumetric flow at the corners of the cantilever. Observing the flow off the tip of the fan lead to the finding that the dominant flow velocity occurs not at the center of the fan, but at the midpoints between the center and each edge. The flow field data are primarily used to motivate future geometry, and boundary configurations that could greatly enhance the thrust capabilities of the cantilever by directing the flow downstream in a more effective manner. The thrust produced was experimentally measured using a high resolution scale. Clear trends were observed and correlations developed to help predict the thrust as a function of the operating



parameters including the cantilever geometry and vibration amplitude and frequency. Attempts at shaping the flow were investigated by introducing sidewalls on both sides of the oscillating cantilever. The sidewall boundary condition was tested with thrust performance and power consumption in mind, and it was found that the position of the tip on the cantilever in relation to the edge of the sidewall has an effect on power consumption that is dramatic and incongruent with what one would expect. This research provides the critical experimental analysis to gauge the viability of using simple and energy efficient actuation from cantilever-like structures in place of more complicated solutions which attempt to maintain a higher degree of biomimicry.

## TABLE OF CONTENTS

<b>PREFACE.....</b>	<b>XIX</b>
<b>1.0 INTRODUCTION.....</b>	<b>1</b>
<b>1.1 PROPULSIVE MOTION .....</b>	<b>2</b>
<b>1.1.1 Undulatory Motion .....</b>	<b>3</b>
<b>1.1.2 Foils .....</b>	<b>4</b>
<b>1.1.3 Oscillatory Motion .....</b>	<b>5</b>
<b>1.2 OSCILLATING CANTILEVERS .....</b>	<b>7</b>
<b>1.2.1 Oscillating Cantilevers from Piezoelectric Actuation .....</b>	<b>7</b>
<b>1.2.2 Fan Array Interaction .....</b>	<b>9</b>
<b>1.2.3 Connection to Cooling Performance.....</b>	<b>10</b>
<b>1.2.4 Flow Analysis .....</b>	<b>12</b>
<b>1.2.5 Piezoelectrics for Propulsion .....</b>	<b>15</b>
<b>2.0 FLOW FIELD ANALYSIS .....</b>	<b>18</b>
<b>2.1 GENERAL EXPERIMENTAL SETUP AND PROCEDURE .....</b>	<b>18</b>
<b>2.2 PARTICLE IMAGE VELOCIMETRY (PIV) SETUP.....</b>	<b>23</b>
<b>2.3 CENTERLINE X-Y PLANE ANALYSIS .....</b>	<b>27</b>
<b>2.4 OFF CENTERLINE MULTIPLE PLANE ANALYSIS.....</b>	<b>35</b>
<b>2.5 STREAMLINES AND VORTEX PROPAGATION .....</b>	<b>44</b>

2.6	INLET AND OUTLET FLOW .....	57
2.7	CONCLUSION .....	63
3.0	THRUST MEASUREMENT CHARACTERIZATION .....	65
3.1	EXPERIMENTAL SETUP AND PROCEDURE.....	66
3.2	THEORY AND DATA ANALYSIS.....	69
3.3	EXPERIMENTAL RESULTS .....	72
3.4	CONCLUSION .....	80
4.0	CHARACTERIZATION OF VISCOUS DAMPING.....	81
4.1	SIDEWALL SETUP AND PROCEDURE.....	81
4.2	THEORY .....	84
4.3	EXPERIMENTAL RESULTS .....	86
4.4	CONCLUSION .....	96
5.0	SIDEWALL POSITIONING FOR THRUST ENHANCEMENT .....	98
5.1	SIDEWALL THRUST MEASUREMENT PROCEDURE .....	98
5.2	THRUST ENHANCEMENT WITH SIDEWALLS.....	101
5.2.1	Sidewall Gap Spacing.....	101
5.2.2	Tip Extension Distance.....	104
5.3	CONCLUSION .....	111
6.0	FINAL REMARKS.....	113
6.1	FUTURE WORK.....	114
APPENDIX A .....		116
APPENDIX B .....		122
BIBLIOGRAPHY.....		128

## LIST OF TABLES

Table 1: The translational velocity and direction of the vortex path. ....	29
Table 2: Maximum $x$ , $y$ and overall velocity in the flow field for each amplitude.....	35
Table 3: The relevant dimensions and operating parameters of all of the piezoelectric fans investigated. ....	65
Table 4: List of the default PIV image capture settings.....	117

## LIST OF FIGURES

Figure 1: An illustration of the undulatory and oscillatory motions found in aquatic propulsion from Tyell [19].....	2
Figure 2: Typical motion of a foil from Schouveiler et al. [24]. Notice that the foil undergoes a translational undulatory motion along with a local flapping oscillation.....	4
Figure 3: A picture from Kimber et al. [43] demonstrating two fan interaction orientations: face-to-face and edge-to-edge.....	9
Figure 4: General layout and dimensions of the piezoelectric fan.....	19
Figure 5: Mode shape of the piezoelectric fan normalized by the maximum (tip) vibration amplitude.....	20
Figure 6: Oscillatory motion of the piezoelectric fan tip as a function of time. The amplitude is normalized by the maximum (tip) vibration amplitude .....	20
Figure 7: Representation of the gap that occurs in this type of motion .....	22
Figure 8: Representation of the component orientation.....	23
Figure 9: Illustration of the two layouts used in capturing the flow field. The left illustration captures the y-z flow field and the right captures the x-y flow field .....	25
Figure 10: Illustration of the shadowing effect of the laser sheet.....	26

Figure 11: Two-dimensional flow field and full-field vorticity for $A = 4$ mm and phase equal to (a) $90^\circ$ , (b) $105^\circ$ , (c) $120^\circ$ , (d) $135^\circ$ , (e) $150^\circ$ , and (f) $165^\circ$ . .....	28
Figure 12: Vortex paths for $A =$ (a) 4 mm, (b) 3.5 mm, (c) 3 mm, (d) 2.5 mm and (e) 2 mm. The vortex is tracked over the phase range displayed on each graph. The error bars are based on the statistical averages of experiments repeated 50 times. ....	30
Figure 13: Maximum vorticity for each amplitude with respect to phase angle of the fan. ....	31
Figure 14: Vorticity plots of $A =$ 4 mm, 3.5 mm, 3 mm and 2.5 mm. Normalized by each corresponding maximum vorticity.....	32
Figure 15: Cycle averaged flow fields determined from 1250 captures over one full period for $A =$ (a) 4 mm, (b) 3.5 mm, (c) 3 mm, (d) 2.5 mm and (e) 2 mm.....	34
Figure 16: Cycle-averaged $U_x$ along the $z$ -axis in the $x$ - $y$ plane for different $z$ values: (a) 1 mm, (b) 2 mm, (c) 3 mm, (d) 4 mm, (e) 5 mm and (f) 6 mm. The solid dark lines represent the fan at phase angles of 0 (non-displaced position) and 90 degrees (maximum displacement). ....	37
Figure 17: Cycle-averaged velocity vectors in the $y$ - $z$ plane at different $x$ positions.(a)-8 mm, (b)-6 mm, (c) -4 mm, (d) -2 mm, (e) 0 mm and (f) 2 mm. The solid dark lines represent the fan at phase angles of 0 (non-displaced position) and 90 degrees (maximum <i>local</i> displacement). The velocity magnitude indicator is uniform for (a) through (f) and shown in (a). ....	40
Figure 18: Instantaneous velocity vectors in the $y$ - $z$ plane at $x = 0$ mm and a phase of 255 degrees. ....	42

Figure 19: Volumetric flow rate along a half cycle of the oscillation amplitude with respect to the $x$ location of the $y$ - $z$ plane. Positive indicates flow toward the centerline of the piezofan.	43
Figure 20: General representation of a potential sidewall geometry based on the analyzed data. The dashed lines represent the approximate operational area of the piezofan.	44
Figure 21: Streamlines over the piezofan with origins 8 mm above the face of the fan. (a) is above the face of the fan looking down and (b) is beside the fan looking across the face.	45
Figure 22: Streamlines over the piezofan with origins upstream of the flow. (a) is above the face of the fan looking down and (b) is beside the fan looking across the face.	47
Figure 23: Streamlines over the piezofan with origins at 5 mm from the center of the fan. (a) is above the face of the fan looking down and (b) is beside the fan looking across the face.	48
Figure 24: The $y$ - $z$ plane (at $x = -8$ mm) flow field at different oscillation phases. From top left to bottom right, the phases are (a) 120, (b) 150, (c) 180, (d) 210, (e) 240, and (f) 270 degrees.	50
Figure 25: The $y$ - $z$ plane (at $x = -4$ mm) flow field at different oscillation phases. From top left to bottom right, the phases are (a) 120, (b) 150, (c) 180, (d) 210, (e) 240, and (f) 270 degrees.	51
Figure 26: The $y$ - $z$ plane flow field at $x = -2$ mm (top) and $x = 0$ mm (bottom) for different oscillation phases. From left to right, the phases are (a & d) 120, (b & e) 150, and (c & f) 180 degrees.	52

Figure 27: Location of the vortex center at different phase steps. The black line represents the fan blade.....	53
Figure 28: The $x$ - $y$ plane (at $z = 1$ mm) flow field at different oscillation phases. From top left to bottom right, the phases are (a) 120, (b) 150, (c) 180, (d) 210, (e) 240, and (f) 270 degrees. ....	54
Figure 29: The $x$ - $y$ plane (at $z = 3$ mm) flow field at different oscillation phases. From top left to bottom right, the phases are (a) 120, (b) 150, (c) 180, (d) 210, (e) 240, and (f) 270 degrees. ....	55
Figure 30: The $x$ - $y$ plane (at $z = 5$ mm) flow field at different oscillation phases. From top left to bottom right, the phases are (a) 120, (b) 150, (c) 180, (d) 210, (e) 240, and (f) 270 degrees. ....	56
Figure 31: Flow velocity of $U_x$ at $y = 0$ with varying $x$ distances away from the tip of the fan blade.....	58
Figure 32: Comparison of the volumetric flow rate in the $z$ -direction (positive is towards the fan) with a control surface that is (a) the oscillation envelope and (b) the entire flow field domain.....	59
Figure 33: Volumetric flow rate in the $z$ -direction (positive is towards the fan) based on an increasing inspection domain in the $y$ -direction. ....	61
Figure 34: Geometrical representation of a sidewall that would block only the flow lost over the sides of the fan blade.....	62
Figure 35: The cycle averaged flow field in the $y$ - $z$ plane for $x = -4$ mm. This demonstrates how the volumetric flow rate minimum corresponds to the vortex position. The dotted red line represents the inspection domain for the volumetric flow rate minimum. ....	63



Figure 36: Visual representation of the size and shape of all the fans used for thrust measurements.....	66
Figure 37: Graphical representation of the orientation and position of the thrust measurement setup. ....	68
Figure 38: Comparison of the previously collected data from [70] and the new data.....	72
Figure 39: Thrust data for each fan compared to their respective amplitude ranges. ....	73
Figure 40: The non-dimensional thrust for each fan compared to their respective amplitude ranges. ....	74
Figure 41: The non-dimensional thrust with the curve fit using Reynolds and Strouhal numbers. ....	76
Figure 42: The non-dimensional thrust with the curve fit using the Keulegan-Carpenter number only. ....	77
Figure 43: Non-dimensional thrust as function of Keulegan-Carpenter number. ....	78
Figure 44: Schematic illustrating orientation of the sidewalls to the fan blade.....	82
Figure 45: Comparison of the normalized amplitude response for the (a) $V = 17.5$ Vrms and (b) $V = 32.5$ Vrms case. ....	87
Figure 46: The progression of the natural frequency as the sidewall gap is varied.....	88
Figure 47: The quality factor for each sidewall gap distance. ....	89
Figure 48: Curve fit of the quality factor that has been normalized by the isolated quality factor. ....	90
Figure 49: The power requirement of the piezoelectric fan at 61 Hz as the gap is varied. ....	91
Figure 50: The current as a function of sidewall gap for set voltage inputs.....	92

Figure 51: The phase difference between the current and voltage input at 61 Hz for a set voltage inputs.....	93
Figure 52: The phase lag between the voltage and current input as a function of frequency for a voltage input of 17.5 Vrms. ....	94
Figure 53: The maximum oscillation amplitude for each sidewall gap distance.....	95
Figure 54: The power requirement to the piezoelectric fan with a fixed amplitude as the frequency is changed within the bandwidth.....	96
Figure 55: Thrust force as a function of the gap distance for three fixed amplitudes. ....	102
Figure 56: Power as a function of gap distance for three fixed amplitudes.....	103
Figure 57: Efficiency of thrust as a function of gap distance for three fixed amplitudes.....	104
Figure 58: Thrust as a function of tip extension for a fixed amplitude of $A = 5$ mm. The horizontal line indicates the thrust generated in the absence of sidewalls.....	106
Figure 59: Power as a function of tip extension for a fixed amplitude of $A = 5$ mm. The horizontal dashed line represents the power consumption at a no sidewall effect condition. ....	107
Figure 60: Voltage as a function of tip extension for a fixed amplitude of $A = 5$ mm. ....	108
Figure 61: Current as a function of tip extension for a fixed amplitude of $A = 5$ mm.....	108
Figure 62: Phase as a function of tip extension for a fixed amplitude of $A = 5$ mm. ....	109
Figure 63: Efficiency of thrust as a function of tip extension for a fixed amplitude of $A = 5$ mm. ....	111
Figure 64: An image of a proper seeding particle density obtained with a smoke pen. ....	119
Figure 65: Image of a good velocity vector field resulting from a satisfactory density of seeding particles. ....	121

Figure 66: Comparison of the repeatability uncertainty (b) to the vorticity (a) in the $x = -2$ mm velocity field. The both of the colorbars have units of $1/s$ indicating vorticity. ....	125
Figure 67: Comparison of the precision error (b) to the vorticity (a) in the $x = -2$ mm velocity field. The both of the colorbars have units of $1/s$ indicating vorticity. ....	126
Figure 68: The representation of the combined repeatability and precision error in the $x = -2$ mm velocity field. The colorbar has units of $1/s$ indicating vorticity. ....	127

## NOMENCLATURE

$A$	tip oscillation amplitude
$A_{max}$	maximum tip oscillation amplitude
$A_{local}$	local vibration amplitude
$c$	structural damping coefficient of the cantilever
$c_a$	aerodynamic damping coefficient
$D$	width of the cantilever
$F_o$	force on the oscillating cantilever
$I$	current (rms) input to the piezoelectric fan
$k$	spring constant of the cantilever
$KC$	Keulegan-Carpenter number Eq. (10)
$L_b$	length of exposed portion (i.e., not covered by piezoelectric patch) of cantilever
$L_p$	length of the piezoelectric patch
$L$	total length of the Mylar blade
$m$	effective mass of the cantilever
$m_a$	mass of the air
$Q$	structural quality factor
$Q_a$	aerodynamic quality factor

$Q_{air}$	quality factor in air (combined structural and aerodynamic effects)
$Q_{iso}$	isolated quality factor in air (i.e., when no sidewalls are affecting the fan)
$Re_A$	oscillating Reynolds number, Eq. (1)
$St$	Strouhal number Eq. (8)
$t_b$	thickness of the cantilever
$t_p$	thickness of the piezoelectric patch
$T$	thrust force
$T^*$	non-dimensional thrust force
$U$	flow velocity
$u$	maximum tip velocity
$V$	voltage input to the piezoelectric fan

### **Greek Symbols**

$\delta$	distance between the wall and side edge of the cantilever
$\varepsilon$	downstream distance the tip of the fan extends beyond the sidewalls
$\eta$	efficiency based on the thrust to power ratio (Eq.(25))
$\mu$	dynamic viscosity (air)
$\nu$	fluid kinematic viscosity (air)
$\phi$	phase lag between the voltage and current input
$\omega$	oscillation frequency
$\omega_{n,air}$	resonance frequency in air
$\omega_n$	resonance frequency
$\zeta$	structural damping ratio
$\zeta_{air}$	structural damping coefficient in air

## Subscripts

$x$	x-direction
$y$	y-direction
$z$	z-direction

## **PREFACE**

I would like to thank my committee for dedicating their time and expertise to make my research the best that it can be. I would also like to thank Eric Thorhauer and Jacob Keifer for their contributions to this work.

## **1.0 INTRODUCTION**

The study of propulsion mechanisms in nature has been ongoing for many decades. This has occurred for both flight in air [1-3] and swimming in water [4-10]. Despite the large interest in how creatures in nature travel, it has never been completely replicated in a laboratory setting. However, this has not stopped researchers from attempting to build comparable analogs in order to test their competency [11-16]. Despite a less than complete understanding, the knowledge that has been gathered has been monumental in furthering advances in other areas. For example, Whittlesey et al. [17] employed the method that fish use when they swim in schools to make improvements in the area of wind turbine farm design. The new proposed configuration with vertical axis wind turbines was found to theoretically provide an order of magnitude increase in power output over currently in place horizontal axis wind turbine farms. Vatanabe et al. [18] used the same concept of fish swimming patterns to optimize biomimetic pumps.

Additionally, the categorization and analysis of the various modes of aquatic locomotion conducted by Sfakiotakis et al. [6] gives a good starting point for the proposed research. In his research, Sfakiotakis breaks down aquatic movement to two main categories: undulatory and oscillatory. The aquatic life that was studied was found to range between the two types of motion in varying degrees. Often, some would exhibit both forms depending on the given conditions. Undulatory motion was found to be exceptional for fast acceleration while oscillatory motion was seen to be the most efficient for maintaining continuous speeds. The fact that transportation



methods found in nature tend to be quite efficient and/or effective has led to quite a bit of research in an attempt to replicate and harness it. The aim of the presented work is to investigate the propulsion capabilities of the simplified structure and motion of an oscillating cantilever rather than attempt to mimic the complex mechanism involved in complete biomimicry. In the remainder of this chapter, the background behind aquatic and aerial motion is presented along with a summary of related studies involving thermal or fluid aspects of oscillating cantilevers.

## 1.1 PROPULSIVE MOTION

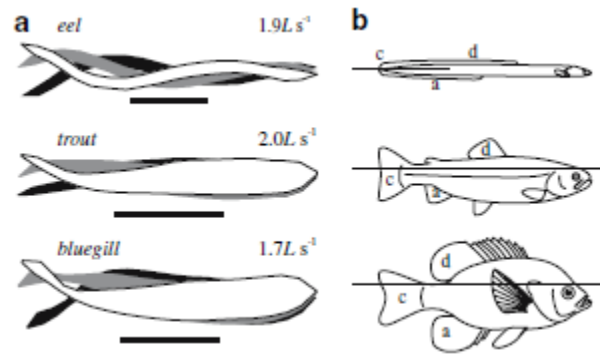


**Figure 1: An illustration of the undulatory and oscillatory motions found in aquatic propulsion from Tyell [19].**

In order to understand the efficacy of the proposed type of propulsion in this work, it is key that a good understanding of all major forms of biomimicry type locomotion methods are developed. Much like the designation of undulatory and oscillatory motion in fish, propulsion methods break down into traveling waves (undulatory motion) or a flapping fin (oscillatory motion). Triantafyllou et al. has provided two reviews in the undulatory type of propulsion: the first being a brief overview of studies and analysis into the hydrodynamics at work [20] and the second

being a very thorough review focusing on biomimetic foils [21]. The second paper was completed in 2004 concluding that although there have been many advances; there was much that remains uncertain about replicating aquatic propulsion.

### **1.1.1 Undulatory Motion**

Kosa et al. [22] studied a propulsion method that subjects individual portions of a cantilever to the same frequency of oscillation at different phases. This allowed them to create a traveling wave that generates thrust to propel their structure underwater. Their experimental model was able to achieve a propulsive thrust of 0.04 mN which allowed a maximum speed of 5 cm/s. Rather than construct a complicated system that required precise control, Behkam et al. [23] decided to create a rigid helical structure that rotated in order to produce that undulatory motion. Analytical models were developed for a traveling wave type propulsion system as well, but it was not brought to the experimental stage. Their experimental model for the helical wave propulsion outperformed their theoretical model, reaching nearly 14 mN of thrust at an 8 Hz operating frequency. Their experimental model was approximately 5 cm in length. A similar study was conducted by Edd et al. [11] with an analytical model using arrays of helically shaped carbon nanotubes. It is yet to be seen whether this can be replicated experimentally once the state of carbon nanotube technology catches up to these theoretical designs.

Low et al. [16] used shape memory alloys (SMA) in order to replicate undulatory motion. The shape memory alloy was controlled in three segments by applying current at each location to get the desired temperature change to cause flexure in the SMA. It was found that allowing for adequate cooling of the SMA was a limiting factor in operation. This effect would be assisted by the device actually moving through the water, providing some amount of convective cooling. It

was also determined that more individually operated sections would allow for a higher effectiveness due to the increase in time between necessary heating of the SMA. However, just like other undulatory based systems that use active control of the motion, the control mechanism is very complicated and would increase in complexity as more segments were added. This is even more amplified by a system that relies on allowing a proper cooling time in order to operate effectively

### 1.1.2 Foils

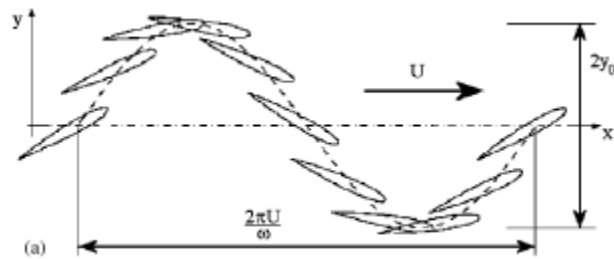


**Figure 2: Typical motion of a foil from Schouveiler et al. [24]. Notice that the foil undergoes a translational undulatory motion along with a local flapping oscillation.**

Oscillating foil technology exists between the oscillatory and undulatory regime. The path of the foil in water is a sine wave which classifies it as undulatory. However, the foil undergoes a local flapping oscillation such that if the translational velocity were zero, it would be classified as oscillatory. A graphical representation can be seen in Figure 2. The appeal of this type of propulsion is that propulsive efficiencies are very high [25] as well as combining the benefits of both translational and oscillatory motion.

With the type of movement that makes an oscillating foil work, there are a multitude of parameters that effect performance. Anderson et al. [25] determined optimal conditions based on the Strouhal number, heave-to-chord ratio, angle of attack, and the angle between heave and pitch. The maximum propulsive efficiency that they were able to obtain was 87%, which is in line with that found in nature. However, this is a higher efficiency than what was found via experimentation by Read et al. [26]. It was also found that the motion produced a reverse Karman Vortex Street. Schouveiler et al. [24] examined the effect of the Strouhal number on propulsive performance as well. They also found a mechanism of generating a sideways force in order to enable maneuvering. Young and Lai [27] used a numerical model to determine that Strouhal number was not sufficient in effectively characterizing propulsive efficiency.

Heathcote et al. [28] analyzed a flapping airfoil with a fin attached to the trailing edge. They found that the thrust was not only dependent upon the frequency and amplitude, but the mode shape (altered by the fin flexibility). Whether the mode shape produces such a pronounced increase in thrust once the translational motion is removed is uncertain. A more flexible foil will produce a mode shape that is increasingly parabolic in nature. The translational motion could have the effect of damping the negative effects of a higher mode shape (i.e. flow in the opposite intended direction) while enhancing the positive effects.

### **1.1.3 Oscillatory Motion**

Shape memory alloys have been a popular choice in achieving the desired operational characteristics in oscillatory motion, due to their high stress capabilities [29]. Garner et al. [30] developed a computational model to analyze its effectiveness. Their final outcome was an entire system consisting of a shape memory alloy material so that a desired deflection could occur at

any point on the body, but they started with a small section that just moved the tail end. This allowed their model to be validated by an experimental test mimicking the finite element analysis model. It was concluded that this type of actuation is quite effective in producing a large amount of actuation power. Rediniotis et al. [31] continued that research with a slightly more complex version. Their control scheme allowed an operational frequency of up to 20 Hz. They were also able to produce a small traveling wave along the body of the system.

Zhang et al. [13] also used a shape memory alloy to oscillate a fin shaped cantilever in order to drive the motion of a fish-type analog. They concluded that, although there was some fine tuning required, their model performed well. Suleman and Crawford [32] took this even further and made the entire model resemble a tuna. They were able to reduce the complexity using an adaptive structure model. As with other attempts at biomimetic propulsion the control system was found to be a major limitation.

There have also been underwater propulsion prototypes using completely mechanical actuation. Yu et al. [14] designed a model that used four separate actuators that drove a fish tail shaped fin. Although the mechanism simply oscillated with a curvature, modulating the speed through the oscillation allowed the control of direction as well as speed. Work done by Tan et al. [12] used a much simpler form with only a single actuation point. Their main goal was to analyze the flow that was generated by the tail fin itself.

The main drawback to these attempts at replication of what we see in nature is that it tends to yield a very complicated or power sensitive process. Undulatory motion requires many individually operating segments. Each segment requires a control scheme that can not only operate individually, but also adapt and respond to the changing environment and adjoining segments. Shape memory alloys have the potential to provide large amounts of thrust power, but

the control system would have to be able to actively adjust to the cooling conditions in the surrounding area. Purely mechanical operation would allow for an easily scalable response, but it is very power hungry compared to active material options. Additionally, attempts to accurately replicate even the simple oscillatory motion of a fish are very complicated and may not be viable on an application scale. It is with this in mind that justification exists for using simple oscillating cantilevers as the primary thrust component. The actuation can be very energy efficient and is relatively simple to implement.

## **1.2 OSCILLATING CANTILEVERS**

Oscillating or vibrating cantilevers have many useful applications in the areas of biosensors [33], atomic force microscopes [34], flow sensors [35], and rheological measurements [36]. Typically, the classic engineering problem of predicting the motion of a vibrating cantilever neglects the fluid structure interaction. However, this interaction is not always negligible and the inclusion of it in analysis increases the complexity tremendously. Consequently, as the flow field produced by a vibrating cantilever is of interest to the current research, the fluid structure interaction is non-negligible.

### **1.2.1 Oscillating Cantilevers from Piezoelectric Actuation**

The usage of piezoelectric materials to drive oscillations in a cantilever has been proposed as a low power and simple alternative to the more power hungry and complex mechanical excitation. Toda and Osaka [37] presented the idea of using a Poly-Vinylidene Fluoride (PVF2) type

piezoelectric material to induce vibration in a cantilever in 1979. Their intended application was electronics cooling due to their low power requirement and simple structure. Yarinaga et al. [38] tested a Lead Zirconate Titanate (PZT) piezoelectric material attached to a fan. Sheu et al. [39] investigated the influence of the bonding material on the vibration characteristics. Using a lumped-mass analytical model that was verified with experiments, Yao and Uchino [40] predicted the tip deflection and behavior of a piezoelectric bimorph based on the physical characteristics. Ergin and Ugurlu [41] developed a numerical model for the response of a cantilever when a surrounding fluid is taken into account.

In order to determine the pressure and flow rate characteristics of these oscillating cantilevers, Kimber et al. [42] analyzed two different cantilever sizes and materials (Mylar and steel) in an enclosed box with well-defined inlet and outlet regions for the surrounding air. It was found that the Mylar blade, operating at its largest amplitude, exhibited the highest flow rate while the steel blade, also operating at its largest amplitude, gave the highest static pressure. An interesting finding is that the maximum flow rate for the steel and Mylar blades are only different by 20% while the pressure difference is over twofold. This is even more interesting considering that the maximum amplitude of the steel blade is 40% lower than the Mylar blade. It is implied that it may be due to the higher oscillation frequency employed by the steel blade. The distance of the fan blade to the enclosure walls was also considered. It was found that when the enclosure walls that were above and below the face of the blade were removed, the performance increased. This indicates that the oscillating cantilever draws flow from above and below the blade in addition to just upstream. However, the impact of these variables on thrust was not investigated.

### 1.2.2 Fan Array Interaction

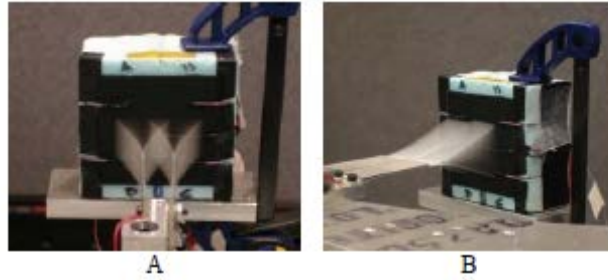


**Figure 3: A picture from Kimber et al. [43] demonstrating two fan interaction orientations: face-to-face and edge-to-edge.**

The potential for a beneficial interaction between cantilever blades is a point of interest for future research. In 1994, Ihara and Watanabe [44] observed the interaction between two mechanically oscillating cantilevers oriented such that the flat surface of each slender cantilever faced the other (this orientation is also commonly referred to as “face to face”). They operated the fans such that their motion was in-phase or counter-phase with each other. The distance between the plates was altered to investigate its impact. It was found that the distance between the plates had an effect only when the oscillation of the two cantilevers was counter-phase. In that case, they found that their mean flow velocity nearly doubled.

Kimber et al. [43, 45] continued this analysis by looking at not only a face-to-face orientation, but edge-to-edge as well. The heat transfer implications were also explored. When the vibration amplitude was measured, it was found that the fan interaction contributed to as large as a 40% increase in vibrational amplitude without any additional power requirement. In order to isolate the contributing factors to the added amplitude, the tests were also conducted in a vacuum chamber. The results indicated that the change in amplitude is almost entirely due to the



fluid interacting with the beams, initiating a change in viscous damping. With the two oscillating cantilevers close enough to interact, it was found that the face-to-face orientation benefited from an in-phase operation while the edge-to-edge orientation benefited to a counter phase operation.

Shoemaker [46] also investigated the effect of piezoelectric fans operating in arrays. Two different styles were chosen: inline (each row directly behind the other) and staggered (each row offset such that the piezoelectric fan was between the two in front of it). It was found that, as the fans in each row were placed closer together, the static pressure increased while the flow rate decreased for both the staggered and inline arrays. However, there is a potential problem with these results. The mounting system that was used was a post that appears to occupy the width of the upstream flow of the fan. As the separation distance between the fans decreases, it is expected that the pressure loss from these obstructions will increase. It is not explicitly stated that this effect has been accounted for. Due to the limited amount of static pressure the fans produce, it is apparent that this oversight could completely change the overall conclusion.

### **1.2.3 Connection to Cooling Performance**

One of the most popular applications for piezoelectrically oscillating cantilevers is in electronics cooling due to their low power requirements, scalability, and simple structure. Although not a direct correlation, in many cases a higher forced convection heat transfer coefficient through increased flow production can be assumed to result in a higher thrust production as well. As mentioned before, the paper by Toda and Osaka [37] was one of the first to propose the use of vibrating cantilevers for electronics cooling. Now that current consumer electronics have become more space restricted and power sensitive, cooling solutions have had to move away from

traditional rotary fans with large heat sinks. Piezoelectrically oscillating cantilevers have been one of the solutions to fill the void.

Although there was no actual heat transfer analysis, Yoo et al. [47] developed several blade geometries in order to analyze frequency, amplitude, and flow velocity for the purposes of heat transfer applications. They found a linear relationship between the oscillation amplitude and flow velocity when operated at 60 Hz. It was also found that the maximum flow velocity was greatest for a phosphor bronze material which has the lowest Poisson's ratio and highest Young's modulus.

Acikalin et al. [48] analyzed the flow fields and heat transfer capabilities of simple rectangular piezoelectric fans in various orientations. They also placed the piezoelectric fan in a cellular phone and laptop size enclosure in order to quantify the effectiveness in a very space limited environment. At steady state, the maximum convective heat transfer coefficient was nearly  $105 \text{ W/m}^2\text{K}$  when the piezoelectric fan was placed with the tip at the center and oscillating parallel to the heat source. This magnitude of heat transfer coefficient is an order of magnitude increase over natural convection and therefore illustrates the viability of using piezoelectric fans for cooling.

More fan to heat source orientations were investigated by Acikalin et al. [49] including impingement flow. They also conducted a numerical simulation that had mixed results compared to experimental. This was mainly attributed to the fact that the numerical model is two dimensional while the experiment has three dimensional flow field components to it. Resonance frequency also played a very significant role in heat transfer performance as they found that a 5% deviation from the natural frequency decreased their temperature drop by 30%.

Wait et al. [50] considered the flow potential for a piezoelectric fan operating up the 4<sup>th</sup> resonance mode. This included a numerical analysis of the mode shapes of three different blade lengths as well as the flow visualization. It was found that power requirements increase dramatically when operating at higher resonance modes due to losses in the piezoelectric. There is also a sacrifice in flow at the tip of the fan blade due to a decrease in vibrational amplitude.

A more recent experimental study by Kimber and Garimella [51] found that the maximum heat transfer performance of a vibrating cantilever can be broken down in terms of oscillation frequency and amplitude (excluding spacing and orientation). This means that the width and length of the fan do not contribute to the magnitude of the convective heat transfer rate. They also determined that the oscillation frequency contributes slightly more to thermal performance than amplitude. Due to the applicability of thermal performance to thrust performance, similar efforts have been made in the current research to quantify the thrust based on the oscillation frequency and amplitude much in the same manner.

#### **1.2.4 Flow Analysis**

Understanding the flow that is generated by oscillating cantilevers is a crucial part of completely being able to harness its potential. Kim et al. [52] used particle Image Velocimetry (PIV) to study the flow field of a single, wide oscillating cantilever bounded by two sidewalls. Their operating frequency was 240 Hz with an amplitude of 0.74 to 1.37 mm. This corresponds to a kinetic Reynolds number range of approximately 50 to 180. They observed two counter rotating vortices shed counter phase to each other over each cycle of vibration. This ends up being analogous to a reverse Karman vortex street. The cycle averaged flows revealed a region of high downstream velocity within the oscillation envelop of the tip with a maximum velocity nearly

three times the fan tip velocity. This was a product of the oscillation frequency and amplitude. The location of the highest flow rate was at the center of the cantilever. As such, the numerical research by Choi et al. [53] that was modeled after the experiments in Kim et al. [52] was only of a 2-dimensional flow field. As the flow is confined by sidewalls, it is likely that this is at least one of the contributing factors (along with width) that cause the flow to not have apparent corner interactions.

Extending this research further, Kim et al. [54] developed a wavelet based numerical model that replicates their previous system. It was concluded that their model corresponds well to their experimental results. They determined that the cycle averaged analysis averages out some of the less pronounced phenomenon that is not necessarily pronounced apparent throughout the cycle. This does not preclude the usage of a cycle averaged analysis however. There are many applications, such as thrust generation, that do not necessitate the tracking of small instances of flow phenomena as they would result in little significance to the overall outcome.

In order to gain a better understanding of optimal design and orientation of piezoelectric fans, Acikalin et al. [55] conducted an analytical, numerical, and experimental investigation of the two dimensional flow generated by a piezoelectric fan. They found their theoretical model compared well to their experiments with a few explainable errors. Choi et al. [53] also developed a numerical model that was verified by experimental data. The model included more of a focus on vorticity and vortex formation. This numerical model allowed for a monitoring of pressure within the system, which led to the conclusion that static pressure difference contributes heavily to vortex formation.

Bidkar et al. [56] developed an experimentally verified theoretical model to predict the effect of aerodynamic damping on the oscillation frequency and amplitude of an oscillating

cantilever. In the model, the Keuligan-Carpenter number [57] was varied along with the frequency. Two different blade types were analyzed (Mylar and steel) that presented different operating parameters. Both the theory and experimental results found that a non-linear increase in aerodynamic damping presents with an increase in oscillation amplitude. Their model also presents a worthwhile visualization of the vortex sheets that are developed along the edge of an oscillating flat structure.

Similar to the flow field research conducted by Kim et al. [52, 54], Clemons et al. [58] used PIV to investigate the two dimensional flow fields from a piezoelectrically oscillating cantilever. The fan was placed in a wind tunnel such that the tip was pointing perpendicular to the induced flow. This created a reverse Karman vortex street off the trailing edge of the fan that has been seen in previous research emanating from the tip. Peterson et al. [59] also used PIV to study the flow field produced at the fan tip of an oscillating cantilever. The driving mechanism was an Ionic Polymer Metal Composite (IPMC), but the nature of the motion is the same.

One of the main components of the flow field that are generated by an oscillating cantilever is vortices. They contribute to and give vital information about the performance of many flow generating systems. It was found by Krueger [60] that force produced by the jet was maximized as vortex shedding is decreased. Thus, Dabiri and Gharib [61] have investigated the effect of vortex shedding on propulsion. They demonstrated the conditions for the Kelvin-Benjamin variational principle in a jet setup. A digital particle image velocimetry system was used to map the velocity field produced by a vortex ring generator. The stroke length was increased until the vortex was no longer shed from the nozzle outlet. Thus, they effectively demonstrated that the propulsive thrust can be maximized by limiting vortex shedding. However, it is not reasonable in many cases to attempt to completely remove vortex formation from flow.

Dabiri [62] investigated the possibility of optimal vortex formation criterion. It was proposed as a new basis for further understanding propulsion, particularly biological propulsion.

### **1.2.5 Piezoelectrics for Propulsion**

The amount of research done in terms of piezoelectric fan induced propulsion is limited. Additionally, most of the research has skipped straight to the application phase rather than explore the underlying mechanisms involved. Chung et al. [63] investigated a wide blade driven by two piezoelectric patches. The main application was for generating flight in air. The two piezoelectric patches could be operated independently of one another. Their research confirmed basic assumptions that amplitude is highest when the two piezoelectric patches were operated in phase and at resonance. Ming et al. [64] made use of a fiber composite piezoelectric to drive underwater robots. They measured a maximum propulsive force of 0.33 N from a 110 mm by 42 – 65 mm blade (the blade linearly increased in width from tip to tail). This allowed for a maximum velocity of 325 mm/s which demonstrates that this method of propulsion is viable. Mujherjee and Ganguli [65] developed a theoretical model that attempts to mimic dragonfly wings. Their model also predicts the average lift and thrust produced when operating at the respective parameters found in nature.

Piezoelectrically oscillating cantilevers may not have the means to fully replicate the motion and performance of propulsion in nature, but they have one overriding advantage: simplicity. Their solid state nature makes them easy to manufacture and implement into many applications. This allows them to also be scalable in size as well as efficient in many scenarios. For example, one could create a swarm of independently maneuvering sensing robots to create ocean temperature maps or monitor municipal water systems. Operation is power based,

therefore environmental fluctuations should have minimal effect compared to shape memory alloys. The overarching objective of this research is to provide a comprehensive understanding on the performance characteristics of piezoelectric fans and how to promote thrust enhancement. This is a fundamental step needed to adequately expand the consideration of their potential applications.

The main contributions of this thesis are:

- A greater understanding of the three dimensionality of the flow field that is dominant when the length is comparable to its width.
  - This will help determine the inlet and outlet areas of flow for better boundary positioning.
  - This will show the progression and effect of the vortices on the flow field.
- An understanding of the thrust potential for oscillating cantilevers based on the oscillation frequency, maximum tip amplitude and geometric properties.
  - This will allow for future studies to be able to choose a cantilever and operational settings to get the desired results before extensive testing.
- Fundamental insight into the viscous damping that occurs when boundaries are introduced which impede flow off of the side of the cantilever (normal to the oscillation path of the cantilever).
  - This will provide information on the extra power that is required to operate within the presence of boundaries.
  - This will demonstrate when boundaries have a non-negligible effect on the cantilever operation.

- The effect of sidewall placement on thrust force and the required power consumption
  - This will provide an understanding of the optimal placement of sidewalls for both maximum thrust and efficiency.
  - The placement for low power consumption will assist with other applications such as electronics cooling.

The remainder of this thesis is organized as follows. Chapter 2 presents the flow field analysis for multiple planes in order to give an idea of the three dimensional flow. This provides motivation for defining inlet and outlet regions of the oscillating cantilever in a manner where thrust can be enhanced. Chapter 3 presents a characterization of thrust production based on multiple oscillating cantilever sizes and operational characteristics. Chapter 4 investigates viscous damping effects and power requirements when sidewalls are introduced to the system. Chapter 5 then takes all of the previous information and applies it to sidewall positioning to determine the effect on thrust. Finally, chapter 6 presents the concluding remarks that seek to succinctly explain the findings in this work.



## 2.0 FLOW FIELD ANALYSIS

The first step in this work was to gain a more comprehensive understanding of the flow field that is produced by oscillating cantilevers whose length is comparable (on the same order or magnitude) to its width. This is to allow for a more intelligent application of thrust enhancement methods once boundaries (e.g., sidewalls) are introduced. The following is a general experimental setup and procedure for the main cantilever used in this work followed by the results obtained from Particle Image Velocimetry (PIV) analysis.

### 2.1 GENERAL EXPERIMENTAL SETUP AND PROCEDURE

Although different cantilever geometries were used at certain points in this work, the main type of oscillating cantilever used in this study is a commercially available piezoelectric fan (i.e. piezofan) from Piezo Systems (RFN1-005) and illustrated in Figure 4. Piezofans can generally be defined using the following geometric parameters: It consists of a thin Mylar blade of uniform thickness ( $t_b$ ) of 0.3 mm, width ( $D$ ) of 12.7 mm, and total length ( $L$ ) of 64.9 mm with the exposed length ( $L_b$ ) being 36.5 mm. The cantilever is actuated by a lead Zirconate Titanate (PZT) bimorph affixed to the blade at the mounting base. The dimensions of the PZT patch are thickness ( $t_p$ ) and length ( $L_p$ ) of 0.6 mm and 32.0 mm respectively. The PZT patch creates a moment at the base of the cantilever leading to large vibration amplitudes at the tip (free end of

the cantilever). A mounting bracket (supplied with the unit from the vendor) is fixed to the base of the fan which allows for a secure method of attaching the piezoelectric fan to a variety of surfaces.

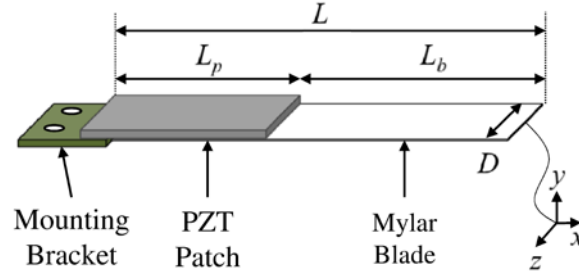


**Figure 4: General layout and dimensions of the piezoelectric fan**

The mode shape and tip response of the piezofan fan are provided in Figure 5 and Figure 6, respectively. Note that the displacements are relatively small in the region covered by the piezoelectric patch due to its greater stiffness. In the exposed blade region ( $0 < x < 36.5$  mm), the mode shape is similar (although not identical) to a standard cantilever beam. The displacement signal at the tip ( $x = 0$ ) is nearly perfectly modeled with a sinusoid waveform. The data in Figure 6 is taken from a driving signal of 61 Hz and 53 Vrms. The amplitude is measured using a laser displacement sensor (Keyence LK-G157) positioned to target the tip of the fan on the centerline (the origin, as shown in Figure 4) with the laser oriented parallel to the y-axis. The flow that is produced is exclusively due to the oscillatory motion of the fan. The oscillation is accomplished by subjecting the piezoelectric material to an AC signal produced by a function generator (Tektronics AFG 3102). This causes the piezoelectric material to expand and contract. By tuning the input frequency to the fundamental frequency of the piezofan, the small movement of the patch causes large oscillations at the free end of the cantilever blade. The magnitude of this AC

signal is quite large ( $\sim 120$  V) due to the requirements of the PZT material. This is accomplished by routing the function generator signal through a signal amplifier (MIDE QPA200).

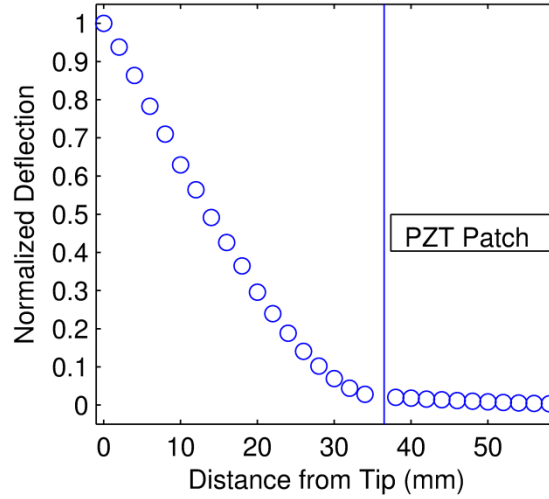


**Figure 5: Mode shape of the piezoelectric fan normalized by the maximum (tip) vibration amplitude**

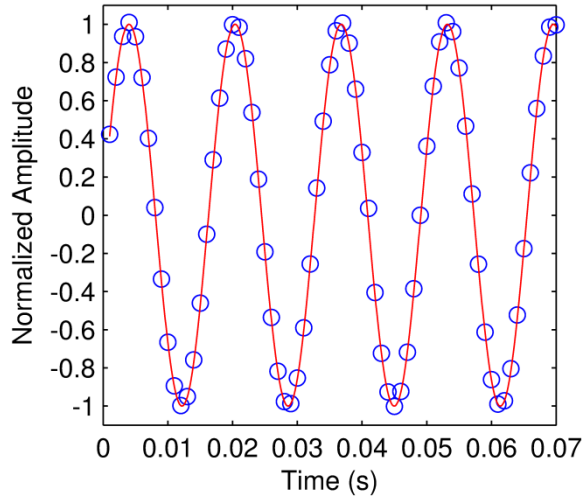


**Figure 6: Oscillatory motion of the piezoelectric fan tip as a function of time. The amplitude is normalized by the maximum (tip) vibration amplitude**

Close monitoring of the vibration response is required to maintain experiment validity and accuracy throughout testing. The precision error of the vibrometer is 0.03% of the full scale

and is positioned approximately 150 mm from the measurement surface. This distance is effectively the “optimal” spot for measurements.

For the flow field studies, a single vibration frequency ( $\omega$ ) and amplitude ( $A$ ) are analyzed. The piezofan is forced to oscillate at 62.5 Hz with a vibration amplitude of 2 to 4 mm in 0.5 mm increments. These are determined based on the desire to consider a range of Reynolds numbers which include those used in [52], and also extend beyond those values. The Reynolds number, as defined in Eq.(1), makes use of a velocity multiplied by a length scale normalized by the fluid viscosity ( $\nu$ ). The velocity is defined as the product of frequency and amplitude. This same displacement is used for the length scale such that the Reynolds Number ( $Re_A$ ) becomes:

$$Re_A = \frac{\omega A^2}{\nu} \quad (1)$$

For the particular fans used, the specified amplitudes yield Reynolds numbers of 105, 164, 236, 321 and 419 respectively (range considered in [52] is 43 to 146).

Care is taken to ensure that the laser displacement sensor recorded as close to the tip as possible. The mode shape of the piezofan is not perfectly linear; further, as the amplitude increases, the position of the fan tip is farther back in the  $x$ -direction at the point of maximum deflection (Illustrated in Figure 7). Therefore, the vibrometer was oriented just far enough back so that the full displacement amplitude was able to be captured.

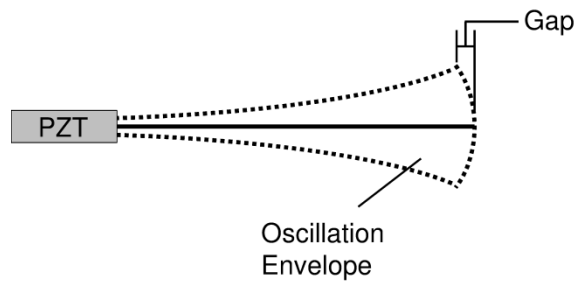


**Figure 7: Representation of the gap that occurs in this type of motion**

## 2.2 PARTICLE IMAGE VELOCIMETRY (PIV) SETUP

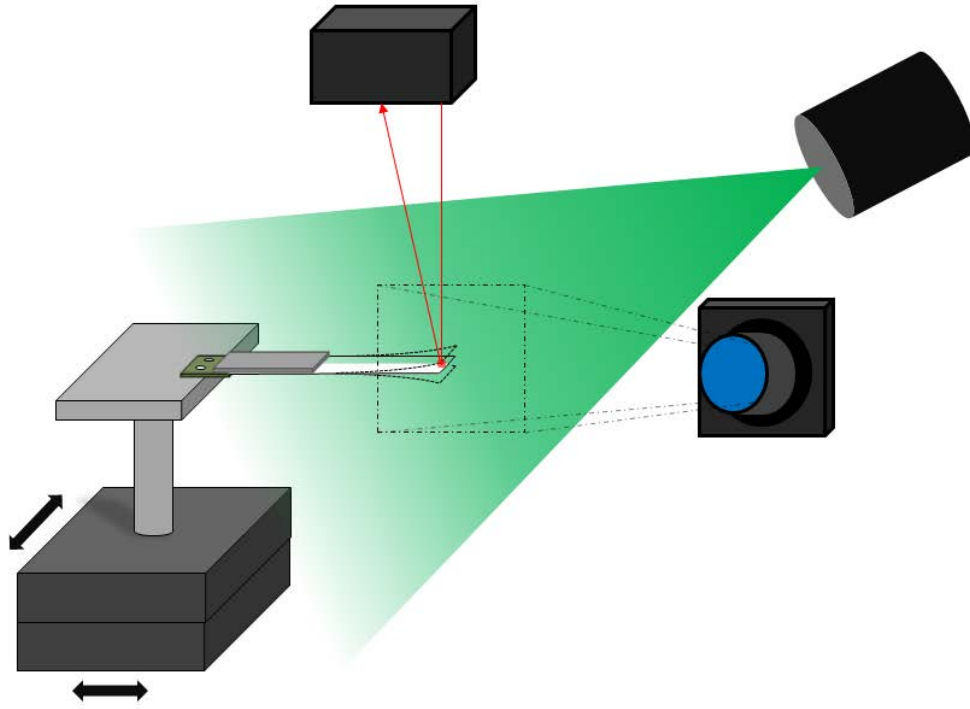


**Figure 8: Representation of the component orientation**

The flow field is captured using a Particle Image Velocimetry (PIV) system. This allows for unobtrusive and efficient analysis of an entire flow field all at once. A smoke pen is used to generate seeding particles within the enclosure, where they are allowed to diffuse and evenly distribute over a few minutes. The light sheet is generated by diverging the light from a 532 nm YAG laser (New Wave SoloIII-15Hz) into a sheet (see Figure 8). A camera (Powerview Plus 2MP), located outside the enclosure, captures the light that is reflected by the particles in two different orientations (see Figure 9). The camera timing is designed to capture two images in

quick succession (a time difference of 16  $\mu$ s) which is sent to an accompanying program (Insight3G) that completes a statistical analysis comparing the two images. The analysis was conducted with zero post collection error correction methods as the results only exhibited errors in the margins that were not included in the analysis. This analysis allows for the generation of velocity vectors over the entire field of view with a nominal uncertainty of 3.5%. Although the accuracy of the PIV analysis is very flow and setting dependent, this value is provided to give a general idea of the uncertainty that one could expect. All of the aforementioned components are controlled by a synchronizer (TSI 610034). The function generator, laser displacement, and piezo-amplifier signals are monitored via an oscilloscope (Tektronics DPO 3014).

The piezofan is mounted on a 90 mm tall post which is then mounted on a pair of linear stages that allow for adjustment in two axes ( $x$  and  $z$ ). The entire assembly is affixed to a laser table to reduce outside vibrations. A large enclosure, with dimensions of 305 mm x 610 mm x 406 mm, is placed over the entire system with the piezofan centered in the enclosure. The enclosure effectively isolates the system from ambient currents within the research space. This, along with the elevation from the post, allows for a sufficient distance of any large object from the fan so that boundary effects can be essentially ignored.

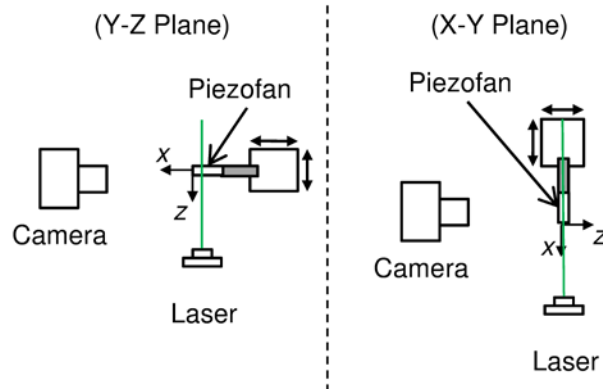


**Figure 9: Illustration of the two layouts used in capturing the flow field. The left illustration captures the y-z flow field and the right captures the x-y flow field**

The progression of the reporting of the results follows the progression of research and is indicative of how each discovery lead to the next stage of tests. Although much of the research was predetermined, there were findings that necessitated further investigation. The rough progression consists of the flow field analysis phase which includes both centerline (2-D flow) and multiple plane flow (3-D flow), thrust analysis and quantification of the effect of multiple operational factors, the effect of sidewalls on oscillation performance and thrust enhancement with sidewalls.

Due to the need of illuminating the domain with a laser sheet, the presence of the fan inevitably causes a shadow to be cast over a small area. This causes certain sections of the flow field to result in either zero or incorrect and inconsistent flow vectors. If not carefully dealt with, this can result in analysis that deviates from that which is physically realistic in other sections of the flow. Much effort is taken to limit the shadowing that occurs via careful orientation of the laser sheet. Thus, in both the  $x$ - $y$  and  $y$ - $z$  planes, the shadowing (seen in Figure 10) occupied a sufficiently minimal area in the inspection domain where the majority of flow was occurring.



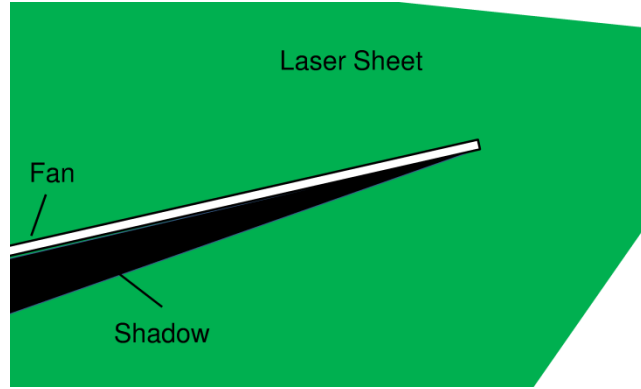


**Figure 10: Illustration of the shadowing effect of the laser sheet**

The seeding particles are introduced into the enclosure and allowed to spread for a period of a few minutes. The piezofan is then powered and the entire system is allowed to reach steady state (roughly 10 to 15 minutes). The PIV system is then initialized and flow field captures are taken at 15 degree phase increments from zero to 345 degrees. For each specific phase, a set of 50 image captures are taken in order to provide a statistical average of the flow field and mitigate inherent fluctuations that are present in unsteady flows. The PIV system available does not include time-resolved capabilities and therefore cannot provide data acquisition speeds sufficiently high enough to analyze data for a single vibration cycle.

A flow field analysis is performed for a series of  $x$ - $y$  and  $y$ - $z$  planes. For the  $x$ - $y$  planes, the flow data is taken for  $z = 0$  to 6 mm in 1 mm increments. Note that  $z = 0$  represents the centerline location along the length of the fan. For the  $y$ - $z$  plane, data is acquired from  $x = -8$  mm to 2 mm in 2 mm increments. Note that  $x = 0$  represents the tip of the fan blade. From the flow field data, the  $x$ ,  $y$ , and  $z$  velocities ( $U_x$ ,  $U_y$ , and  $U_z$  respectively) can be analyzed. The vorticity is determined by using the “curl” function of Matlab. This function uses the “gradient” function to determine the velocity differences. The gradient uses a central differencing numerical scheme in the central portion of the matrix and either a forward or reverse scheme around the edges as

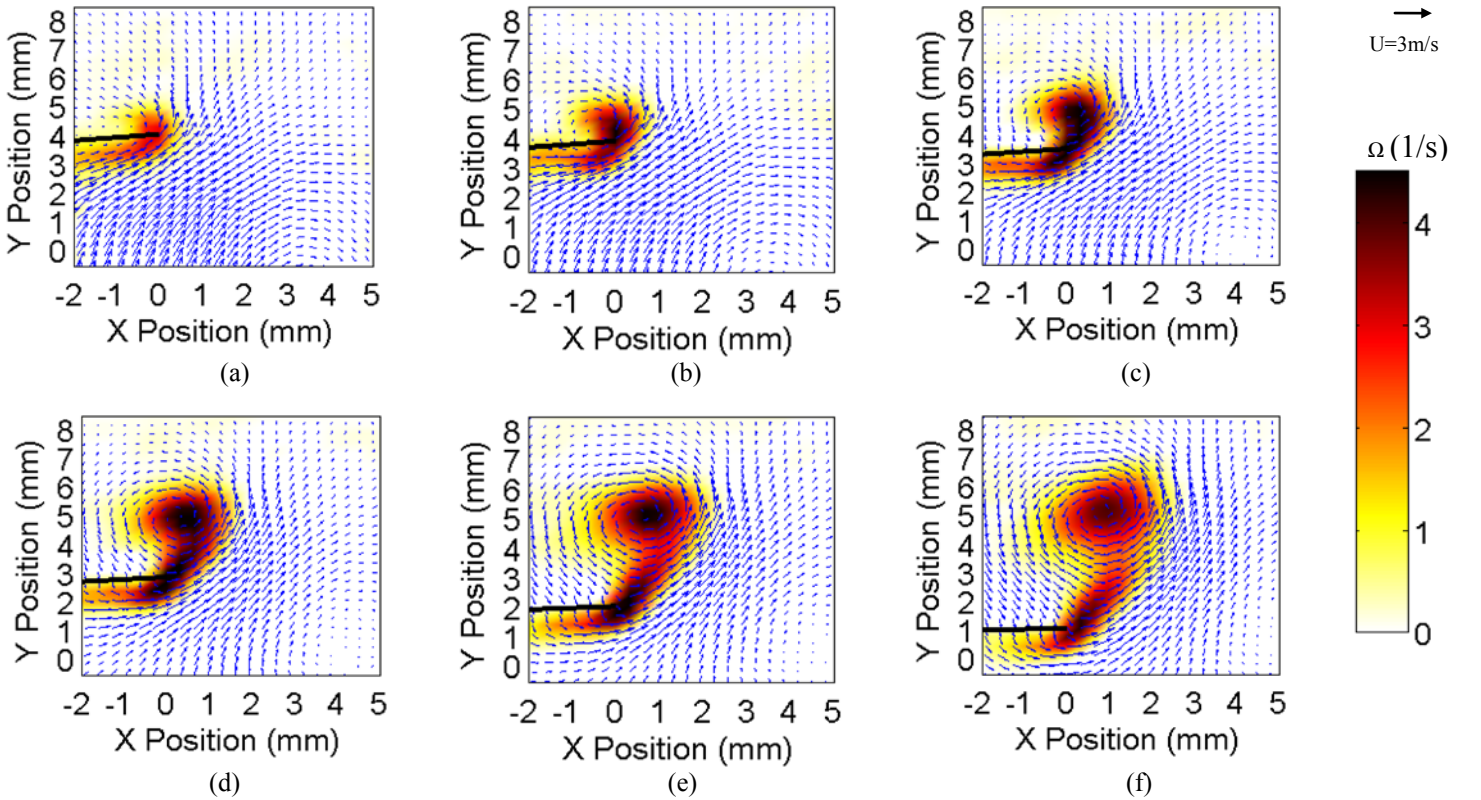
appropriate. This data and its subsequent analysis sets the ground work for further tests to optimize the  $x$ -directional flow, and therefore thrust, by using sidewalls that bound the flow in targeted locations while not limiting flow regions just outside the fan. In a more broad sense, this flow field analysis allows for a better understanding of the nature of the flow generated by an oscillating cantilever and how to utilize it to its fullest potential.

### **2.3 CENTERLINE X-Y PLANE ANALYSIS**

Vortex formation is a well known byproduct when dealing with flow past a sharp edge (as is the case with a vibrating cantilever beam). This process is important to understand for a number of reasons. For example, vortex formation and control plays a primary role in biological propulsion [6, 20], the movement of the vortex can give an indication of bulk fluid motion, and vorticity also plays a role in lift. In the case of propulsion, knowing (and possibly controlling) the vortex location and trajectory will potentially allow for the recapturing of some of that lost energy.

A vortex is formed each half cycle of oscillation from the sharp edge of the fan tip. This process is perhaps most easily observed near the fan tip, and at the  $z = 0$  plane, defined as the centerline of the fan blade. The data fields shown in Figure 11 demonstrate the downward stroke of the fan from a phase angle of 90 to 165 degrees in 15 degree increments. It can be seen that even though the fan itself has no velocity at a phase of 90 degrees, the upward flow generated by the fan in the first quarter of the cycle is already starting to generate a counter clockwise (CCW) vortex. With detachment being defined as the point where the vortex is no longer being driven by the fan blade (i.e. the point of maximum vorticity in the cycle), it can be observed that

detachment appears to occur approximately between a phase angle of 135 and 150 degrees. After detachment, as expected, the vortex travels away from the fan and begins to increase in size and lose its energy. A clockwise (CW) vortex is generated in the negative  $y$  region and is 180 degrees out of phase with the CCW vortex. The continual shedding of this vortex pair constitute what is known as the reverse Karman vortex street, and is also seen in the wake region of fish and other marine animals whose propulsion is gained through oscillations [6, 66, 67]. For the additional amplitudes considered, the behavior is qualitatively similar. In other words, although the strength of the vortex is amplitude dependent, the formation and shedding process is consistent for all experiments.



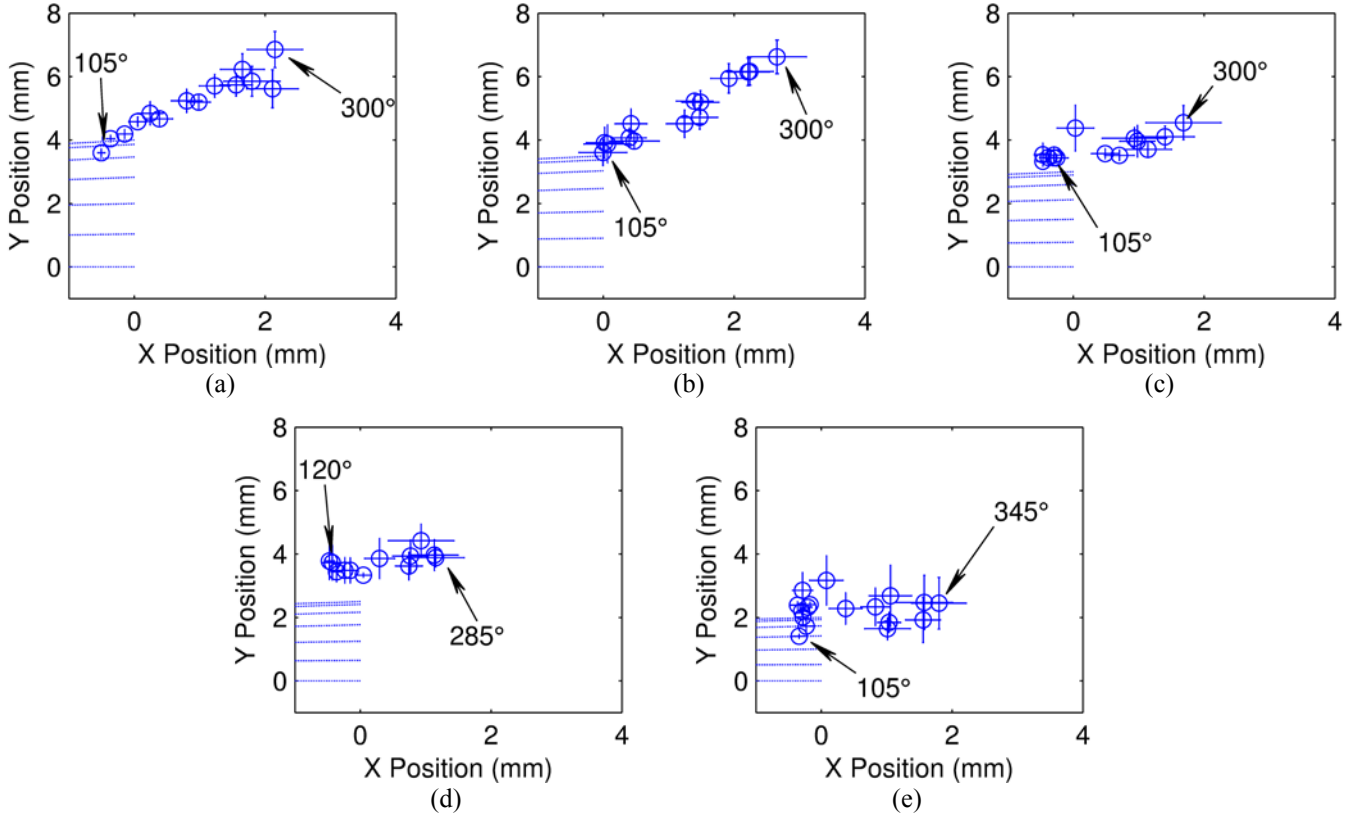
**Figure 11: Two-dimensional flow field and full-field vorticity for  $A = 4$  mm and phase equal to (a)  $90^\circ$ , (b)  $105^\circ$ , (c)  $120^\circ$ , (d)  $135^\circ$ , (e)  $150^\circ$ , and (f)  $165^\circ$ .**

Table 1 displays the average angle of travel and average translational velocity of the vortex. The reference axis is positive counter-clockwise with zero degrees being parallel to the fan blade. From 3.5 mm to 2 mm, as the amplitude decreases, the angle of the vortex travel decreases. Both the 4 mm and 3.5 mm case have roughly the same angle of travel. Translational velocity of the vortex (shown in the third column) also falls with decreasing amplitude. This can be mainly attributed to a decrease in tip velocity. It is interesting to note that for the data in Table 1, the maximum fan tip speed ( $\omega A$ ) for all amplitudes is 3 to 4 times larger than the translational velocity of the vortex.

**Table 1: The translational velocity and direction of the vortex path.**

<b>Amplitude</b>	<b>Angle (Degrees)</b>	<b>Translational Velocity (mm/s)</b>	<b>Fan Tip Speed (mm/s)</b>
4.0 mm	44.2	474	1571
3.5 mm	45.9	390	1374
3.0 mm	19.5	266	1178
2.5 mm	12.0	250	982
2.0 mm	0.4	202	785

Figure 12 shows an interesting trend in how the vortex travels as amplitude changes. The 8 mm case (Figure 12(a)) has a very well defined vortex path which increases in uncertainty as the distance from the fan tip grows. By contrast, the 3 mm case (Figure 12(c)), reveals a large grouping of points near the fan tip with the remainder of the points showing a path with a definite trend, although the uncertainty has increased. This same behavior is most easily seen in the 2 mm case (Figure 12(e)).



**Figure 12: Vortex paths for  $A =$  (a) 4 mm, (b) 3.5 mm, (c) 3 mm, (d) 2.5 mm and (e) 2 mm. The vortex is tracked over the phase range displayed on each graph. The error bars are based on the statistical averages of experiments repeated 50 times.**

The strength of the vortex for each amplitude from a 90 degree phase angle to 345 degrees can be seen in Figure 13. Despite a change in vibration amplitude, the peak vorticity occurs at roughly the same phase. This would indicate that the vorticity peak is dominantly

dependent upon where the fan is in its oscillation cycle and that the effect of amplitude is negligible.

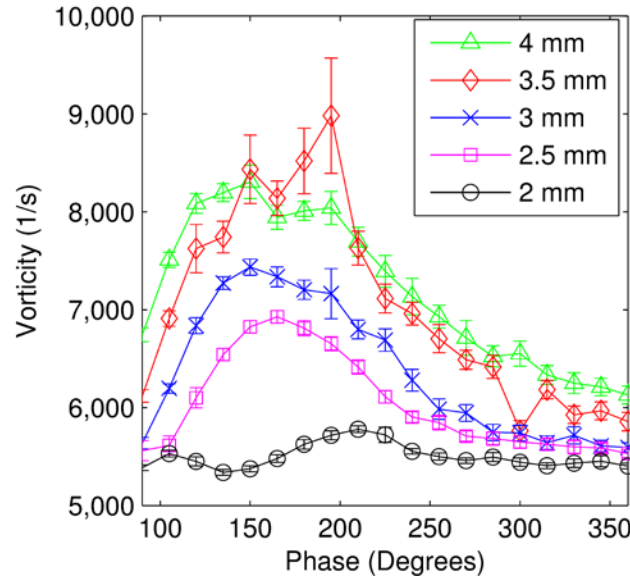


**Figure 13: Maximum vorticity for each amplitude with respect to phase angle of the fan.**

In observing Figure 13, it can be seen that the maximum vorticity decreases with amplitude. This is a logical conclusion, in that a higher tip velocity would create a faster spinning vortex. It should be noted that the 3.5 mm case does not necessarily follow this argument, yielding a vorticity peak that is higher than the 4 mm case. It is also possible that the 3.5 mm case has a high degree of instability such that the results from different vibration cycles are not as repeatable. Comparing the magnitude of the error bars in Figure 13 suggests that even after removing statistical outliers, the 3.5 mm case has the largest amount of uncertainty.

Also worth noting in Figure 13 is that all the vortices dissipate at roughly the same rate. This outcome is logical in that when the vortex detaches from the fan tip it is only subjected to the surrounding air at some constant viscosity which then provides the dissipation. This is more easily seen if the vorticity curves from Figure 13 are normalized by their respective maximum

values as shown in Figure 14. The behavior of each amplitude is shown to collapse into a single curve, suggesting a correlation could be developed to predict the growth and decay of a vortex shed by an oscillating piezoelectric fan. Only the 2 mm case (not shown in Figure 14) does not follow this trend. This will likely be understood better as the full three-dimensional flow field is understood in greater detail.

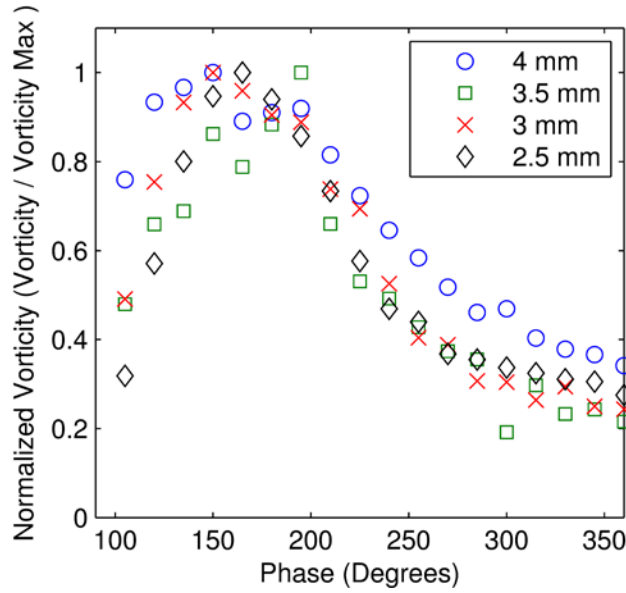


**Figure 14: Vorticity plots of  $A = 4$  mm, 3.5 mm, 3 mm and 2.5 mm. Normalized by each corresponding maximum vorticity.**

The maximum local velocities ( $x$  and  $y$  components) experienced during a vibration cycle can be seen in Table 2 for all amplitudes considered. For all five amplitudes,  $U_x$  is the dominant velocity. This is most evident for the three smallest amplitudes where the maximum velocity only has an  $x$  component. For the 4 mm and 3.5 mm cases,  $U_x$  is still dominant, but  $U_y$  can no longer be neglected when determining the overall maximum velocity ( $U$ ).

Cycle-averaged flow fields can also provide significant insight into the key flow features. These are shown in Figure 15 for each of the five vibration amplitudes considered for this centerline data ( $z = 0$ ). The velocity near the fan tip is predominantly in the  $x$ -direction for the lower amplitudes (Figure 15 (c)-(e)), while for the higher amplitudes (Figure 15 (a) and (b)), the flow in this same region (near the fan tip) is in a more upwardly direction indicating possibly some sort of behavior change based on amplitude. This is the same observation made in regard to the instantaneous flow field data presented in Table 2. In other words, a distinct shift in dominant flow direction is apparent when comparing the results from the 3 mm case (Figure 15(c)) and 3.5 mm case (Figure 15(b)). The lower amplitudes seem to exhibit more of a jet-like appearance, similar to what was observed in Kim et al. [52] for the cycle-average flow. Therefore, transitions in Figure 15 suggest one might be encountering a departure in the flow behavior from small amplitude restrictions. It can also be seen in Figure 15 (a) and (b) that the jet-like flow may be slightly asymmetric. It is not conclusively known what the cause is, however a paper by Ellenrieder and Pothos [68] may shed some light on a potential reason. They found that asymmetries in the flow are observed at a Strouhal number that is above 0.434. Although there is no free stream velocity in the current experiments, it is conceivable that the operation of the oscillating cantilever operates above an effective Strouhal number of 0.434. Since many of the intended applications (e.g., heat transfer or propulsion) will benefit from larger vibration amplitudes, we now take the large case ( $A = 4$  mm) from this centerline data and explore the flow fields over a range of analysis planes both in the  $x$ -direction ( $y$ - $z$  planes) and in the  $z$ -direction ( $x$ - $y$  planes).



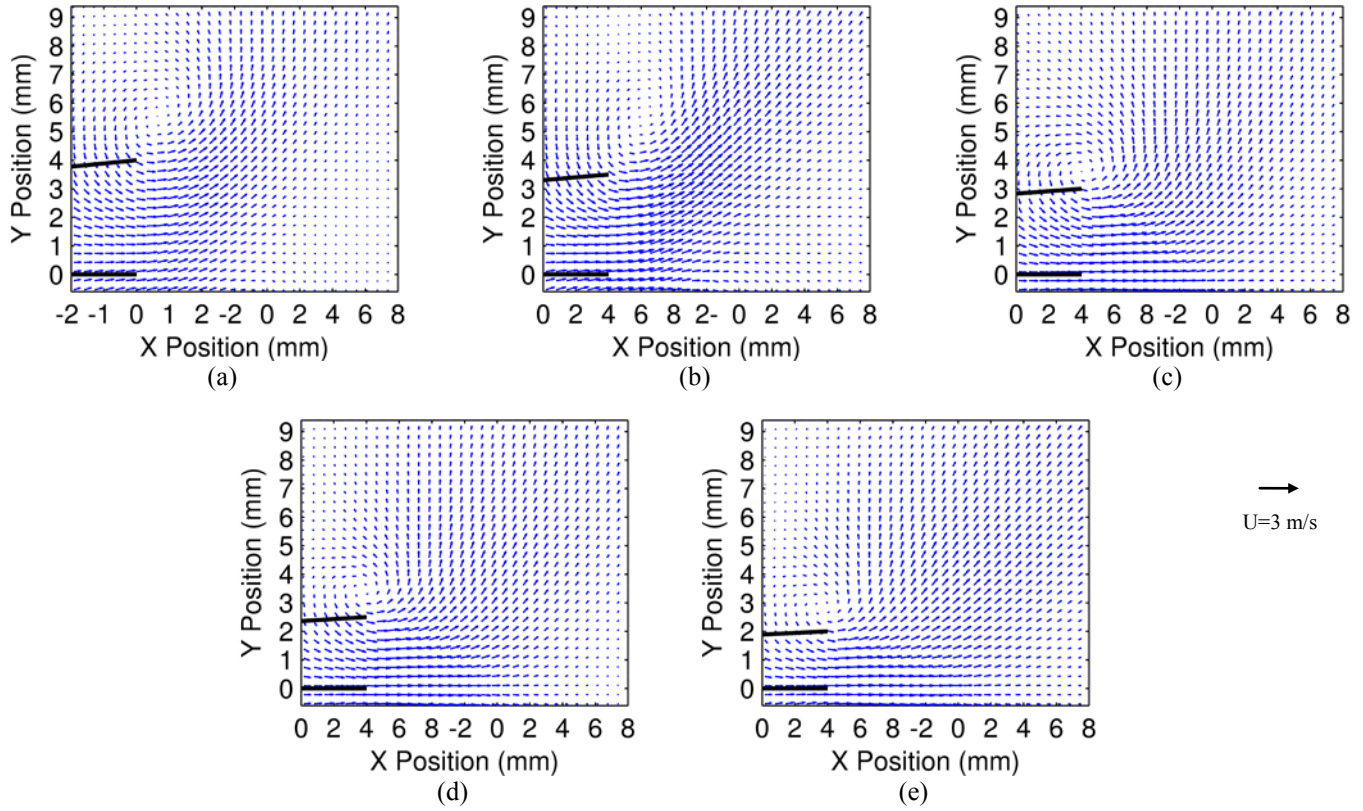


**Figure 15: Cycle averaged flow fields determined from 1250 captures over one full period for  $A =$  (a) 4 mm, (b) 3.5 mm, (c) 3 mm, (d) 2.5 mm and (e) 2 mm.**

Although the amplitude changes, we can see in Table 2 that the maximum flow velocities are relatively unchanged other than those between the 3.5 mm and 3 mm case. Also, maximum overall flow is less for the higher amplitude cases, which is counter intuitive given the fact that at higher amplitudes one would expect larger tip speeds. However, due to the fact that the piezoelectric fan used in the current study has a length greater than its width and the fact that no sidewalls are present; this behavior is attributed to the inability to capture flow velocities in the  $z$ -direction in the current setup.

**Table 2: Maximum  $x, y$  and overall velocity in the flow field for each amplitude.**

	<b>4.0 mm</b>	<b>3.5 mm</b>	<b>3.0 mm</b>	<b>2.5 mm</b>	<b>2.0 mm</b>
<b>Max <math>U_x</math> (mm/s)</b>	943	930	1096	1124	1028
<b>Max <math>U_y</math> (mm/s)</b>	697	646	657	601	520
<b>Max <math>U</math> (mm/s)</b>	975	947	1096	1124	1028

As was found in [52], a vortex source can be observed from the cycle-averaged flow fields in Figure 15. The position of this vortex remains relatively unchanged, regardless of the amplitude considered. The location is, in general, just above the fan at its maximum displacement. The distance between the fan and this vortex core is slightly larger for the 3.5 mm and 4 mm cases (Figure 15 (a) and (b), respectively). Larger amplitudes and additional frequencies should be tested in order to better characterize the location of this vortex in the cycle-averaged flow fields.

## **2.4 OFF CENTERLINE MULTIPLE PLANE ANALYSIS**

Once the 2-dimensional flow field from an oscillating cantilever is understood, it follows that an investigation into where this assumption begins to break down and become more 3-dimensional in nature. This is of particular importance for a cantilever with an aspect ratio ( $L_b/D$ ) that is on an order of magnitude of one. The flow field data from averaging over all 24 phase angles represents the cycle-averaged flows. Of primary importance is the  $x$ -directional flow velocity ( $U_x$ ) whose cycle-averaged flow fields are shown in Figure 16 for  $z = 1$  mm to 6 mm. Near the center of the fan (Figure 16(a)), a region of significant  $U_x$  is seen just beyond the fan tip. This behavior is also observed for  $z = 2$  mm (Figure 16(b)) and  $z = 3$  mm (Figure 16(c)). These findings are consistent with Kim et al. [52] who experimentally investigated two-dimensional

flows, as well as work presented in the previous subsection. The instantaneous flow fields in these studies reveal two counter rotating vortices shed from the sharp edge (fan tip) during each vibration cycle. The combined effect of the vortices in a cycle-averaged flow field is similar to a jet issuing forth into a quiescent medium. Also worth noting in Figure 16(a) – (c) is the presence of a negative  $U_x$  region of flow near the upper corner of the oscillation envelope (i.e., when the fan is at its maximum amplitude). This is attributed to the vortex that is shed during the downward stroke, and acts to pull air into the oscillation envelope from the region above the maximum fan displacement.

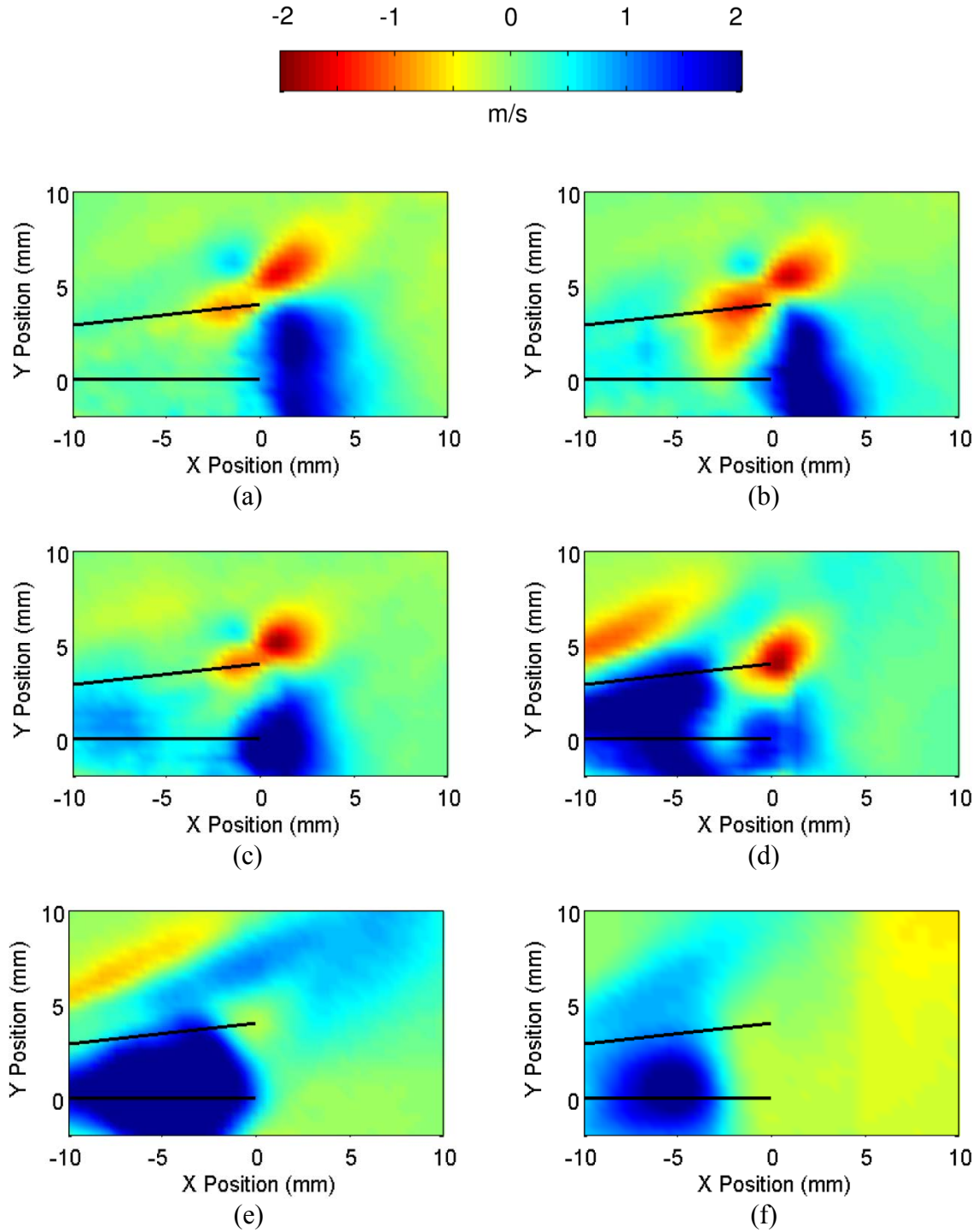


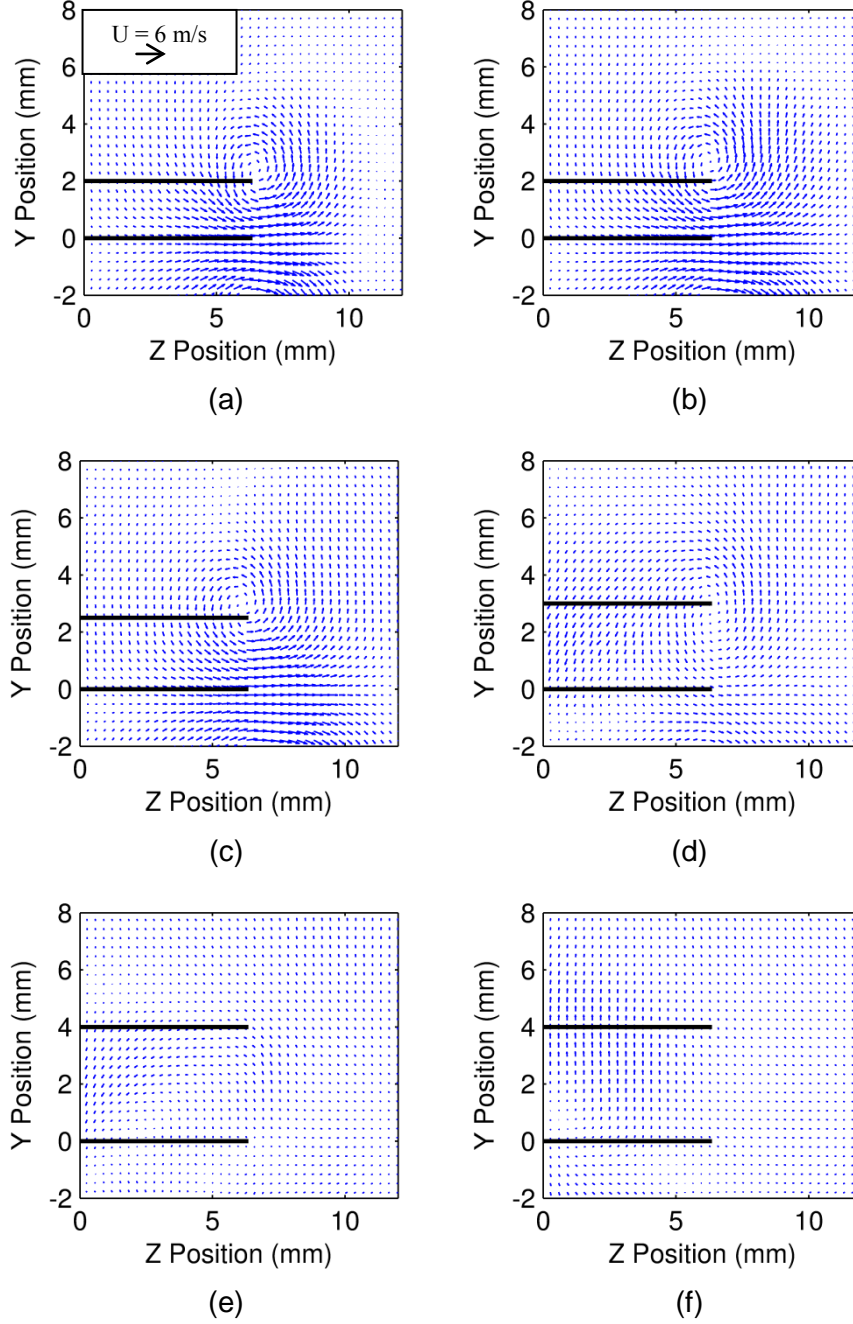
**Figure 16: Cycle-averaged  $U_x$  along the  $z$ -axis in the  $x$ - $y$  plane for different  $z$  values: (a) 1 mm, (b) 2 mm, (c) 3 mm, (d) 4 mm, (e) 5 mm and (f) 6 mm. The solid dark lines represent the fan at phase angles of 0 (non-displaced position) and 90 degrees (maximum displacement).**

For a highly three-dimensional flow such as the one in this work, it is expected that the two-dimensional behavior will begin to transition at some distance from the lengthwise axis of the fan ( $z = 0$ ). The current data suggests that this occurs at  $z = 4$  mm (Figure 16(d)), or approximately 63% of the distance from the center to the edge of the fan (fan half-width), evident from the fact that the concentrated region of high  $U_x$  is no longer present just beyond the fan tip. This is the plane where the three-dimensionality of the flow begins to be felt and the two-dimensional predictive tools no longer apply. It is expected that the  $z$ -location of this plane will ultimately depend on fan geometry (e.g., fan with small width should provide very little  $x$ -momentum) as well as oscillation frequency and amplitude, but it is interesting to note that for the current experimental conditions ( $A = 4$  mm and  $D/2 = 6.35$  mm), the location of this plane is the same as the vibration amplitude ( $A$  and the location where transition occurs are both 4 mm). Data from the same fan vibrating at different amplitudes would provide insight into whether this dependence is maintained.

As the data extraction plane continues to shift from  $z = 4$  mm to 6 mm (Figure 16(d) through (f)) there exists a significant  $U_x$  within the oscillation envelope of the fan. This is not present for small values of  $z$  (near the center of the fan) and suggests that in addition to pulling air from locations above and below the envelope of oscillation, flow is also supplied from off-center upstream locations.

The fact that vortices are generated from flow over sharp edges can be seen in the  $y$ - $z$  plane as well. This is evident from the cycle-averaged flow fields shown in Figure 17 for  $x = -8$  mm to  $+2$  mm. For sufficiently far upstream locations ( $x = -8$  to  $-4$  mm as shown in Figure 17(a)-(c)), the vortex fully forms by the time a half cycle is completed. This, when observed as cycle-averaged data, exhibits similarities to the flow fields seen in the  $x$ - $y$  plane near the fan tip (i.e.,

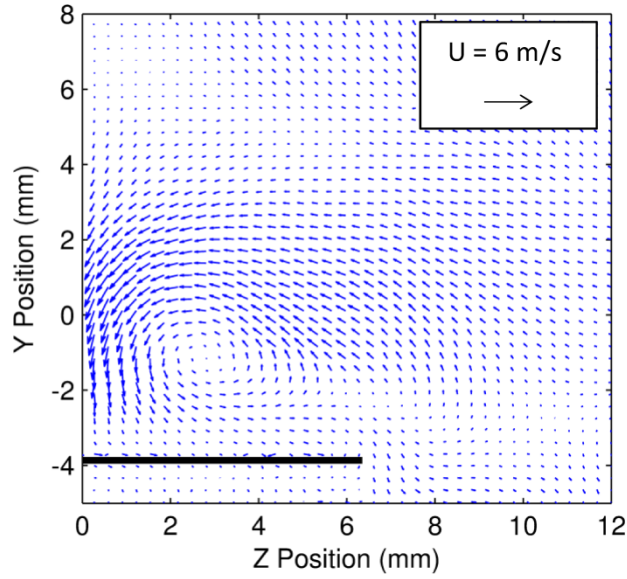
similar to jet issuing forth into quiescent medium). For locations further upstream ( $x < -8$  mm), the vortex size and velocity magnitudes decrease as the analysis plane moves further upstream due to the decrease in the *local* vibration amplitude at a particular cross-section. However, behavior of the flow field in the  $y$ - $z$  plane becomes notably different near the fan tip and is no longer two-dimensional. Near the tip of the fan ( $x = -2$  mm to 2 mm as shown in Figure 17(d)-(f)), there is no noticeable vortex in the cycle-averaged flow.



**Figure 17: Cycle-averaged velocity vectors in the y-z plane at different x positions.(a)-8 mm, (b)-6 mm, (c) -4 mm, (d) -2 mm, (e) 0 mm and (f) 2 mm. The solid dark lines represent the fan at phase angles of 0 (non-displaced position) and 90 degrees (maximum *local* displacement). The velocity magnitude indicator is uniform for (a) through (f) and shown in (a).**

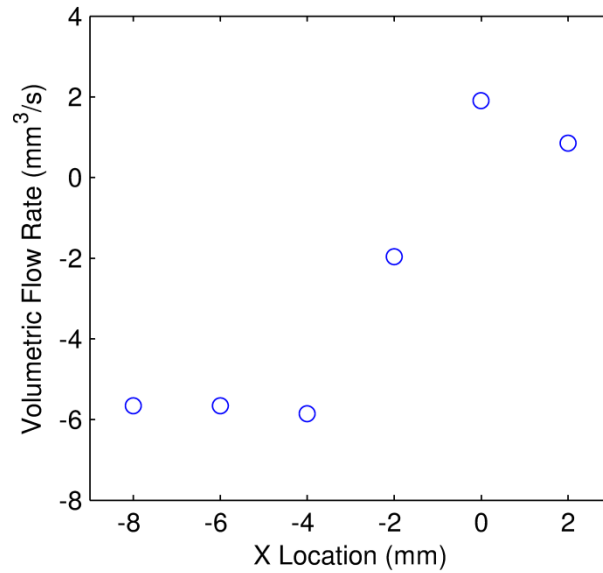
In previous two-dimensional computational [56] and experimental studies [53, 69], the vortex formation and detachment processes both occur during the first half of the vibration cycle (before a phase angle of 180 degrees). Vortex detachment was deemed to have occurred when the vortex is no longer visibly affected (when observing a plot of vorticity) and is no longer being contributed to by the sharp edge of the beam. By contrast, the experimental results at the fan tip ( $x = 0$ ) suggest a significant delay in this vortex formation process. The velocity vectors for a phase angle of 225 are shown in Figure 18, and reveal that a vortex is indeed present, but because of the delay in forming is unable to detach and is swallowed up during the return cycle. The vortex also resides near the ( $y = 0$ ) centerline of the oscillation envelope, which indicates that a counter rotating vortex would reside at relatively the same position. The result is the absence of a visible signature of the vortex in the cycle-averaged data (Figure 17 (d)-(f)). This delayed vortex formation and movement is atypical and not seen anywhere else in either the  $x$ - $y$  and  $y$ - $z$  flow planes. It is possible that the effect is caused by the highly three dimensional nature of the flow field near the fan tip. More specifically, as seen in Figure 16,  $U_x$  at the fan tip is concentrated near the centerline ( $z = 0$ ). It would be reasonable to assume that the concentrated  $U_x$  pulls the vortex towards the centerline of the fan. This results in  $U_z$  towards the fan rather than away, which is contrary to what is expected. This may also be the reason for a delayed vortex formation.





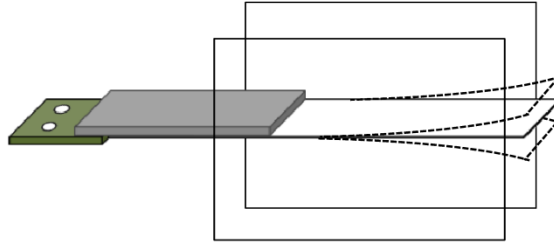
**Figure 18: Instantaneous velocity vectors in the  $y$ - $z$  plane at  $x = 0$  mm and a phase of 255 degrees.**

Figure 17 is analyzed further by computing the flow rate for each set of data from  $y = -A_{local}$  to  $+A_{local}$  along the line  $z = D/2$ . The result is shown in Figure 19 and reveals the magnitude of the flow in and out of the vibration envelope along the length of the fan. The flow rate is positive (toward the fan) for  $x > \sim -1$  mm and negative (away from the fan) otherwise. The peak flow rate in the  $z$ -direction is observed at or around  $x = 0$  mm (the fan tip). These results provide a simple basis for optimizing  $x$ -directional thrust. In particular, sidewalls could prove very effective in the event that they could be tailored to prevent flow from escaping the oscillation envelope for  $x < \sim -1$  mm, but still promote outside flow entering the envelope in the  $x > \sim -1$  mm region.



**Figure 19: Volumetric flow rate along a half cycle of the oscillation amplitude with respect to the  $x$  location of the  $y$ - $z$  plane. Positive indicates flow toward the centerline of the piezofan.**

Figure 20 illustrates a simple conceptual design that would potentially accomplish these goals. The sidewalls would terminate near the demarcation line between positive and negative flow rate in the  $z$ -direction. Based on the cycle-averaged results from Figure 17, the flow field remains relatively unaffected a distance of 1 cm away from the fan. Therefore the gap between the fan edge and the sidewall can be tested from very small values up to 1-2 cm away to determine optimal spacing. For example, a very small gap may better prevent unwanted flows in the  $z$ -direction, but would also cause greater viscous drag (see Kimber et al. [45]). Therefore careful and systematic studies should be conducted to investigate the effect of this gap on performance. This proposed sidewall design has the benefit of being very simple and provides a basis from which thrust optimization studies can then be made.



**Figure 20: General representation of a potential sidewall geometry based on the analyzed data. The dashed lines represent the approximate operational area of the piezofan.**

## **2.5 STREAMLINES AND VORTEX PROPAGATION**

Also of importance in analyzing this data is to quantify the effective inlet region of the fan. In other words, determine from which upstream locations the flow is originating. In previous research by Kimber et al. [42], it was postulated that the effective inlet for a piezofan is directly above and below the face of the vibrating cantilever. In order to gauge the adequacy of this claim and to better quantify the effective inlet, the multi-plane cycle-average flow field is analyzed in terms of the streamlines. These can be initiated at any point in the flow field and are generated in Matlab using the raw velocity data. In Figure 21, streamlines are initiated at  $\langle -5, 8, 3 \rangle$  (*blue*),  $\langle -4, 8, 3 \rangle$  (*red*),  $\langle -6, 8, 2 \rangle$  (*green*), and  $\langle -5, 8, 2 \rangle$  (*brown*) and are seen to travel toward the face of the fan and then toward the fan tip, thereby supporting the claims previously mentioned. Note that the two streamlines entering at  $z = 3$  mm (blue and red curves) travel toward the face of the fan

and then continue in the  $x$ -direction. The other two streamlines (green and brown curves) enter at  $z = 2$  mm and also travel toward the face of the fan, but then cross toward the center of the fan. Once they approach the center of the fan, they finally begin moving in the  $x$ -direction again. This indicates that there is a flow inlet region above the face of the cantilever. Note that, although the streamlines may appear to stagnate at the centerline this is not the case. The algorithm that determines the streamlines is only looking at half of the flow on the fan and therefore there is no flow pushing in the opposite direction on the other side of the centerline. If this were the case, one could naturally assume that the flow would change very slightly in that respect. Thus, these streamlines should be assumed as more of a guide or indicator of how the flow behaves on a cycle-average basis.

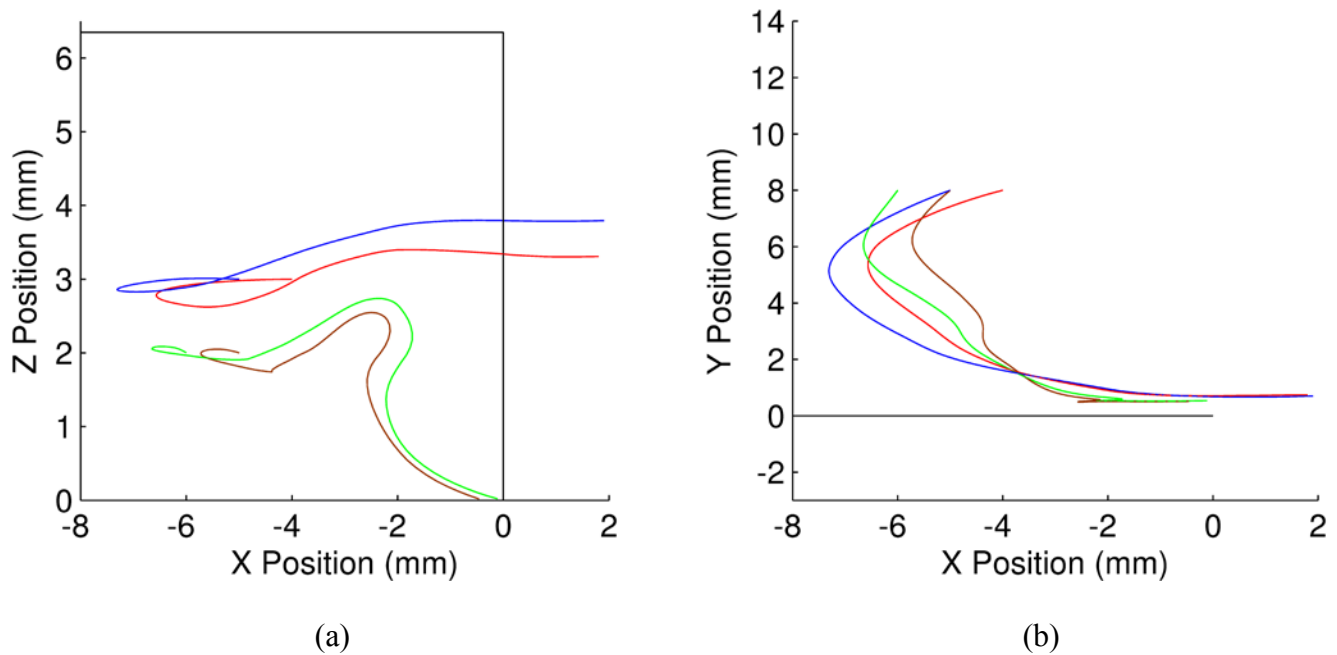


**Figure 21: Streamlines over the piezofan with origins 8 mm above the face of the fan. (a) is above the face of the fan looking down and (b) is beside the fan looking across the face.**

Additional streamlines are analyzed for  $\langle -8, 2, 4 \rangle$  (*blue*),  $\langle -8, 2, 3 \rangle$  (*red*),  $\langle -8, 2, 2 \rangle$  (*green*), and  $\langle -8, 2, 1 \rangle$  (*brown*). These results are shown in Figure 22, and indicate that there is also some flow entering from upstream of the main inspection area. The flow that enters from upstream, instead of traveling straight in the  $x$ -direction, is pulled toward the edge of the fan as it travels further downstream. This indicates that it is being influenced by the  $U_z$  flow being lost over the edge of the fan. The streamlines also indicate that all of this flow, even that which originates near the center of the fan, travels primarily in the  $x$ -direction. The streamlines also remain fairly close to the neutral position of the fan blade ( $y = 0$ ) effectively never traveling outside of the fan oscillation envelope. Interestingly, although the flow seems to follow the same general path, the furthest streamline from the center (*blue*) makes a wider arc towards the fan tip than the others. This would indicate that, as one would expect, the influence of the edge effects are stronger with decreased proximity to the edge. This may also explain, for that particular streamline, why it travels in the positive  $y$ -direction as well.

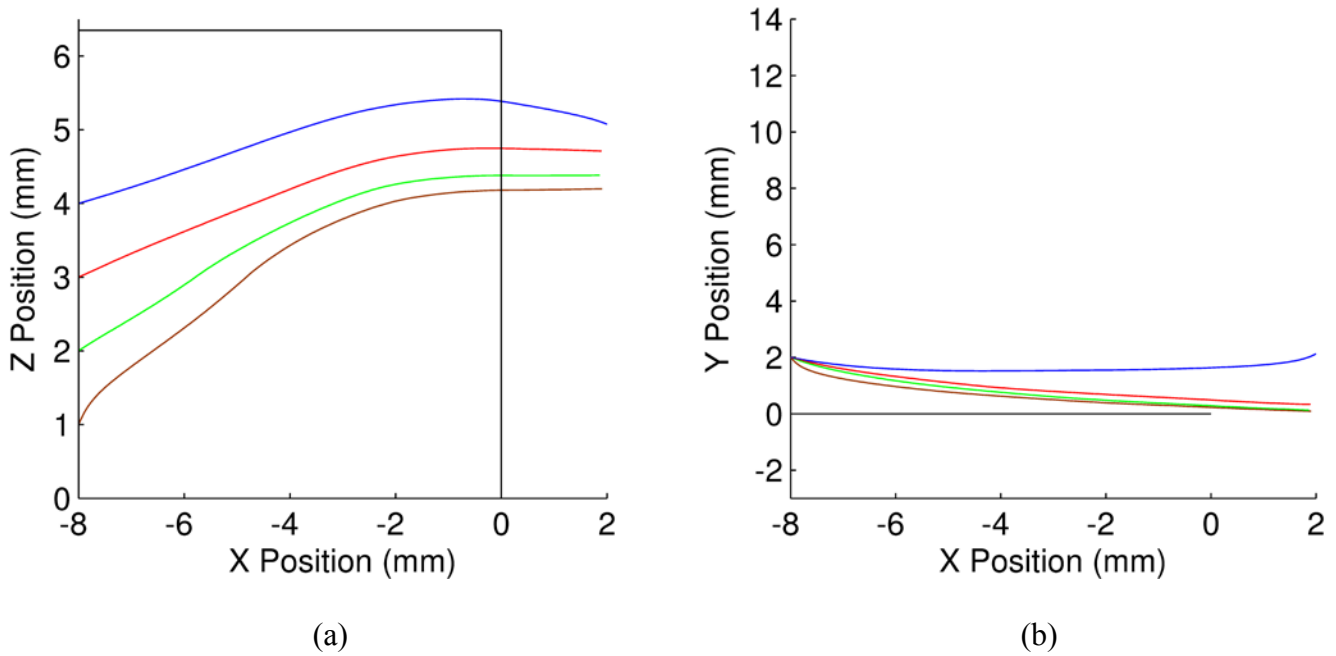


**Figure 22: Streamlines over the piezofan with origins upstream of the flow. (a) is above the face of the fan looking down and (b) is beside the fan looking across the face.**

At the side edge of the fan, the flow effectively exits off of the edge and travels away from the fan; however, at locations just inside this edge, the streamlines exhibit a very different behavior as shown in Figure 23 for  $\langle -8, 2, 5 \rangle$  (blue),  $\langle -7, 2, 5 \rangle$  (red),  $\langle -6, 2, 5 \rangle$  (green), and  $\langle -5, 2, 5 \rangle$  (brown) (approx. 1.35 mm from the edge for all four points). These streamlines initially travel in the  $x$ -direction (downstream), but are pulled toward the origin  $\langle 0, 0, 0 \rangle$  as early as at  $x = -2$  mm where they then travel with a positive  $U_x$  along the centerline. It is possible that this is a product of flow at the side of the fan near the tip being drawn in rather than away from the fan. This would also explain where the flow at the center of the fan originates since many of the previously mentioned upstream streamlines effectively move away from the center of the fan. Also worth noting is the fact that the upstream flow (Figure 22) remains primarily below  $y = 2$

mm while the edge located streamlines (Figure 23) reside above  $y = 2$  mm until they complete their crossover to the center of the fan. Again, similar to the streamlines originating above the fan, the flow turns toward the fan tip once it nears the centerline. This would indicate that there is some amount of non-uniformity in the flow above the face of the fan blade.

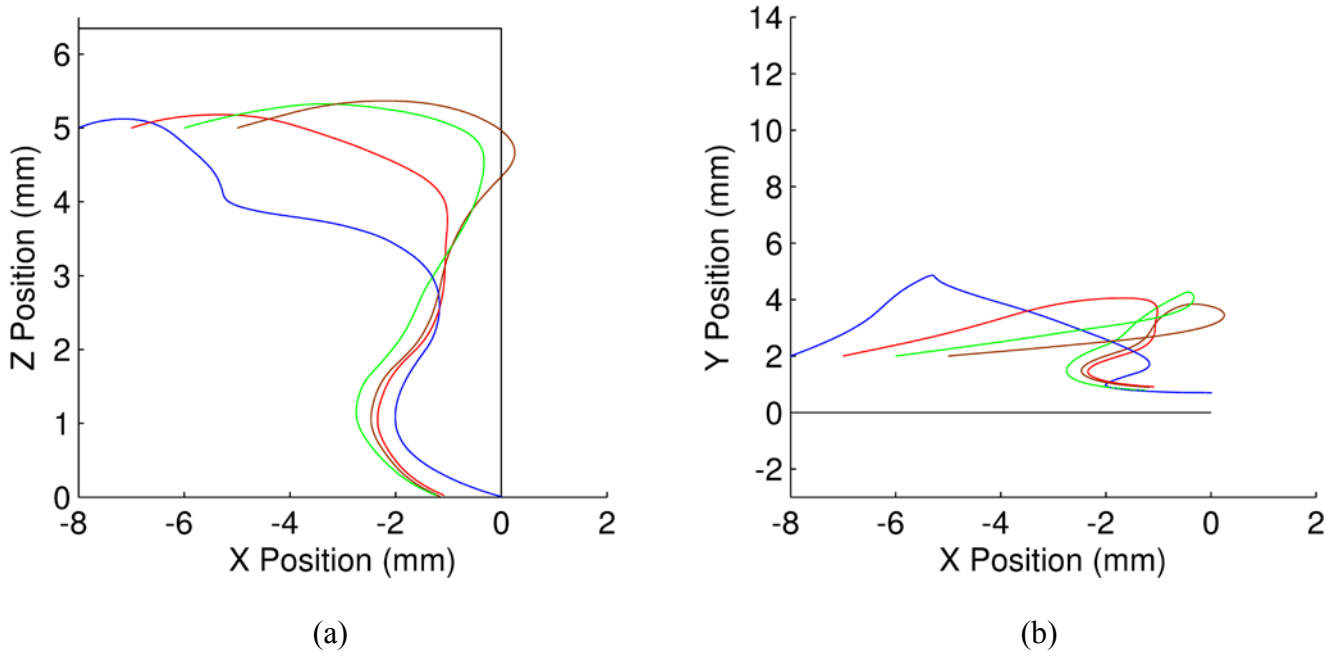


**Figure 23: Streamlines over the piezofan with origins at 5 mm from the center of the fan. (a) is above the face of the fan looking down and (b) is beside the fan looking across the face.**

Flow fields at instantaneous phase points in time can be found in Figure 24 for  $x = -8$  mm. This is far enough upstream that it compares quite well to that found in previous two-dimensional numerical simulations [56] focused on vortex shedding from the side edge and experimental observations from Kim et al [52] as well as those previously described from the current set of data. The vortex formation process begins on the downswing of the fan with detachment occurring at roughly 180 degrees. At that point, the magnitude of the vortex is at its

peak and slowly diminishes further into the oscillation cycle. Although similar two-dimensional expectations were realized for the  $x$ - $y$  plane (see Figure 11) in terms of vortex formation and shedding, the vortex signature in this set of results includes two distinct tails for the later oscillation phases shown (Figure 24(e) and (f)). The vortex is initially very circular in shape and begins to be stretched along one of its axes around a phase of  $240^\circ$ . The two tails of the vortex are linked to the major axis of the vortex core and rotate as the ellipse rotates. The clockwise rotating vortex that was formed during the previous half of the oscillation cycle is still present and visible for a phase up to  $180^\circ$  (Figure 24(a) through (c)), although diminished in magnitude. The counter-clockwise vortex then pulls the clockwise vortex to the opposite side of the fan blade before it disperses. This effectively occurs during the entire generation and detachment phase of the vortex that supersedes the previous vortex. Results very similar to these are observed for data capture at  $x = -6$  mm and are not included here.



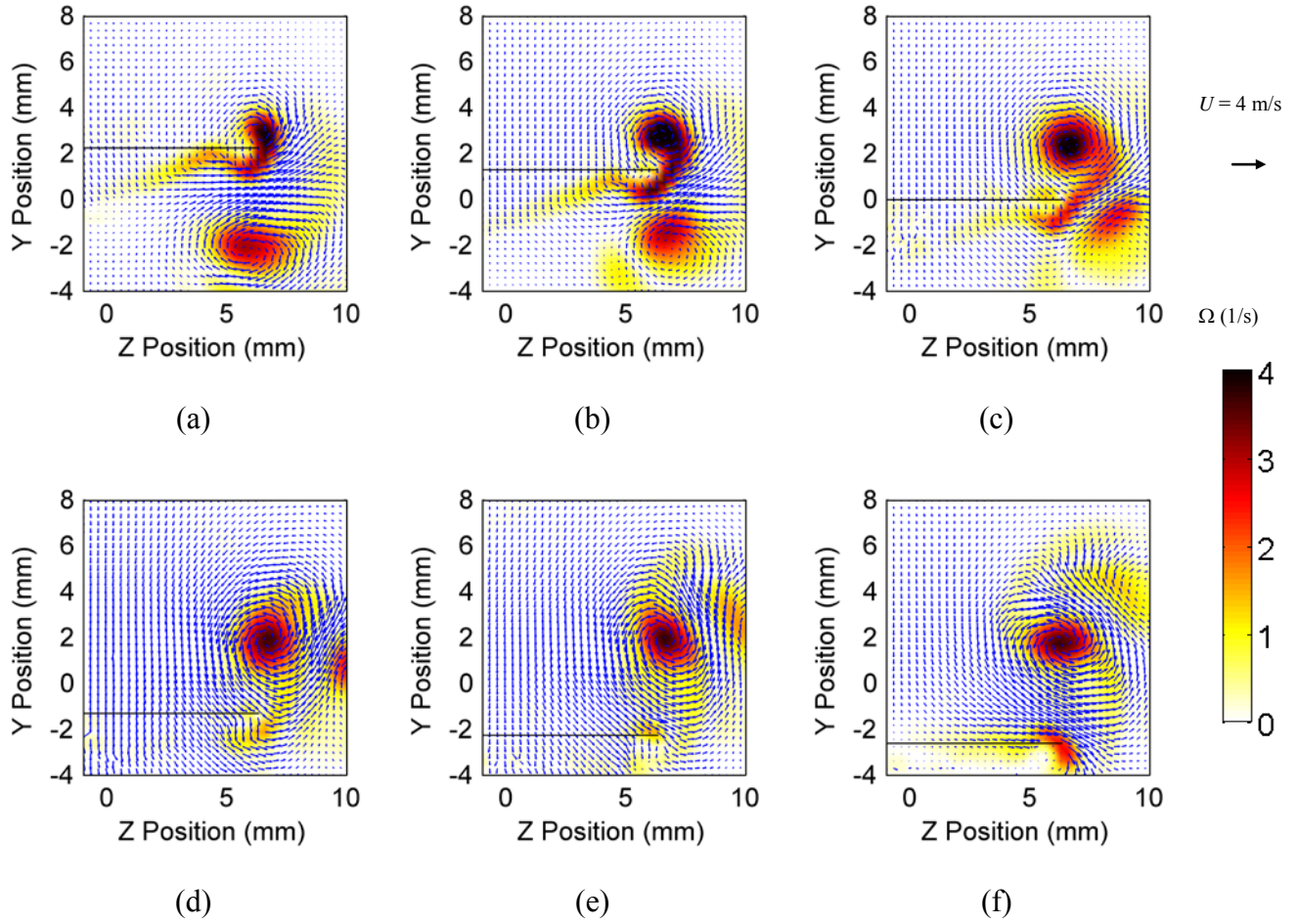


**Figure 24: The y-z plane (at  $x = -8$  mm) flow field at different oscillation phases. From top left to bottom right, the phases are (a) 120, (b) 150, (c) 180, (d) 210, (e) 240, and (f) 270 degrees.**

As the analysis plane moves closer to the fan tip, the effects of the out of plane flow begin to become apparent. Figure 25 illustrates the flow field and vorticity plots at  $x = -4$  mm. The generation of the vortex is nearly identical to that found upstream in Figure 24 ( $x = -8$  mm), however once the vortex detaches it begins to diminish more quickly. The clockwise rotating vortex, seen in Figure 24, is still present at the beginning (Figure 25 (a)) although it is weak and dies out very rapidly. Also, the two tails observed at  $x = -8$  mm are no longer present. It is likely

that the vortex is experiencing out of plane effects inherent in the three dimensionality of the flow at this point. These effects do not seem to affect the overall position of the vortex, however.

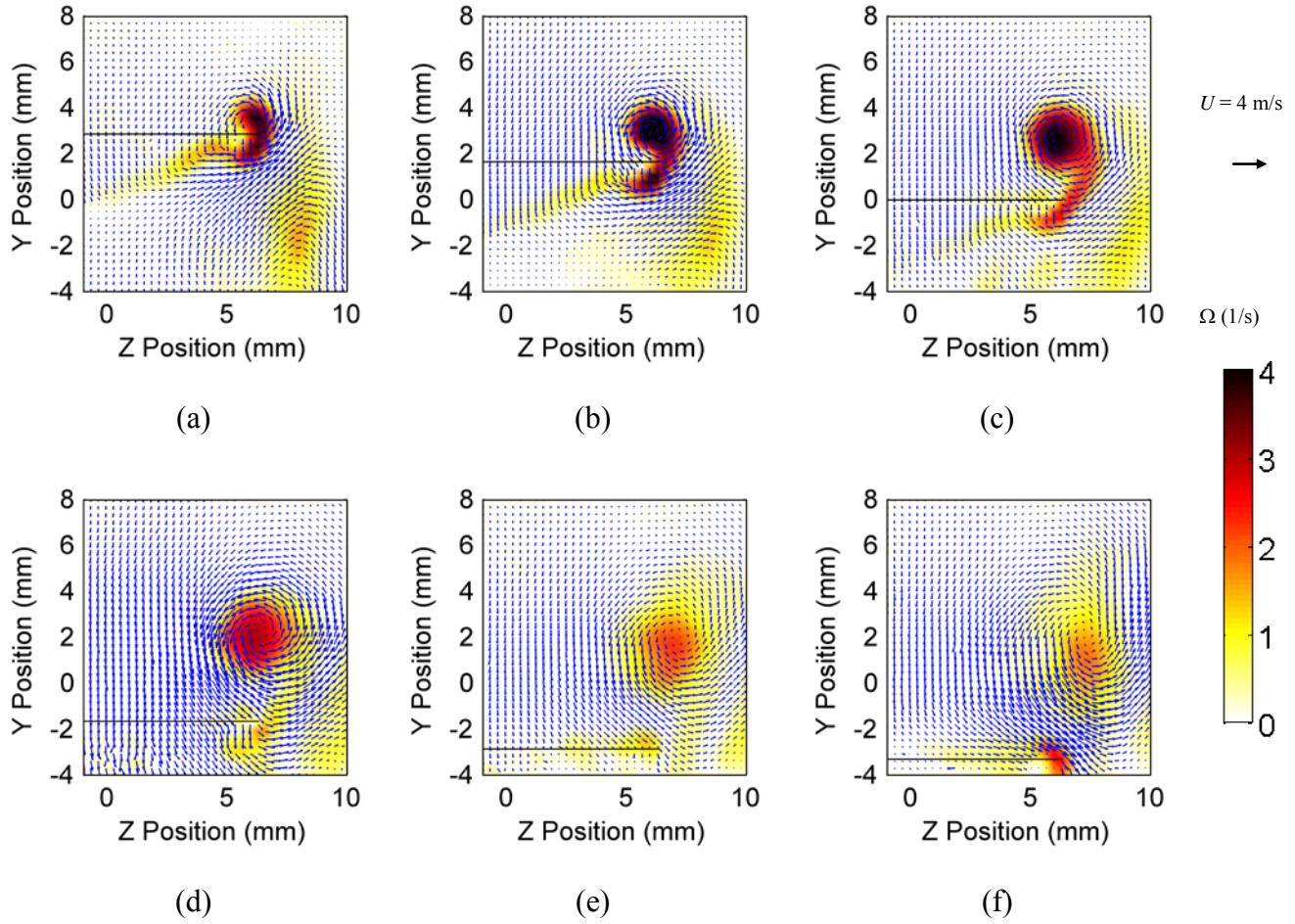


**Figure 25: The  $y$ - $z$  plane (at  $x = -4 \text{ mm}$ ) flow field at different oscillation phases. From top left to bottom right, the phases are (a) 120, (b) 150, (c) 180, (d) 210, (e) 240, and (f) 270 degrees.**

As the flow plane approaches the corner where the two edges meet, the effects of the three dimensionality of the flow become even more apparent. Figure 26 shows the  $x = -2 \text{ mm}$  (Figure 26 (a) through (c)) and  $0 \text{ mm}$  (Figure 26 (d) through (f)) flow planes. At  $x = -2 \text{ mm}$  the

vortex begins to stretch towards the center of the fan. This causes the center of the vortex to also be pulled toward the center of the fan. By the time the flow plane reaches the tip of the fan ( $x = 0$ ), the vortex itself has been moved towards the center of the fan with a greatly diminished magnitude. It can be assumed that the  $y$ - $z$  plane vortex is being entrained by the  $x$ - $y$  plane vortex as evidenced by the large  $y$ -directional flow present in the  $x = 0$  mm flow plane near the centerline of the fan where it is then ejected in the orthogonal direction. In effect, the 3-dimensional effects are apparent and unavoidable in this region.

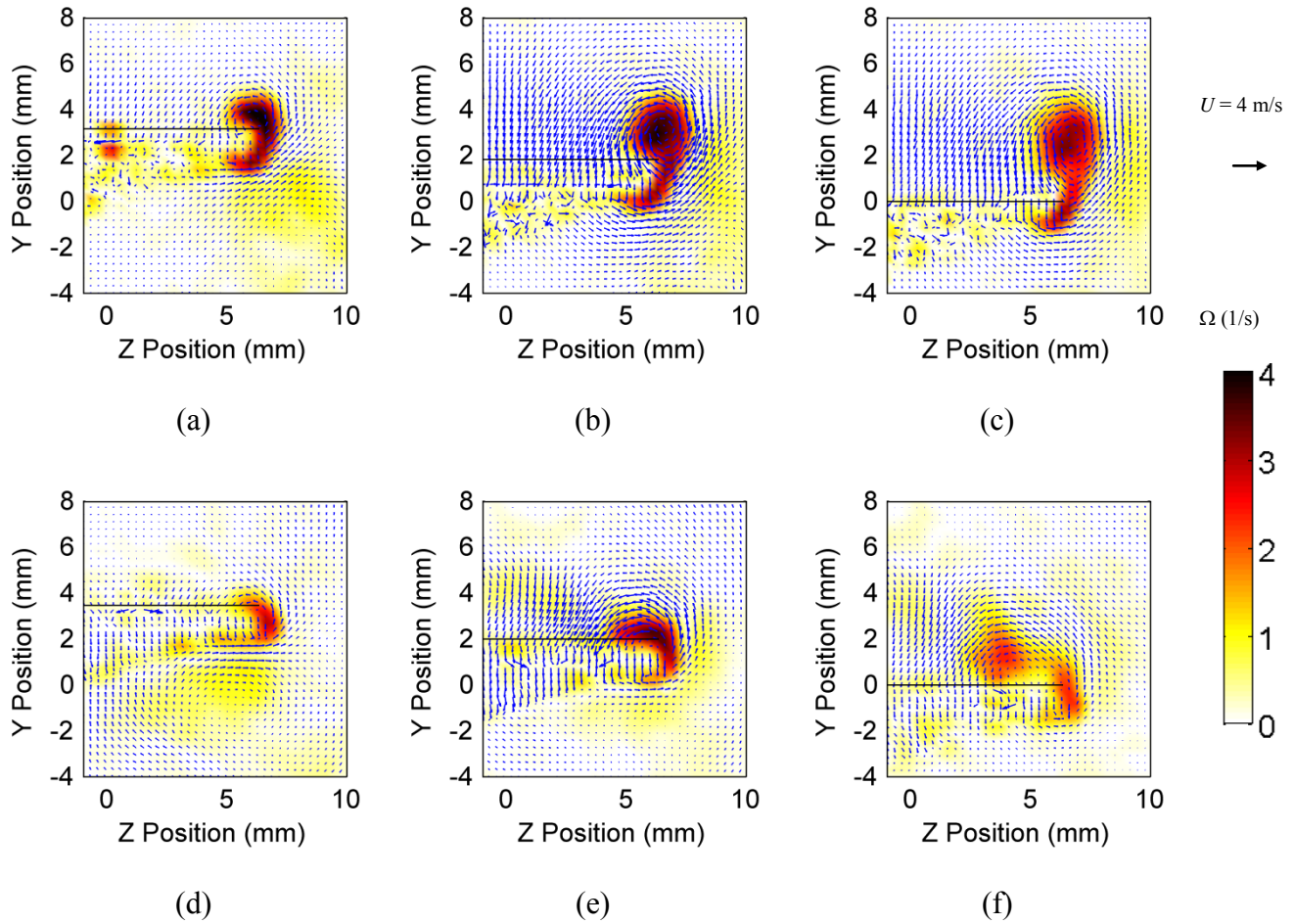


**Figure 26: The  $y$ - $z$  plane flow field at  $x = -2$  mm (top) and  $x = 0$  mm (bottom) for different oscillation phases.**

**From left to right, the phases are (a & d) 120, (b & e) 150, and (c & f) 180 degrees.**

These and other results are analyzed to get a clearer understanding of the vortex movement. The location of the vortex center is shown in Figure 27 for multiple phases and different values of  $x$ . Interestingly, from  $x = -8$  mm up to  $x = -2$  mm the vortex position remains relatively unchanged throughout the oscillation cycle. However, it abruptly changes further downstream and moves quickly towards the center of the fan. Just off the tip of the fan, there is a vortex present in later stages of the oscillation ( $270^\circ$  and  $315^\circ$  curves only). A vortex is not being formed in this plane by the sharp edge of the fan; rather, it is most likely a consequence of the vortex just upstream ( $x = 0$ ) being pulled downstream due to the dominant  $U_x$  at the fan tip. This effectively moves the vortices above and below the fan which limit the loss of flow over the edge. This inward motion was observed in previous work [70] as a positive (towards the centerline)  $U_z$  from  $x > -2$  mm. The motion of the vortex in this region further enforces that conclusion.

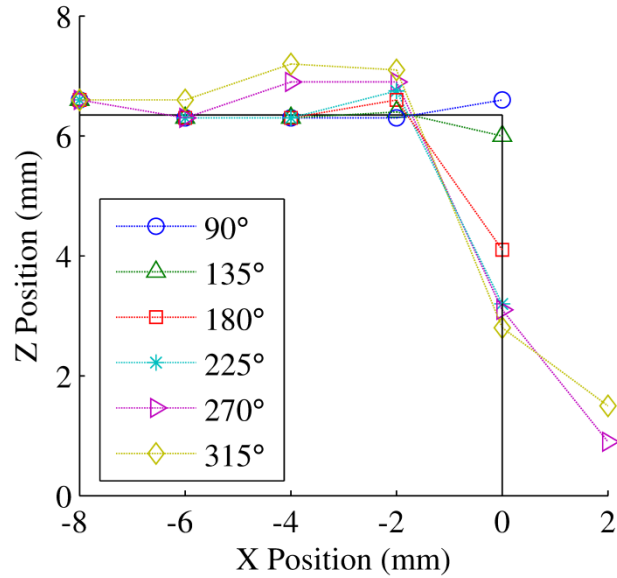


**Figure 27: Location of the vortex center at different phase steps. The black line represents the fan blade.**



The  $x$ - $y$  plane similarly experiences a pronounced effect from the out of plane flow as its proximity to the corner decreases. Figure 28 shows the flow near the centerline of the fan. It is similar to that found in previous work where the vortex is formed and travels downstream as it dissipates. However the flow halfway from the center of the fan to the edge experiences quite a different effect (Seen in Figure 29). The vortex is formed similarly to what is seen at the centerline. However, once detachment has occurred, the vortex actually increases in intensity before dissipating. This is most likely due to the lack of movement of the vortex. The vortex remaining in a relatively stable position uses up less energy while also still benefitting from the flow generation of the piezofan itself.

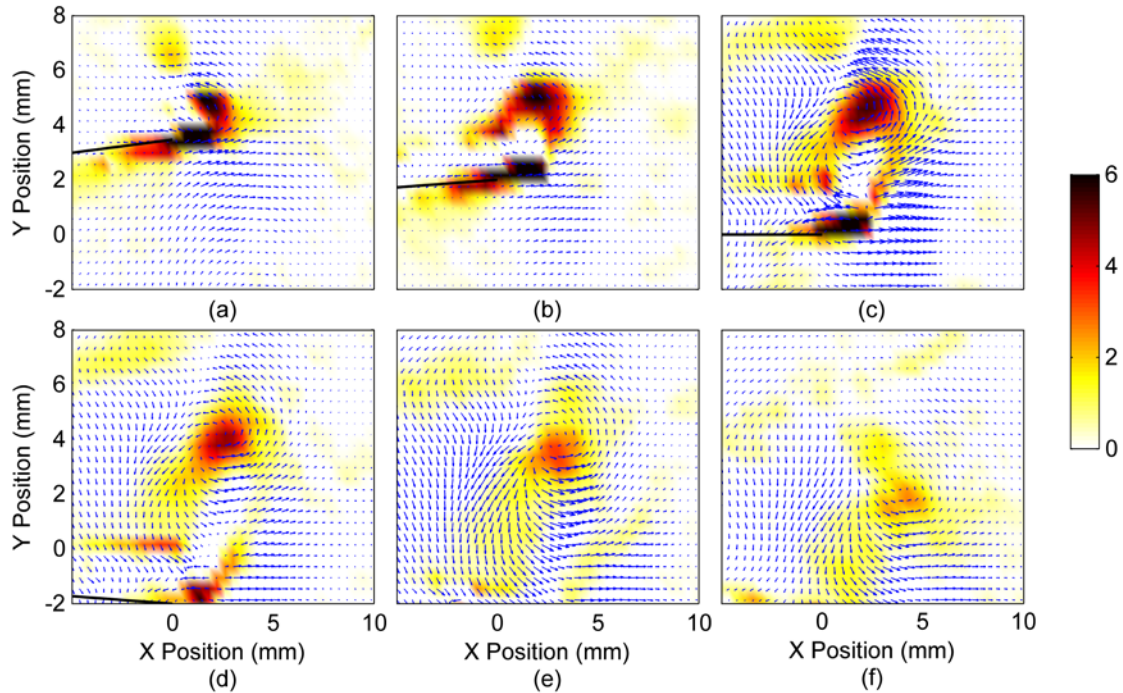


**Figure 28: The  $x$ - $y$  plane (at  $z = 1$  mm) flow field at different oscillation phases. From top left to bottom right, the phases are (a) 120, (b) 150, (c) 180, (d) 210, (e) 240, and (f) 270 degrees.**

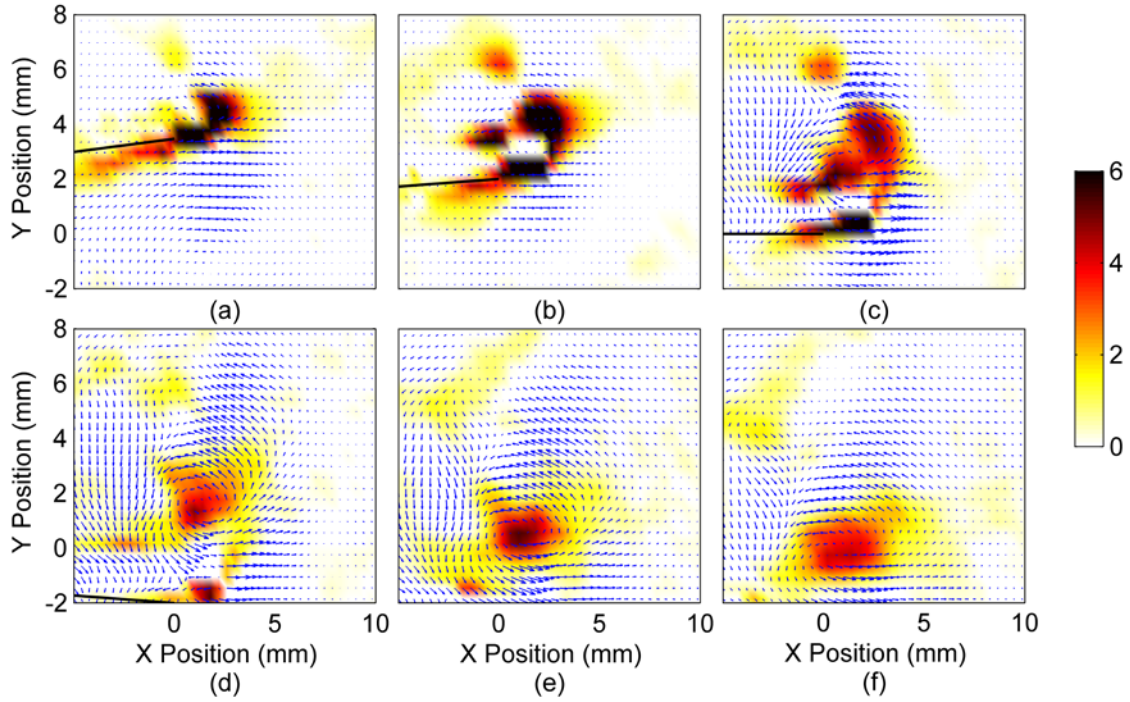


**Figure 29: The  $x$ - $y$  plane (at  $z = 3$  mm) flow field at different oscillation phases. From top left to bottom right, the phases are (a) 120, (b) 150, (c) 180, (d) 210, (e) 240, and (f) 270 degrees.**

Near the edge of the fan (seen in Figure 30), the vortex present later in the oscillation is not one that was generated by the sharp edge of the fan tip. There is, in fact, no apparent vortex generation as seen closer to the centerline of the fan. The major flow that is seen (Figure 30 (a to c)) is that generated by the sharp edge of the fan blade which happens to be the  $y$ - $z$  plane vortex. This is much like that seen in Figure 27 where the vortex is most likely one that has been stretched by entrainment into the flow plane.

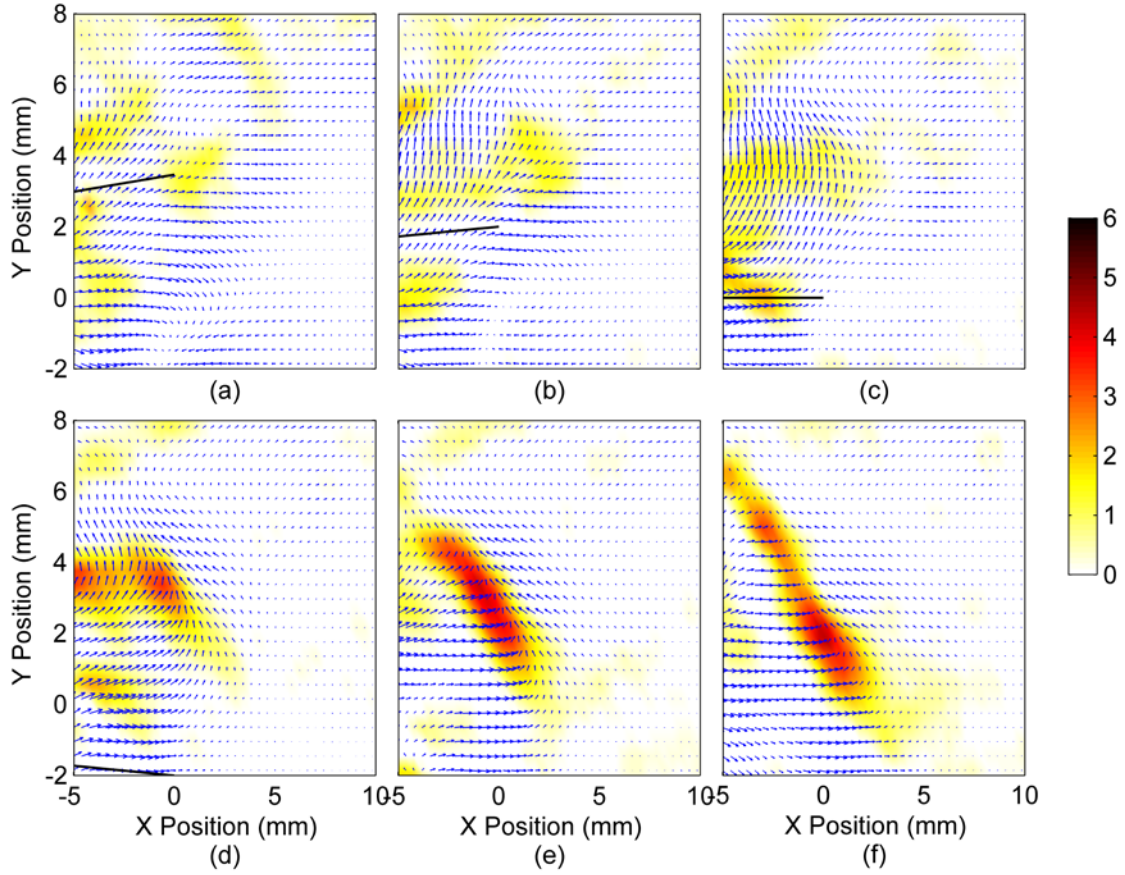


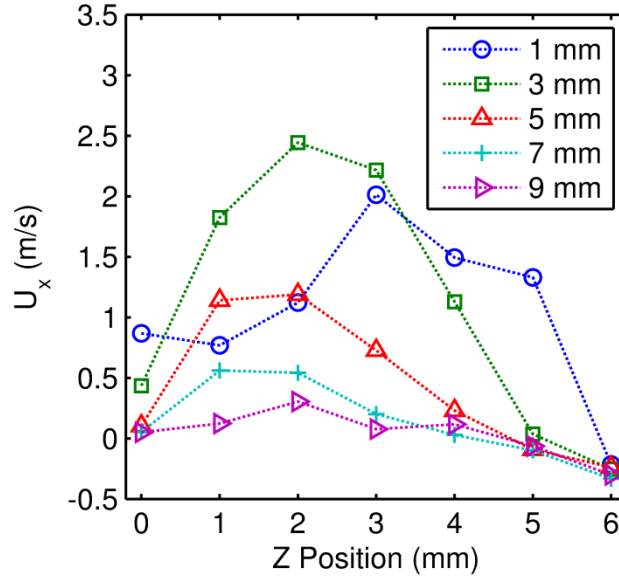
**Figure 30: The  $x$ - $y$  plane (at  $z = 5$  mm) flow field at different oscillation phases. From top left to bottom right, the phases are (a) 120, (b) 150, (c) 180, (d) 210, (e) 240, and (f) 270 degrees.**

These findings indicate that, in order to enhance  $U_x$  at the fan tip, sidewalls are the most apparent option. Limiting the vortex generation at the fan tip may yield unreasonable results, but eliminating the vortices that form off the edge of the fan would serve to be beneficial. However, care must be taken to limit the amount of obstruction above and below the fan as well as upstream. It is also apparent that the vortex location and movement plays a very important role in the inherent flow in an unbounded cantilever.

## 2.6 INLET AND OUTLET FLOW

Building off of two-dimensional analyses in the literature, one might assume that the cycle-averaged flow velocity would be greatest at the centerline ( $z = 0$ ) of the fan. In sidewall bounded analysis [52], this is precisely the case. However, when considering an unbounded cantilever vibrating at larger amplitudes (as is the case in the current study), this is not necessarily the true. In Figure 31, the cycle-averaged velocity profiles are shown at different downstream positions, presented in terms of the  $U_x$  velocity component. The highest  $U_x$  occurs at locations away from  $z = 0$ . In the case of just beyond the fan tip ( $x = 1$  mm), the maximum velocity occurs at  $z = 3$  mm, which is nearly half way between the center and side edge of the fan envelope. As the flow progresses further downstream, the point of maximum velocity starts drifting towards the center of the fan. However, peak velocity at the center is not observed even for a downstream location of  $x = 9$  mm. This type of phenomenon has been seen in heat transfer [51] with piezofans as well, where the point of maximum thermal performance for a fan oriented normal to a heated surface rarely occurs at the exact center of the vibration envelope. In that study, fans under investigation included similar fan lengths and widths as what was considered in the current study. The vibration amplitudes and frequencies also cover the range investigated here. They also considered very wide fans and found that the greatest convection enhancement was still found away from the center of the fan. Therefore, although it is rational to expect a two-dimensional flow at the  $z = 0$  centerline for extremely wide fans, the effect of the three-dimensional nature of the flow near the corners causes the point of maximum velocity and thermal convection to be pulled away from this centerline.

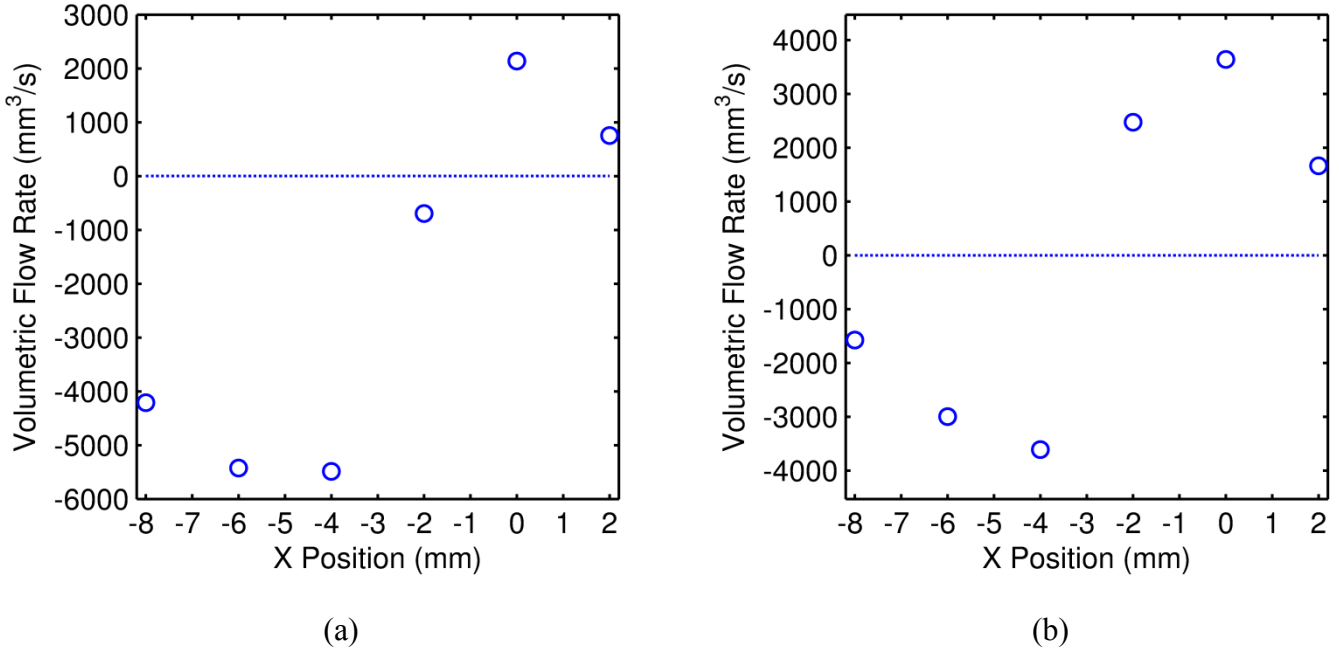




**Figure 31: Flow velocity of  $U_x$  at  $y = 0$  with varying  $x$  distances away from the tip of the fan blade.**

The motivation for much of this research is to inform the design process for a fan enclosure. For the applications of most interest, the fan will undoubtedly need to be mounted within some sort of fixture. It is important that the presence of the enclosure walls does not greatly diminish the performance. Ideally, this design would even allow for an increase in performance. The idea of using the flow field data to determine the optimal placement of sidewalls was addressed in a previous paper [70]. The finding was that, because near the fan tip, flow was moving towards the fan, the enclosure sidewalls should terminate at an upstream location of approximately 1-2 mm in order to allow this inflow to be maintained. This was based on the volumetric flow rate, which was analyzed assuming the sidewalls only reached as high as the oscillation envelope at each unique location along the length of the fan ( $x$ -direction). Here, we allow the inspection domain (the distance from the cantilever in the  $y$ -direction) to change, which has an impact on the flow rate values computed, and consequently modified conclusions are reached. The effective volumetric flow across the  $y$ - $z$  plane can be seen in Figure 32 (a) and

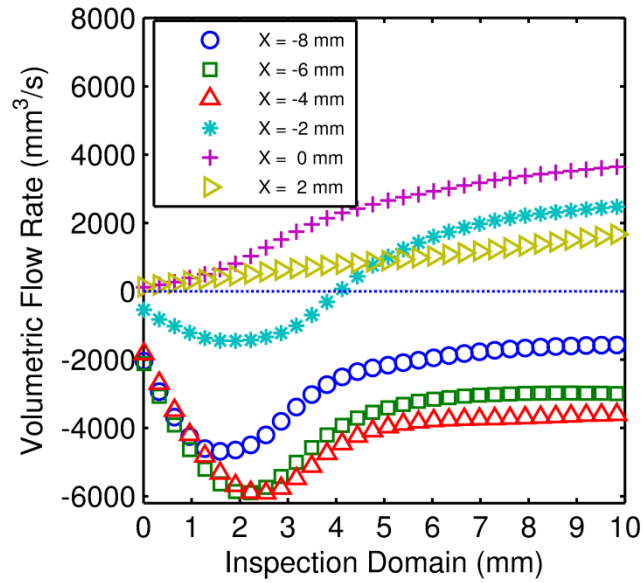
(b) when the inspection domain is only the oscillation envelope (Figure 32 (a)) and for the entire observed flow field (Figure 32 (b)), respectively. Positive flow rate denotes flow traveling toward the fan itself. Therefore the ideal enclosure would allow this flow to enter but prevent the flow from escaping in the regions with negative volumetric flow rate values. Note that the  $x$  location where the sign of flow rate changes from negative to positive is somewhere between  $x = -2$  mm and  $x = 0$  in Figure 32 (a), but when allowing the analysis domain to increase to the extreme edges of our PIV field of view, this transition point is found as far back as possibly 3 mm upstream from the tip (somewhere between  $x = -4$  and  $-2$  mm).



**Figure 32: Comparison of the volumetric flow rate in the z-direction (positive is towards the fan) with a control surface that is (a) the oscillation envelope and (b) the entire flow field domain.**

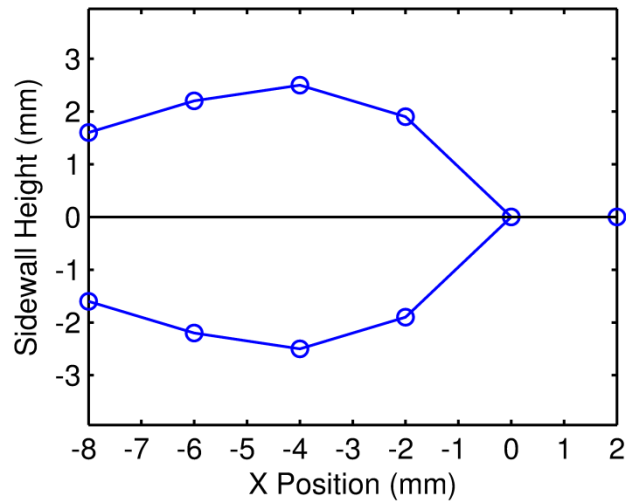
Allowing the  $y$  value (representing the extent of the virtual enclosure walls) to be variable, an optimized side wall design can be determined. For each  $x$  location along the fan blade, an effective control surface can be determined by finding the point (in the  $y$ -direction)

where the volumetric flow rate no longer changes. Such a condition suggests that even if the sidewall height in the  $y$ -direction were increased substantially beyond this value, the overall flow rate values would not change. Figure 33 shows the results of flow rate given a variable enclosure height. For  $x = 2$  mm and  $x = 0$ , the entire curve yields a positive flow rate (traveling toward fan envelope in the  $z$ -direction). For the three furthest upstream locations ( $x = -8$ ,  $-6$ , and  $-4$  mm), the flow rate is always negative, but an additional feature worth noting is the existence of a minimum flow rate in each of these three curves. The  $x = -2$  mm curve also contains a minimum value, but in contrast, crosses the zero flow rate line from negative to positive values. The existence of a minimum value for these four curves is important in that it represents the wall height at which flow is no longer traveling away from the fan but is beginning to have a positive  $U_z$  value. Therefore, the  $y$  location which corresponds to this minimum point represents the ideal enclosure height, one that prevents flow from leaving the vibration envelope, but still accepts the flow that would otherwise enter. This can also be used to determine where the domain size is sufficient for analysis of volumetric flow leaving or entering the cantilever area. Once a curve levels off, there is no longer a need to increase the inspection domain height in that region.



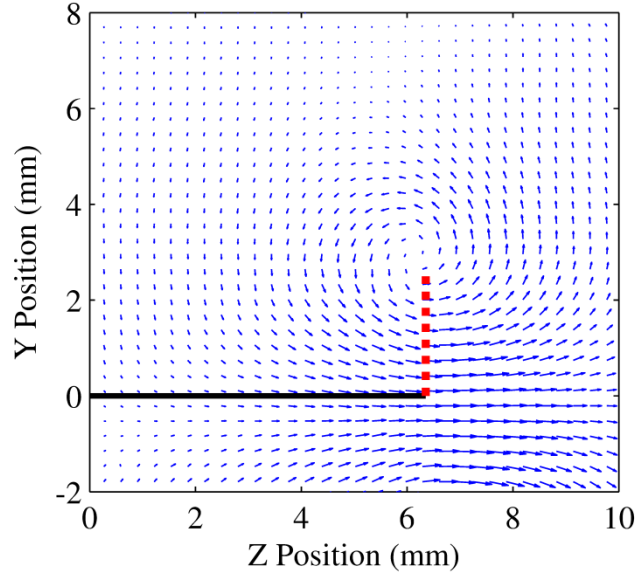
**Figure 33: Volumetric flow rate in the z-direction (positive is towards the fan) based on an increasing inspection domain in the y-direction.**

Figure 34 shows a graphical representation of the general shape that the fan would take based on the optimal values found in Figure 33. Essentially, the optimal value resides at the location of the minimum flow rate on each curve. If there is no minimum and the slope is positive, there is no need for a sidewall at that location. Conversely, if there is no minimum and the slope is negative, the sidewall at that location should be as large as possible.



**Figure 34: Geometrical representation of a sidewall that would block only the flow lost over the sides of the fan blade.**

Also worth noting is that the location of the minimum is most likely related to the vortex position. This can be seen more clearly in Figure 35. As such, it is likely that the sidewall geometry is only a starting point and will change due to the nature of the flow field changing as well. More specifically, the introduction of the sidewall itself would cause a change in the flow field and alter the dimensions of the optimal sidewall geometry. This does not necessarily diminish the findings, however, as this provides a starting point that is based on the actual flow fields.



**Figure 35: The cycle averaged flow field in the y-z plane for  $x = -4$  mm. This demonstrates how the volumetric flow rate minimum corresponds to the vortex position. The dotted red line represents the inspection domain for the volumetric flow rate minimum.**

## 2.7 CONCLUSION

The flow fields for a piezoelectrically oscillating cantilever operating at 62.5 Hz with peak vibration amplitudes between 2 mm and 4 mm were analyzed in order to better understand the flow which is generated without the presence of external boundaries or walls. Both the  $x$ - $y$  and  $y$ - $z$  planes were analyzed at multiple locations ranging from positions where primarily two dimensional flow can be observed to locations where flow is affected by multiple sharp edges.

It was found that, similar to Kimber et al. [42], a portion of the flow comes from above and below the fan as well as upstream. Although flow does not enter from the upstream portion of the side of the fan ( $x < -2$  mm), boundaries at these locations would serve to limit the flow that

is effectively lost in the  $z$ -direction. It is also apparent that the prominent  $U_x$  at the tip of the fan affects the vortices shed by the edge of the fan by entraining them towards the center of the fan. This effectively moves the vortices above and below the fan which limit the loss of flow over the edge. This inward flow was observed in previous work as well [70]. There are also vortices that form later in the oscillation cycle past the tip of the fan and are not generated by any sharp edge at that location. It is likely that this is an upstream vortex that has been stretched via entrainment.

These findings indicate that, in order to enhance  $U_x$  at the fan tip, sidewalls could be tailored to a geometry that only restricted flow that would otherwise be lost off the side of the fan. This sidewall geometry would likely be elliptical in shape.

It is also apparent that the vortex location and movement plays a very important role in the inherent flow in an unbounded cantilever. Under certain geometrical and operational circumstances, the most dominant flow from the tip of the fan blade does not occur along the centerline of the fan. Rather, the dominant flow occurs half way between each edge and the centerline.

### 3.0 THRUST MEASUREMENT CHARACTERIZATION

Now that an adequate understanding of the overall flow field has been presented, a basis for thrust performance should be generated. This is necessary in order to understand what one could expect for an unbounded cantilever given a set of operational and geometric parameters. In order to properly characterize thrust as a simple function of geometry and operational characteristic, multiple different cantilever types were used. Table 3 gives a complete breakdown of all the fans used, the relevant dimensions, and the operational parameters.

**Table 3: The relevant dimensions and operating parameters of all of the piezoelectric fans investigated.**

	$L_p$ (mm)	$L_b$ (mm)	$D$ (mm)	$t_p$ (mm)	$t_b$ (mm)	$A$ (mm)	$\omega$ (rad/s)	$\omega_n$ (rad/s)	Material
<b>Fan 1</b>	32.0	36.5	12.7	0.53	0.27	1.8-14.1	370-396	383	Mylar
<b>Fan 2</b>	24.4	23.0	12.7	0.29	0.10	1.5-3.3	719-748	729	S. Steel
<b>Fan 3</b>	24.2	14.9	6.4	0.44	0.11	1.6-1.7	1514-1552	1533	S. Steel
<b>Fan 4</b>	24.2	24.2	25.4	0.44	0.11	0.96-1.8	723-748	735	S. Steel
<b>Fan 5</b>	32.0	36.5	25.4	0.53	0.27	3.0-4.8	383	---	Mylar
<b>Fan 6</b>	24.4	23.0	25.4	0.29	0.10	1.6-2.2	672	---	S. Steel



### 3.1 EXPERIMENTAL SETUP AND PROCEDURE

The piezoelectrically oscillating cantilevers (piezofans) used in this section were a mix of commercially available (RFN1-005 and RFN1-LV-02 from Piezo Systems) and lab manufactured fans. Fan blades comprised of both Mylar and stainless steel were used. The exposed portion of the cantilever is the part of the fan that experiences the largest vibration amplitudes and therefore is the main contribution to the fluid structure interaction. A total of six unique fans or fan combinations are considered in this work. A visual representation of these can be seen in Figure 36. Of note is that fan 5 and 6 actually consist of two separate fans positioned with a very small gap between them (less than 0.5 mm), and are forced to operate in phase at the same frequency and amplitude. To verify this condition was met, two laser displacement sensors (Keyence LK-G157) were used to monitor vibration signals for each fan. A two channel function generator (Tektronics AFG 3102) with phase lock control was used to adjust the input signals such that the outputs were in phase within  $1^\circ$  and the vibration amplitudes were identical within 1%. Due to slight differences in each fan, their natural frequencies are not identical. However, for the fan 5 and fan 6 cases, this difference was less than 5%.

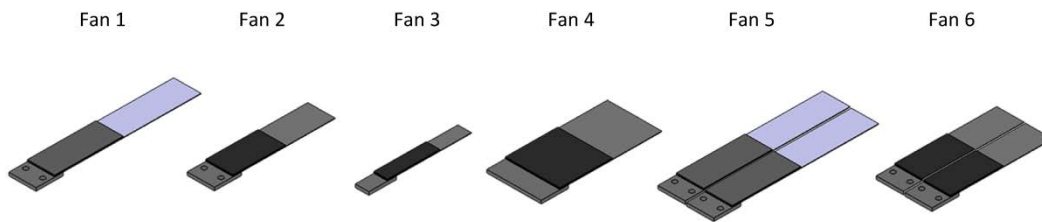


**Figure 36: Visual representation of the size and shape of all the fans used for thrust measurements.**

In order to measure the thrust produced by the fan, a high precision digital scale (Sartorius CP Series CPA 3245) was used. This scale was set to output mass values to a computer at a frequency of 5 Hz which could then be converted to a thrust value. It should be noted that the piezofans themselves operate at frequencies at least an order of magnitude higher than this, and therefore the scale is unable to measure the instantaneous thrust signal, but is still able to quantify the cycle-averaged result which is the primary metric of interest. The fan is attached to an aluminum bracket and large (0.3 kg) damping mass which is then placed on the scale. This is done to limit the components of force orthogonal to the thrust direction, which represent the recoil force from the back and forth movement of the fan blade. Although these forces have a zero mean, they can produce physical instability in the setup if their effect is not properly reduced. Previous tests have found that the difference in amplitude between a rigidly mounted fan and one mounted to the large mass to be less than 2% [70]. The assembly can be seen in Figure 37. The high precision of the scale causes the measurement to potentially be affected by the errant flows in the room. Therefore, to isolate the scale from these random fluctuations, the system was placed inside of an enclosure of dimensions 305 mm x 610 mm and 406 mm.

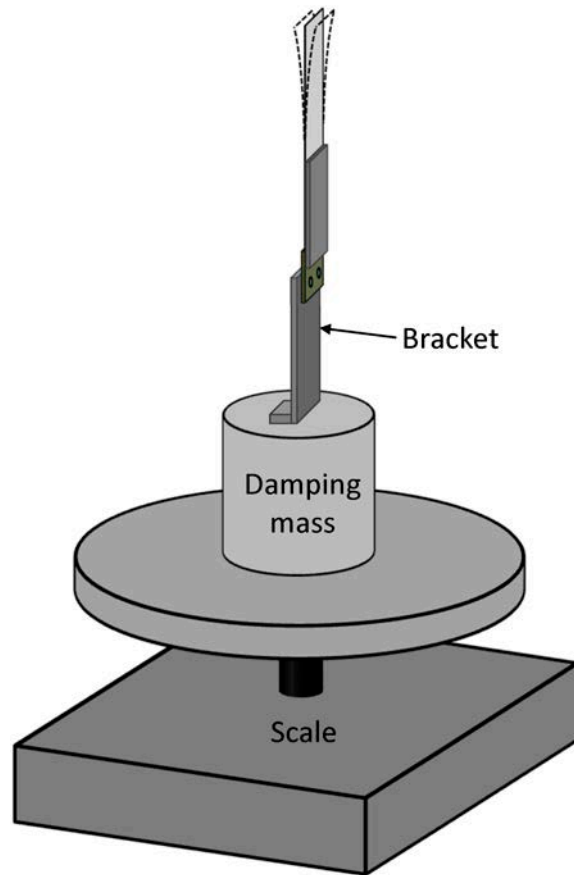


**Figure 37: Graphical representation of the orientation and position of the thrust measurement setup.**

The piezofan is mounted to the bracket and damping mass which is then placed on a sheet of magnetic field isolating material (two pieces of a 63.5 mm wide Mumetal foil sleeve laid flat). All of this is placed on the scale which is entirely contained within the enclosure. All necessary electronic equipment is then turned on without an actual output to the fan. The entire system is then allowed to sit for a period of at least one hour to allow for all errant flows within the enclosure to dissipate, and allow magnetic field interference from any electric equipment to stabilize.

To gather a baseline reading of zero thrust (i.e., the weight of the damping mass, bracket and fan), data is collected for approximately 10 seconds before the signal to the fan is turned on. Once the piezofan is provided with a signal it is allowed to run for at least 20 seconds total in order to ensure that the thrust is stabilized. Considering the number of data points collected per second (rate of 5 Hz), this allows for a total of at least 100 data points for the thrust measurement and 50 for the baseline or zero thrust measurement for each unique experiment. Within the thrust data set, the first 25 data points were discarded, as they represent the transition period where the thrust is unsteady and thus not reliable.

In general, the frequency range was kept within the bandwidth (70% of the maximum tip deflection) near the natural frequency. Therefore, the results in this work can be applied to the fundamental mode of vibration. Far away from this condition, they might not apply, especially when higher vibration modes are considered. Although the frequency ranges for each fan are different, the frequency was typically varied in  $\pi$  rad/s (0.5 Hz) steps to generate a number of data points for each frequency sweep.

### 3.2 THEORY AND DATA ANALYSIS

The dimensions include  $L_p$ ,  $L_b$ , and  $D$ , as well as the piezoelectric patch thickness ( $t_p$ ) and blade thickness ( $t_b$ ). The operating parameters of interest in thrust characterization are the oscillation amplitude ( $A$ ), oscillation frequency range ( $\omega$ ), and natural frequency ( $\omega_n$ ). It should be noted that fan 4 and fan 6 are geometrically similar, except fan 6 is comprised of two smaller fans. Therefore, similar performance of these two fans helps validate the approach used with fans 5 and 6 to create a wider fan.

Let us start by considering the general incompressible, 2-dimensional momentum equations, neglecting body forces:

$$\rho \left( \frac{\partial \vec{u}}{\partial t} + \vec{u} \nabla \vec{u} \right) = -\nabla P + \mu \nabla^2 \vec{u} \quad (2)$$

Although the flow itself is unsteady by nature, we are primarily concerned with the cycle-averaged thrust, and therefore the unsteady term can be ignored, which leaves the following equation:

$$\vec{u} \nabla \vec{u} = -\frac{1}{\rho} \nabla P + \nu \nabla^2 \vec{u} \quad (3)$$

A scaling analysis is now performed to facilitate better understanding of dimensionless terms that dictate thrust forces. From detailed PIV studies [52], it is reasonable to assume that the scale of the cycle-averaged downstream velocity is on the order of the maximum tip velocity ( $u \sim \omega A$ ). In addition, a quantity measured in the  $y$ -direction would logically scale with vibration amplitude ( $y \sim A$ ). For the  $x$ -direction, the scale is initially taken to be an arbitrary length scale ( $x \sim \lambda$ ). From the continuity equation, a scaling argument can be made for the  $y$ -directional velocity ( $v$ ) as shown in Eq. (4).

$$v \sim \frac{\omega A^2}{\lambda} \quad (4)$$

The pressure term of Eq. (3) can be taken as the primary source of thrust generation and should not be neglected in favor of the viscous or inertia forces. We next let the gradient of pressure scale as the ratio of a pressure difference  $\Delta P$  and an appropriate length scale, depending on which component of the momentum equations are of interest. For investigating thrust, this is the downstream direction ( $x$ -direction). Making use of the scaling arguments proposed, the  $x$ -momentum equation becomes:

$$\left[ \frac{\omega^2 A^2}{\lambda} \right] + \left[ \frac{\omega^2 A^2}{\lambda} \right] = \left[ \frac{1}{\rho} \frac{\Delta P}{\lambda} \right] + \left[ \frac{\nu \omega}{\lambda} \left( \frac{A}{\lambda} + \frac{\lambda}{A} \right) \right] \quad (5)$$

where the brackets signify the magnitude (scale) of each term is being considered. This reveals that both inertia terms (left hand side of Eq. (5)) are comparable and depending on the relative magnitude of  $A$  and  $\lambda$ , the viscous terms (non-pressure terms on right hand side of Eq. (5)) could either be neglected or dominate over the inertia terms. An additional intuitive relationship can relate the pressure difference ( $\Delta P$ ) to the actual thrust ( $T$ ), namely  $\Delta P \sim T/(AD)$ . In other words, the pressure scales with the thrust divided by the area over which the thrust is applied (we assume this area scales as the product of vibration amplitude and fan width). Making this substitution into Eq. (5) and dividing by  $\omega^2 A^2/\lambda$  yields the following:

$$[1] + [1] = \left[ \frac{T}{\rho \omega^2 A^3 D} \right] + \left[ \frac{1}{Re_A} \left( \frac{A}{\lambda} + \frac{\lambda}{A} \right) \right] \quad (6)$$

where  $Re_A$  is the oscillating Reynolds number [51, 52], defined in Eq. (1).

The magnitude of  $Re_A$  encountered for a macro-sized oscillating beam is typically  $O(10^2)$  or higher. Although  $\lambda$  is an arbitrary length scale used for convenience in the scaling analysis, it can be thought of as the downstream distance where the cycle-averaged velocity decays to a near-zero value. In order for viscous and inertia terms to be comparable, one of the two conditions must be met: (i)  $\lambda/A \sim O(Re_A)$  or (ii)  $A/\lambda \sim O(Re_A)$ . From briefly analyzing the PIV data from [52], it is reasonable to assume that  $\lambda \sim A$ , a condition suggesting that the inertia terms are much larger than the viscous terms, at least for the current geometries and conditions investigated in this paper. Therefore, a dimensionless thrust based on the assumed form of the pressure term can be defined as:

$$T^* = \frac{T}{\rho \omega^2 A^3 D} \quad (7)$$

and one would expect the magnitude of this dimensionless thrust to be  $O(1)$ .

Eq. (6) also yields insight into what one would expect to happen at lower Reynolds numbers. Once  $Re < 1$ , the viscous term on the right is likely to start being the dominant factor. Once that happens, there is little chance that vortices will be formed. As vortex formation is a factor propulsive thrust in this type of motion, it is likely that there will be no thrust generated. The downward stroke of the cantilever does produce a resulting force in the direction of desired thrust simply due to pushing against the fluid, but this is met with an equal force in the opposite direction during the upward stroke thus cancelling each other out over an entire oscillation cycle.

### 3.3 EXPERIMENTAL RESULTS

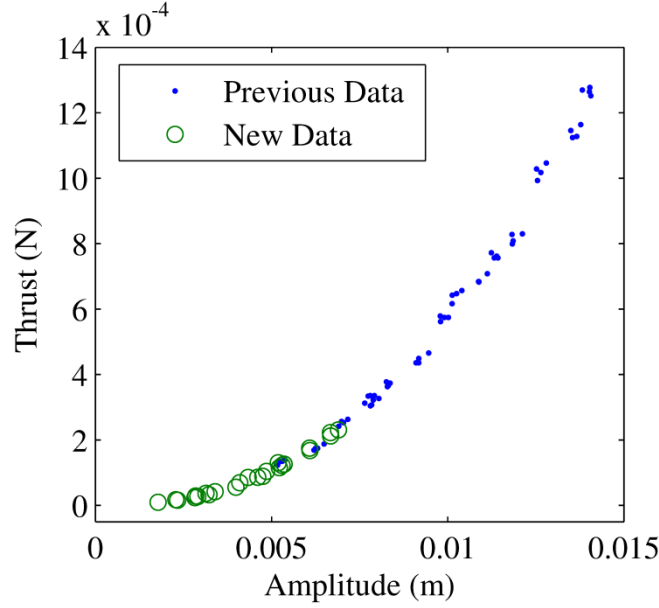


**Figure 38: Comparison of the previously collected data from [70] and the new data.**

As the analysis of this paper includes data from preliminary experiments [70]. That work has been published, but it is imperative to ensure that the same procedures produce similar trends for the sake of repeatability. This is because the same piezoelectric fan used in [70] was also employed in the current study, with the exception that lower thrust values (and amplitudes) were targeted here. The range was consciously chosen such that some amount of overlap existed between previous and new data sets. The comparison of results (thrust vs. amplitude) can be observed in Figure 38 and verifies the consistency between previous and current experimental results. Note that although Figure 38 displays thrust vs. amplitude, it does not capture the effect of frequency, since only a very narrow frequency band (59 Hz to 63 Hz) was considered. As expected, a decrease in amplitude causes a decrease in thrust, revealing the nonlinear relationship between these two parameters.



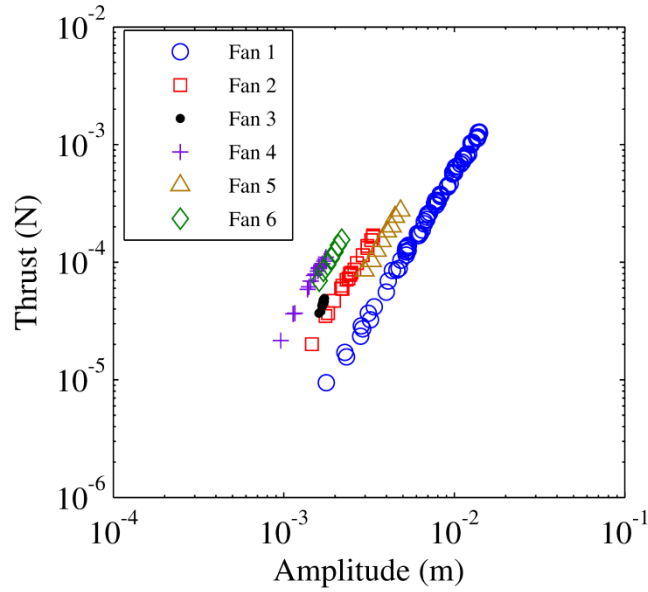


**Figure 39: Thrust data for each fan compared to their respective amplitude ranges.**

In Figure 39, the thrust is shown for all six fans. As expected, the thrust increases with amplitude, regardless of the fan geometry. The type of material and size of the blade dictates the achievable thrust and its range. The smallest of the six fans (fan 3) appears to be less sensitive to changes in frequency or amplitude. Fans 4 and 6 yield a similar trend, which is expected due to geometric similarity between the two. This also validates using data from fans 5 and 6 to represent a fan which is twice as wide as the original.

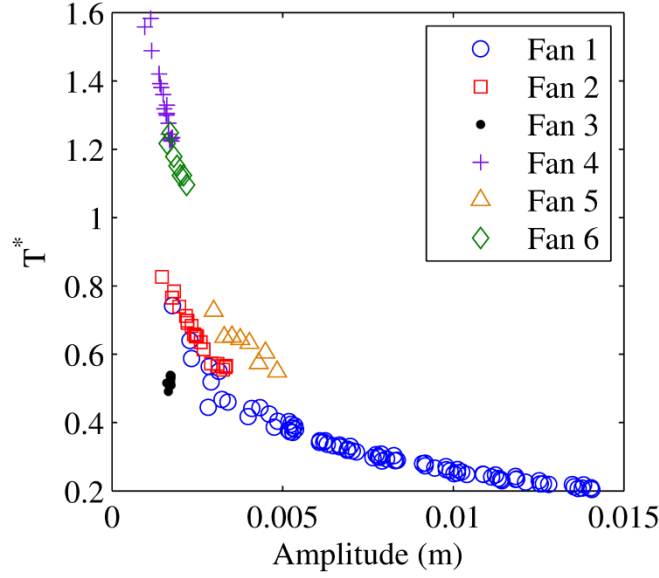


**Figure 40: The non-dimensional thrust for each fan compared to their respective amplitude ranges.**

The same set of data presented in terms of the dimensionless thrust (Eq. (7)) is shown in Figure 40. The values are for the most part  $O(1)$ , especially for small amplitudes, a characteristic predicted from the scaling analysis. It is also interesting that the data from fan 1 and fan 2 seem to follow a nearly identical trend. The only common trait between these two fans is their width ( $D$ ), and therefore suggests that  $T^*$  captures the effect of frequency and amplitude reasonably well. Compared to the potential curve that might predict  $T^*$  for fans 1 and 2, an additional curve could potentially be used to predict the trend from fans 4, 5, and 6, all of which are twice as wide as fans 1 and 2. Fan 3 is half as wide and therefore exists below the data from fans 1 and 2. It is worth noting that Eq. (7) does not take the length of the fan ( $L_b$ ) into account. In order to address this issue and compare to thermal performance characterization from Kimber and Garimella [51], we introduce the Strouhal number ( $St$ ) defined as:

$$St = \frac{\omega D L_b}{\nu} \quad (8)$$

The dimensionless thrust can now be expressed as a function of the Reynolds and Strouhal numbers in the following form:

$$T^* = C_1 (Re_A)^{C_2} (St)^{C_3} \quad (9)$$

where  $C_1$ ,  $C_2$ , and  $C_3$  are constants determined from a least squares fit of the data, which yielded 0.0106, -0.33 and 0.62 for  $C_1$ ,  $C_2$  and  $C_3$ , respectively. The fit of the data can be seen in Figure 41, revealing a reasonably close prediction as the rms error is 8.55% and the maximum error is 13.6%.

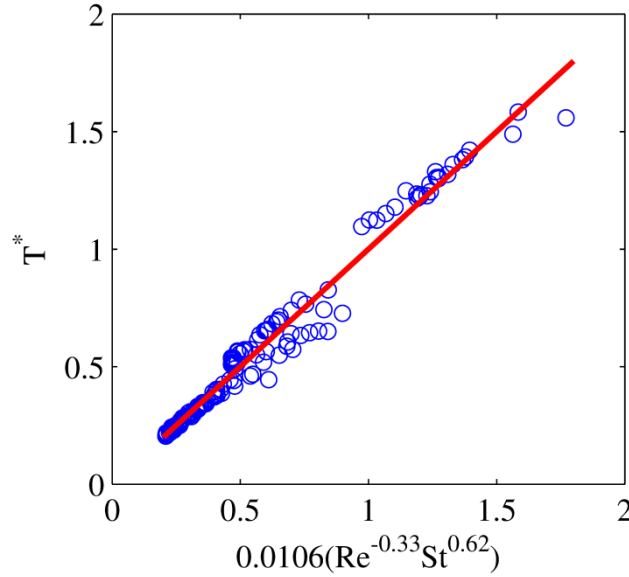


**Figure 41: The non-dimensional thrust with the curve fit using Reynolds and Strouhal numbers.**

Since this is an oscillating flow, another logical approach would be to express the thrust in terms of the Keulegan-Carpenter number [57], which was initially proposed based on experimental data from a cylinder and flat plate in an oscillating flow. It was found that the drag force could be predicted based on the product of the peak flow velocity and period of oscillation, normalized by the diameter or width of the cross section geometry. For the current study, the

oscillating flow velocity is simply replaced by the maximum tip velocity ( $\omega A$ ), and the period is simply expressed in terms of the frequency of oscillation such that the  $KC$  number becomes:

$$KC = 2\pi \frac{A}{D} \quad (10)$$

Note that although the local amplitude varies along the length of the fan from zero to a maximum value, the  $KC$  number as defined above is in terms of the maxim vibration amplitude. A curve fit can also be made relating the dimensionless thrust to this  $KC$  number as follows:

$$T^* = C_4 (KC)^{C_5} \quad (11)$$

where  $C_4$  and  $C_5$  are constants determined from a least squares fit of the data and are found to be 0.7 and -0.63, respectively.

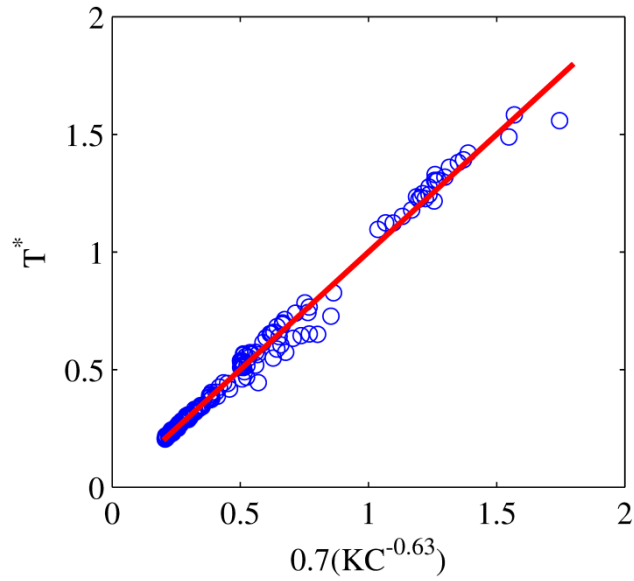


**Figure 42: The non-dimensional thrust with the curve fit using the Keulegan-Carpenter number only.**

The quality of this curve fit can be seen in Figure 42, and reveals a slightly tighter fit compared with the Reynolds and Strouhal number fit from Figure 41 as the rms error is 5.73%

and the maximum error is 12.0%. Another visual representation of the curve fit can be seen in Figure 43.

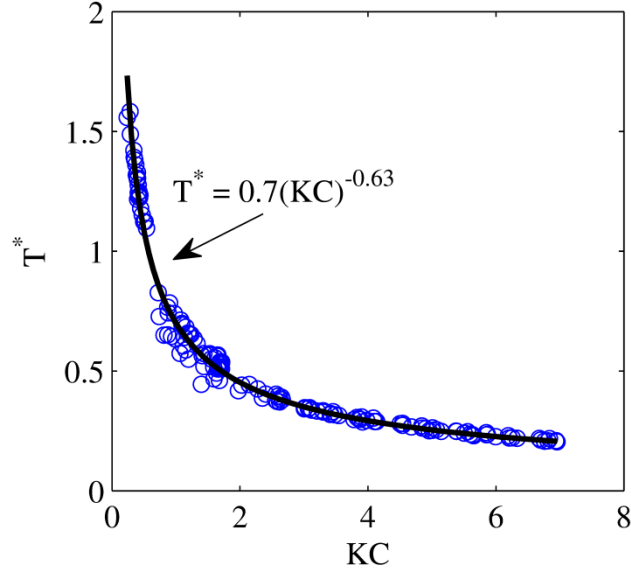


**Figure 43: Non-dimensional thrust as function of Keulegan-Carpenter number.**

For very small  $KC$  numbers, the vibration amplitude is very small compared to its width. One could suppose a two dimensional flow becomes applicable at this limit. From the data in Figure 43, we clearly see that the dimensionless thrust in the low  $KC$  region is extremely sensitive on the value of the  $KC$  number. As the  $KC$  number increases (fan with amplitude much larger than its width), this sensitivity (slope of the  $T^*$  vs.  $KC$  curve) becomes less important. It is useful to quantify the proportionality of the actual thrust as a function of the operating parameters. Substituting Eqs. (7) and (10) into Eq. (11) reveals these proportional relationships as:

$$T \propto \omega^2 A^{2.37} D^{1.63} \quad (12)$$

It is clear that amplitude has the most impact on the thrust force. Although the other two variables contribute to the thrust by a lesser degree, neither carry a linear relationship nor are less

than one. This finding yields an interesting question: Why, in a clearly three dimensional flow, is the cantilever length not present? The fact is, although not readily apparent, its influence is built into the oscillation frequency ( $\omega$ ), whose value very much depends on  $L_b$ , since the fan operation takes advantage of resonance conditions. It should be noted that the fluid properties ( $\rho$  and  $\nu$ ) would also affect the frequency and achievable amplitude of the blade oscillation, but no conclusive statements are made here since all experiments were performed in the same fluid environment, namely air. Alternatively, consider the proportional relationship based on substituting Eqs. (1), (7), and (8) into Eq. (9):

$$T \propto \omega^{2.29} A^{2.34} D^{1.62} L_b^{0.62} \quad (13)$$

which, by contrast, includes the effect of the blade length ( $L_b$ ). However, once accounting for an analysis of a standard cantilever beam, one can express the proportional relationship between length and natural frequency as:

$$L_b \propto \frac{1}{\sqrt{\omega}} \quad (14)$$

Substituting Eq. (14) into Eq. (13) yields:

$$T \propto \omega^{1.99} A^{2.34} D^{1.62} \quad (15)$$

which is nearly identical to the relationships found in Eq. (12). Although fixed beam theory is not a perfect comparison to what was done in this paper, this reinforces the previous assumption that the blade length is accounted for in the effect of the oscillation frequency. This also provides an explanation why a 3-dimensional based flow can be accurately characterized by only looking at one geometrical factor ( $D$ ) rather than two ( $D$  and  $L_b$ ).

### 3.4 CONCLUSION

The second step in understanding the nature of oscillating cantilever thrust enhancement is to determine what factors contribute to the unenhanced thrust performance. Thrust force measurements were taken for multiple piezoelectrically oscillating cantilevers operating near resonance. Although a piezoelectric material was the driving force, these findings should be able to be applied to any oscillating cantilever. As different cantilever geometries and materials were analyzed, this also yielded different resonant frequencies and oscillation amplitudes. This facilitated the ability to vary every physical aspect of the cantilever considered in this paper.

An effort was made to normalize all of the thrust data and apply a single curve fit. A basic scaling analysis was conducted to elucidate a starting point for the normalization of the thrust. This dimensionless thrust was first expressed in terms of the Reynolds and Strouhal numbers. This yielded an adequate normalization with a maximum deviation of roughly 13.6%. A second approach focused on expressing the dimensionless thrust in terms of the  $KC$  number produced a better curve fit with smaller deviations between measured and predicted values. Although the  $KC$  number does not include length or fluid properties, those two factors are built-in to other operating parameters such as frequency and amplitude. In fact, blade length was shown to follow the concept of fixed beam theory in its relationship with frequency.

We present a simple and accurate characterization of the thrust force produced by an oscillating cantilever that is fixed at one end. One can now reliably determine the geometric and operational characteristic that an oscillating cantilever must exhibit based on the desired thrust. It is uncertain at this time how far the validity of this curve fit extends (e.g., high  $KC$  number limit). It is, nonetheless, an adequate tool when using oscillating cantilevers that have a length and width that are comparable.

## **4.0 CHARACTERIZATION OF VISCOUS DAMPING**

Before actual sidewall based enhancement studies are conducted, it is prudent to understand what effect the sidewalls will have on the oscillating cantilever operation. It is expected to have an effect on overall thrust performance, but there will also be an effect on resonant frequency and viscous damping due to a higher fluid structure interaction. Understanding these effects will allow for a more educated placement of sidewalls for thrust enhancement.

### **4.1 SIDEWALL SETUP AND PROCEDURE**

Two sidewalls, one on either side of the fan, were mounted on independent stages that traversed in the  $x$  and  $z$ -directions. These sidewalls had a width and length of 0.102 m and 0.158 m, respectively, in order to provide a sidewall area that is large enough to encompass the majority of the prominent flow field as determined in Eastman et al. [70]. The gap distance between the sidewalls and the edge of the fan blade ( $\delta$ ) and the extension distance of the tip of the fan out of the sidewalls ( $\varepsilon$ ) was varied by independently moving stages. For each sidewall, one stage was used for traversing each desired axis; therefore there were two stages per sidewall and four in total. A representation of this orientation can be seen in Figure 44.



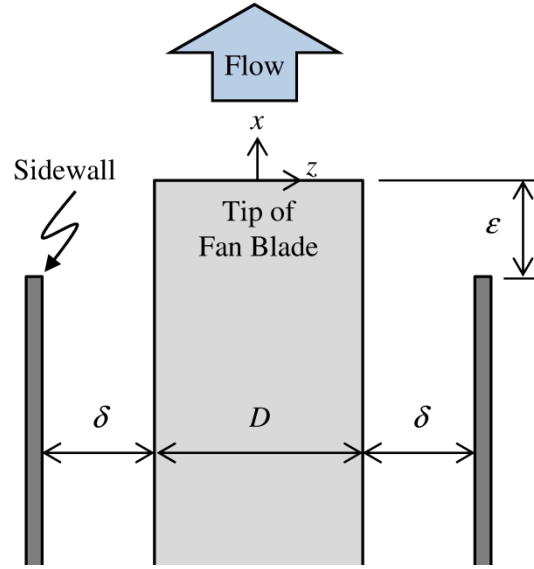


**Figure 44: Schematic illustrating orientation of the sidewalls to the fan blade.**

In order to monitor and control vibration amplitude, a laser displacement sensor (LKG-G157) was positioned above the face of the cantilever at the tip. This data, along with other pertinent data (i.e. input current, input voltage and vibration amplitude), was captured via a data acquisition unit (DAQ) from Measurement Computing (USB-1608HS). The operating frequency ( $\omega$ ) of the piezoelectric fan is the same as the natural frequency ( $\omega_n$ ), which is 61 Hz, and kept constant for all tests. As seen in previous research [56, 71], the natural frequency is dependent on the overall loading from the fluid. This changes with the presence of walls and even as the amplitude is increased or decreased. However, the resulting power change from operating at the same amplitude, but 0.5 Hz off resonance, is less than 5%.

To determine the parameters of interest, a frequency sweep is conducted at multiple voltage levels. This allows for a determination of the damping ratio, the maximum amplitude ( $A_{max}$ ) and the resonant frequency of each sweep. This was linked to other performance factors like power consumption and phase lag between the voltage and current inputs. Additionally, in

order to investigate the effect of phase lag ( $\phi$ ) and oscillation frequency on power consumption, a set of constant amplitude measurements were taken. For the constant voltage experiments, the piezoelectric element was provided with a sinusoidal RMS voltage ( $V$ ) from the function generator at three different levels: 350, 500 and 650 mV<sub>rms</sub>. After a 50x amplification, the voltage seen by the piezoelectric fan was 17.5, 25 and 32.5 V<sub>rms</sub>. The following procedure was conducted for each voltage input. When performing a constant amplitude test, the input voltage was adjusted until the average oscillation amplitude over a period of one second (~61 cycles of oscillation) was found to be within 0.005 mm of the target amplitude. Once that amplitude was met, the test was continued.

Before the sidewalls were introduced, the static displacement ( $F_o/k$ ) was determined by operating the fan at 5Hz and measuring the oscillation amplitude ( $A$ ). Additional amplitudes were independently recorded for individual driving frequencies. The remainder of the operating frequencies were varied from as large of a range as 58 to 64 Hz in 0.25 Hz increments. This range was designed as an attempt to encompass the bandwidth around the resonance frequency (as low as 70% response compared to the maximum displacement). The amplitude measurements for the frequency sweep were normalized by their corresponding static displacement at which point  $\omega_{n,air}$  and  $\zeta_{air}$  were determined from a least squares curve fit (for reference equation, please see Eq. (20) below). The sidewall gaps that were considered were 1, 2, 3, 4, 6, 8, 10, 15, 20 and 25 mm. It was determined during testing that the 25 mm gap was sufficiently far for accurately mimicking an isolated fan condition.

## 4.2 THEORY

Aerodynamic damping near resonance of a thin, flexible beam, can be quantified by first considering the response from approximating the continuous beam as a single degree of freedom system, which yields an expression for the response of the following form:

$$\frac{Ak}{F_o} = \left[ \left( 1 - \left( \frac{\omega}{\omega_n} \right)^2 \right)^2 + \left( 2\zeta \left( \frac{\omega}{\omega_n} \right) \right)^2 \right]^{-1/2} \quad (16)$$

where  $\omega$  is the operating frequency,  $\omega_n$  is the natural frequency in a vacuum,  $A$  is the oscillation amplitude,  $k$  is the cantilever spring constant,  $F_o$  is the force from the piezoelectric element on the beam and  $\zeta$  is the structural damping ratio (in the absence of any surrounding fluid). The effect of the fluid can be manifested both in terms of additional damping and extra mass in the system. Accounting for this in Eq. (16) yields the following [45]:

$$\frac{Ak}{F_o} = \left[ \left( 1 - \left( 1 + \frac{m_a}{m} \right) \left( \frac{\omega}{\omega_n} \right)^2 \right)^2 + \left( 2\zeta \left( 1 + \frac{c_a}{c} \right) \left( \frac{\omega}{\omega_n} \right) \right)^2 \right]^{-1/2} \quad (17)$$

where  $m_a$  is the added mass from the aerodynamic loading,  $m$  is the effective mass of the beam,  $c_a$  is the aerodynamic damping coefficient and  $c$  is the structural damping coefficient. The effect of the fluid becomes more significant as the ratio of aerodynamic to structural mass or aerodynamic to structural damping becomes comparable to unity. In such a case, in order to resolve the coefficients  $m_a$  and  $c_a$ , one must first determine their structural counterparts ( $m$  and  $c$ ), requiring frequency response tests to be conducted in a vacuum chamber. In the current work, the magnitude of  $m$ ,  $c$ ,  $m_a$  and  $c_a$  is not of primary concern. Here, we are more interested in the decrease or increase of damping and added mass for a bounded cantilever with respect to a

scenario where walls are far removed from the fan. In order to predict  $c_a$  from first principles, the interested reader should consult Bidkar et al. [56] and Jones [72].

In this work, we compute the total damping present during a particular frequency sweep in air. This damping ( $\zeta_{air}$ ) is a combined effect of both structural and aerodynamic damping related by the following expression:

$$\zeta_{air} = \zeta \left( 1 + \frac{c_a}{c} \right) \quad (18)$$

The natural frequency is treated in a likewise manner, namely the value found during an experiment in air ( $\omega_{n,air}$ ) can be expressed in terms of the structural and aerodynamic effects as:

$$\omega_{n,air} = \omega_n \left( 1 + \frac{m_a}{m} \right)^{-1/2} \quad (19)$$

Substituting Eqs. (18) and (19) into Eq. (17) yields the equation of motion found in Eq. (20), which is similar to Eq. (16), but the two parameters of interest are now  $\omega_{n,air}$  and  $\zeta_{air}$ , instead of their structural counterparts.

$$\frac{Ak}{F_o} = \left[ \left( 1 - \left( \frac{\omega}{\omega_{n,air}} \right)^2 \right)^2 + \left( 2\zeta_{air} \left( \frac{\omega}{\omega_{n,air}} \right) \right)^2 \right]^{-1/2} \quad (20)$$

The damping can also be expressed as the quality factor defined as:

$$Q_{air} = \frac{1}{2\zeta_{air}} \quad (21)$$

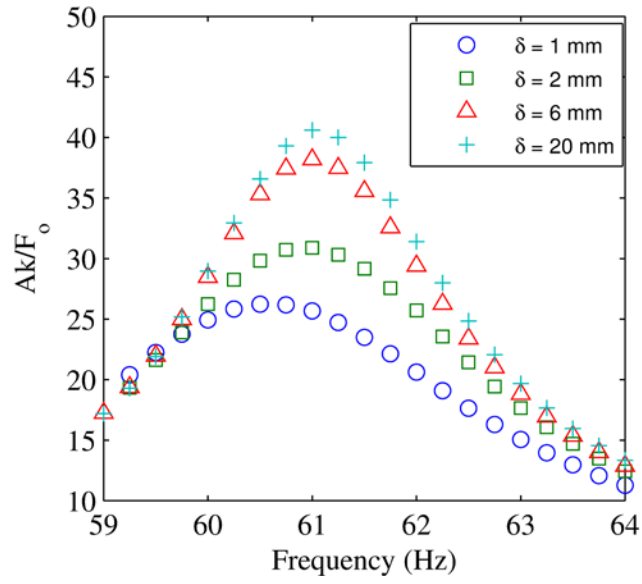
where  $Q_{air}$  is the quality factor found from an experiment performed in air and represents the combined effect of both structural and aerodynamic loading.

Additionally, as damping in fluids is a very complex mechanism, one would find it difficult to simply attribute a constant damping coefficient to fully describe it. The aerodynamic

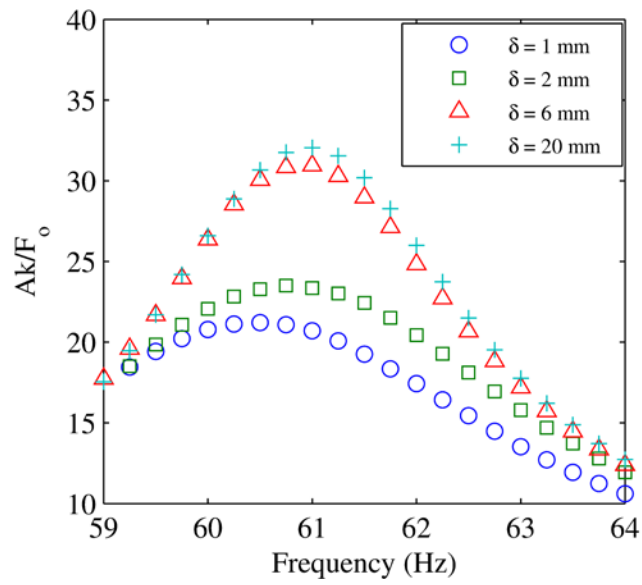
damping coefficient, in the case of this paper, is likely non-constant and based on a number of factors including the frequency, amplitude and the gap between the cantilever and the sidewall. As this is not accounted for in Eq.(20), one should think of the quality factor as more of an average assessment of how the damping will react to the changing sidewall spacing.

### 4.3 EXPERIMENTAL RESULTS

The frequency response curves for inputs of  $V = 17.5 V_{\text{rms}}$  and  $32.5 V_{\text{rms}}$  cases are shown in Figure 45 (a) and (b), respectively. For both cases, the sharpness of the resonance curve decreases as the sidewall gap ( $\delta$ ) becomes small. This is indicative of an increase in damping (or decrease in quality factor), suggesting the presence of the wall itself creates additional viscous drag, resulting in a decrease in vibration amplitude for the same input voltage. It is also apparent that for very small values of  $\delta$ , a shift in resonance frequency occurs. This is in the direction of a lower frequency rather than an increase. This trend can be better observed in Figure 46. This indicates that the effect of added mass (due to the sidewalls) only has a measurable effect when the sidewalls are in very close proximity to the fan. This is despite the fact that the effect of damping can be seen at higher gaps. It should be noted that although a difference between isolated resonance frequencies exists between different the voltage inputs, this difference is less than 0.2%.



(a)



(b)

**Figure 45: Comparison of the normalized amplitude response for the (a)  $V = 17.5$  Vrms and (b)  $V = 32.5$  Vrms case.**

Also worth noting in Figure 45 (a) and (b) is the fact that the  $V = 17.5V_{\text{rms}}$  case yields a larger normalized amplitude response for any given value of  $\delta$ . This indicates that the overall damping is also dependent on the input signal magnitude itself, where higher damping is seen for larger input magnitudes. This is attributed to fact that damping increases when larger vibration amplitudes and velocities occur, and is also consistent with conclusions found in Bidkar et al. [56], which reveals the same behavior for aerodynamic damping without sidewalls.

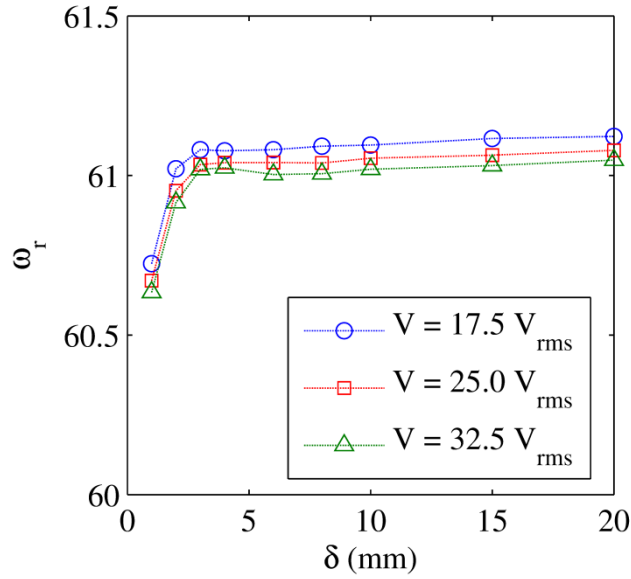


**Figure 46: The progression of the natural frequency as the sidewall gap is varied.**

The trend of the quality factor as a function of  $\delta$  can be seen in Figure 47. For an approximate gap of  $\delta = 10$  mm, the effect of the sidewalls is negligible, and no meaningful benefit or drawback is realized when the spacing increases beyond this value. The general trend is what would be expected as the reduction in gap should cause an increase of damping to the beam. For the data collected, the quality factor at  $\delta = 1$  mm is approximately 35% of the respective isolated values for  $V = 17.5$ , 25, and 32.5  $V_{\text{rms}}$ . One important tradeoff in a number of

applications is the benefit of introducing sidewalls in order to limit the loss of fluid from the side edges of the oscillating fan, balanced with the drawback of increased damping which must be overcome. The decrease in quality factor (and thus increase in damping) means that more power would be required to maintain the same vibration amplitude.

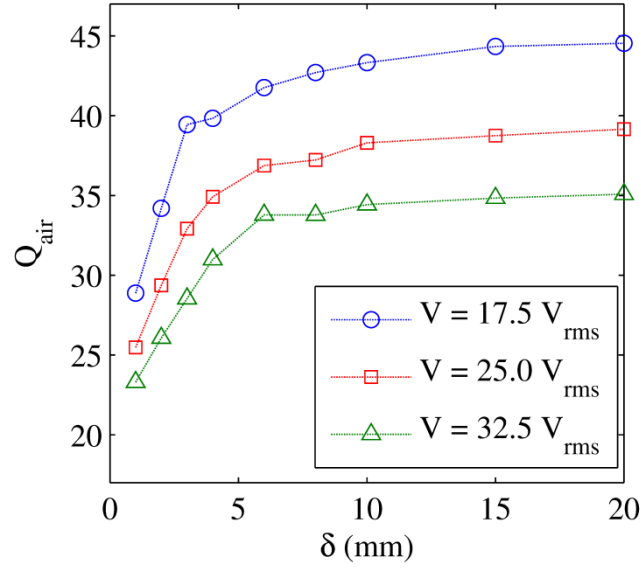


**Figure 47: The quality factor for each sidewall gap distance.**

It should also be noted that the difference in the isolated quality factor between the  $V = 17.5$  and  $25 \text{ V}_{\text{rms}}$  cases is larger than the difference between the  $V = 25$  and  $32.5 \text{ V}_{\text{rms}}$  cases. The damping plays a role in limiting the amplitude, as a slightly higher amplitude will also yield a higher oscillation velocity. As it can be gathered from an understanding of drag, as the velocity increases it causes the drag resistance to increase. This has been demonstrated in other studies using similar systems both by Kimber et al. [45] and Bidkar et al. [56]. This would reinforce that, at a minimum, the non-linear response compared to the linear voltage input is not a product of some unknown systematic error.



In order to develop a way to predict the quality factor in this type of system, a curve fit was applied to the quality factor data after being normalized by the isolated quality factor ( $Q_{iso}$ ) in each case. This resulting behavior can be captured with the following exponential relationship:

$$\frac{Q}{Q_{iso}} = 1 - C_1 e^{-C_2 \left( \frac{\delta}{D} \right)} \quad (22)$$

A least squares curve fit of the data yields 0.51 and 4.78 for  $C_1$  and  $C_2$  respectively. The results of this fit can be seen in Figure 48 with a maximum absolute error of 6.1%. This result allows for an accurate prediction of the resulting quality factor based on sidewall spacing for a set voltage input.

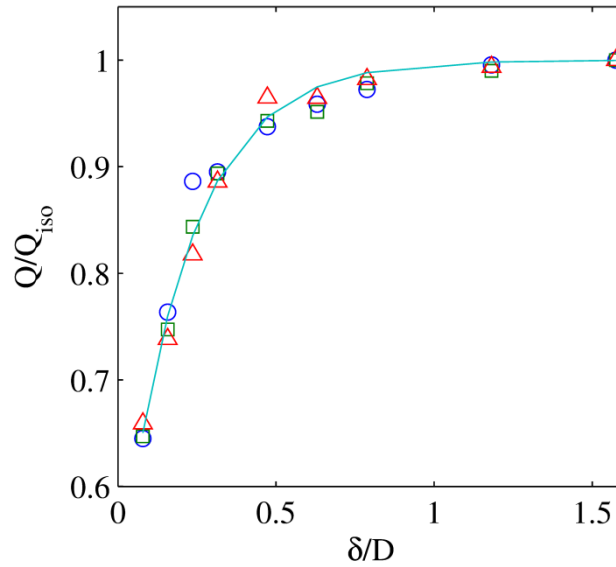


**Figure 48: Curve fit of the quality factor that has been normalized by the isolated quality factor.**

As a prevailing interest in this paper is damping and its effect on performance, it is also important to quantify the power consumption, a metric of great concern for many applications (e.g., electronics cooling). When calculating the power draw for a piezoelectric element, the power is calculated according to the following [73]:

$$P = VI \cos(\phi) \quad (23)$$

where  $I$  is the RMS current to the system and  $\phi$  is the phase difference between voltage and current input signals. The power measurements are conducted for all gaps at the three voltage inputs previously considered, but fixing the driving frequency at 61 Hz. The result is shown in Figure 49, where it can be seen that the power actually decreases for small gap distances at constant voltage inputs. Since the supply voltage remains fixed for a given set of data in Figure 49, only changes in current and/or phase difference can explain the drop in power consumption. Consequently, it becomes apparent that phase difference ( $\phi$ ) is the main contributor to the drop in power.

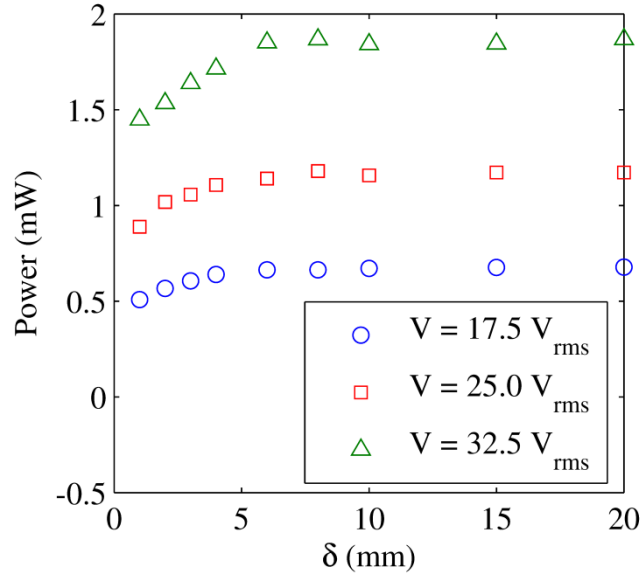


**Figure 49: The power requirement of the piezoelectric fan at 61 Hz as the gap is varied.**

The corresponding RMS current values for this data are shown in Figure 50, which reveals a trend similar to the power data, but the decrease in current is less than 2.5%, whereas the drop in power consumption can be as high as 28%, compared to their respective isolated

(large  $\delta$ ) values. Therefore, a large portion of this drop in power should be explained by a change in the phase angle.

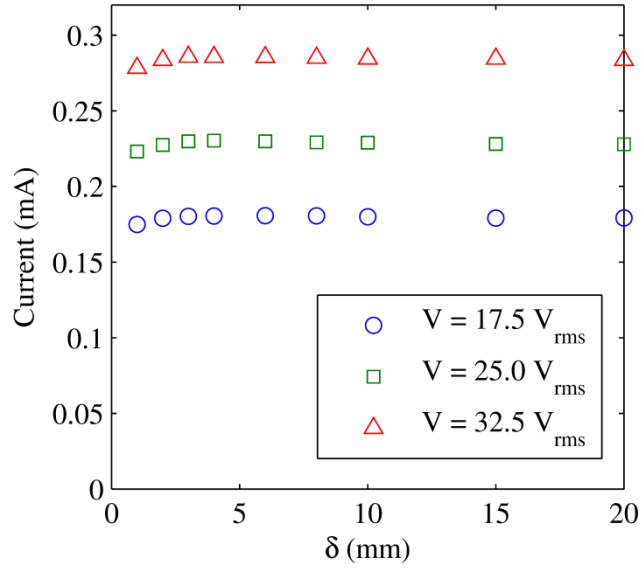


**Figure 50: The current as a function of sidewall gap for set voltage inputs.**

As seen in Figure 51, the phase lag is in the range of -1.24 to -1.35. These values are fairly close to  $\pi/2$ , which means that any small change in phase will result in a much larger change in power due to the fact that the cosine of this phase difference is the quantity of interest. Essentially, the load of the piezoelectric fan has a large imaginary component or electrical reactance. When this is taken into account, it becomes apparent that a change in phase from a gap of 1 mm to 25 mm can result in a roughly 25% change in power consumption if everything else were to remain constant.

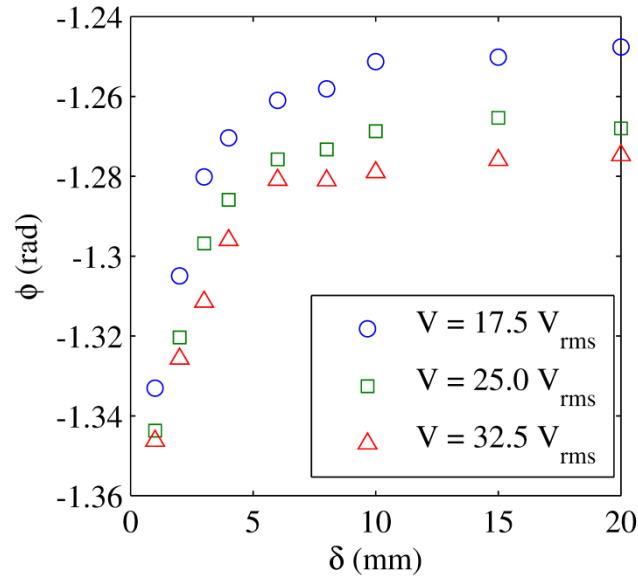


**Figure 51: The phase difference between the current and voltage input at 61 Hz for a set voltage inputs.**

In fact,  $\phi$  changes quite dramatically and does so in a very similar manner to that of the amplitude response of the cantilever, readily apparent in Figure 52, which can be directly compared to Figure 45 (a), since voltage input is the same ( $V = 17.5 \text{ V}_{\text{rms}}$ ). The peak of the phase curve changes with sidewall gap and appears to occur at the same frequency as the resonance frequencies seen from Figure 45. Although one might suppose an advantage exists since power consumption is reduced, this comes at a cost of lower vibration amplitudes due to an increase in aerodynamic damping.

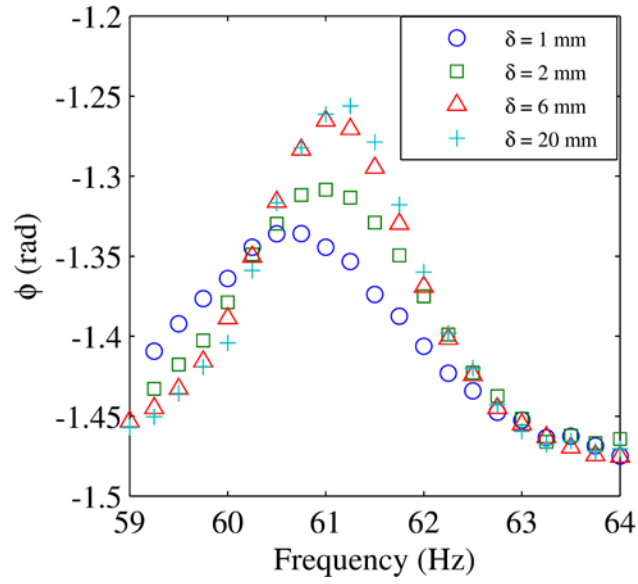


**Figure 52: The phase lag between the voltage and current input as a function of frequency for a voltage input of 17.5 Vrms.**

To illustrate this point, the amplitude measurements from each of the experiments from Figure 49 are shown in Figure 53. The trends from both of these figures reveal that both the vibration amplitude and power consumption decrease as  $\delta$  becomes smaller. In order to further evaluate the power consumption trends working both on and off resonance, additional experiments are performed at fixed amplitudes of 4, 5, and 6 mm with  $\delta = 25$  mm and varying the input frequency across the bandwidth of the frequency response.

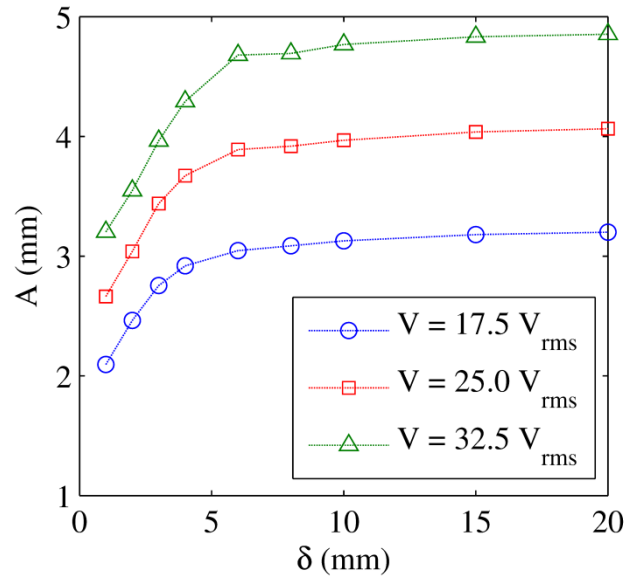


**Figure 53: The maximum oscillation amplitude for each sidewall gap distance.**

The result is shown in Figure 54, where it is apparent that the change in phase lag ( $\phi$ ) when operating off resonance cannot adequately make up for the increased power input required to keep the amplitude consistent across the frequency spectrum. For the 4 mm amplitude, the curve is flatter indicating that the phase does have some effect. However, in order to see a potentially flat power curve, the amplitude would need to be so small that there would be no practical use in this setting. Regardless, this finding demonstrates that operating at resonance is, as one would intuitively expect, the best option in terms of minimizing the power requirements. Further experiments should be conducted where the application-specific performance metrics (e.g., thrust or thermal convection) are evaluated along with the input to truly gauge the tradeoff that must be made between the benefits from sidewalls in terms of preventing flow being lost across the side edges compared to the loss of performance due to a decrease in amplitude and/or the increase in power consumption in order to maintain a specific amplitude.

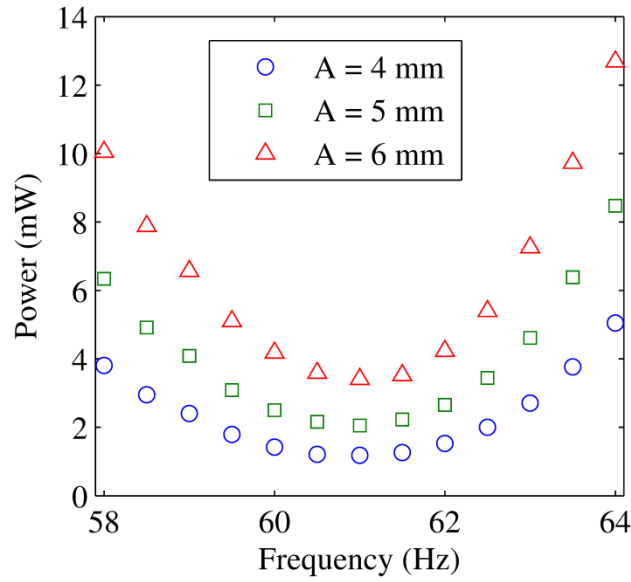


**Figure 54: The power requirement to the piezoelectric fan with a fixed amplitude as the frequency is changed within the bandwidth.**

#### 4.4 CONCLUSION

While introducing sidewalls, it is prudent to look at the damping effect that they will present. Thus, frequency response curves were experimentally measured for a piezoelectric fan vibrating near two sidewalls in order to quantify the effect of enclosure walls on the oscillation characteristics of the fan. Three voltage inputs were considered at multiple sidewall gaps. The natural frequency was shown to decrease with proximity to the side wall suggesting an increase in the added mass from the surrounding fluid. For the damping characteristics, as the proximity of the sidewalls to the fan is decreased, the quality factor was found to also decrease. This means that as one seeks to improve the flow shaping by introducing sidewalls, the inevitable damping must be addressed as it becomes more and more of a factor. A curve fit was applied to the quality

factor, showing good agreement with experimental data. This gives a basis for predicting the viscous damping as a function of the sidewall gap, and suggests a more comprehensive study would be worthwhile where additional factors are investigated (e.g, beam width, length, operating frequency, etc.). The effect of the sidewalls on damping was in general much larger than their impact on the resonance frequency. In addition, the damping began to change from its isolated value at a much larger gap compared to the gap where the resonance frequency began to shift.

It has been demonstrated in this paper that, for a constant voltage input, the change in power requirement is primarily a result of the phase difference between the voltage and current input. This change in the phase difference is driven entirely by the damping conditions imposed by the sidewalls or frequency shift from resonance. However, it does not have a pronounced enough effect to meaningfully limit the power increase needed in order to maintain a specific amplitude.

These findings provide the basis for understanding and predicting the effect of sidewalls on damping and impact on power consumption. This allows for evaluation of the operational characteristics and limitations for an oscillating cantilever when introduced into an enclosed space. Fundamentally, higher damping limits the amplitude for a specific voltage input.



## **5.0     SIDEWALL POSITIONING FOR THRUST ENHANCEMENT**

Now that a very firm foundation of knowledge has been set, positioning of the sidewalls for thrust enhancement can be conducted with confidence. The previous research up to this point allows an understanding of what to expect when introducing sidewalls. Further, many of the key findings in the previous sections are shown to play a role in thrust performance.

### **5.1     SIDEWALL THRUST MEASUREMENT PROCEDURE**

Since the experimental approach in this study is to quantify the performance (both thrust and power consumption) in terms of a given vibration amplitude, the sinusoidal voltage ( $V$ ) from the function generator was adjusted while monitoring the oscillation amplitude. The amplitude was quantified by taking an average measurement over a period of one second (~61 oscillation cycles). The data acquisition rate was 5000 Hz. Once the average amplitude of the 61 cycles reached within 0.005 mm of the target amplitude, the experimental test was initiated. Due to the influence of the sidewalls from viscous damping and air effects, the input voltage changed for different sidewall locations in order to maintain a constant amplitude. Due to findings from previous research [71], where the lowest power consumption was observed at resonance, the oscillation frequency in the current work was set to the unbounded natural frequency of the fan used, namely 61 Hz.

Prior to collecting data, the scale was turned on and allowed the 30 minute warm up time suggested in the documentation. The scale was then observed to make sure that the readings were stable (i.e., fluctuations were minimal and less than 0.5 mg). As the scale is very sensitive and the changes in thrust force can be very small, the entire system was enclosed within a 0.6 by 0.6 by 1.2 m plastic box with one 0.6 by 1.2 m side comprised of a movable curtain. This was to limit any errant air flows present in the room that could disrupt the scale measurements. Introduction of other objects into the enclosure (i.e., arms and hands) were expected to have a disruptive impact on the fluid flow, necessitating a check for stability before each new test. It should also be noted that when switching between two different operational states (e.g., zero to a nominal thrust value, or low thrust to high thrust experiment), there is inherently a period of instability in the scale where that data is unreliable. Therefore, once a specified vibration amplitude was reached, the signal input to the fan remained unaltered for a period of roughly 2 minutes, at which point, the thrust data acquisition procedure was initiated. Data was then collected for a period of approximately 60 seconds at a nominal sample rate of 5 Hz. After approximately 50 seconds of data capture, the signal to the fan was shut off in order to quantify the “zero thrust” reading for each test. Only the last 5 seconds of this no thrust condition were used for this purpose, which also served the purpose of monitoring any drift present in the reading throughout the experiments, and proved to be negligible. The actual thrust measurement reported in this work is the average value from the first 30 seconds worth of data (150 data points). We intentionally removed the thrust data collected between the 30 and 55 second time marks to ensure that the fluctuations present during the transition to zero thrust did not affect the data in any way.

As the location of the sidewalls, in relation to the piezoelectric fan, were of primary importance to this paper, both sidewall gap ( $\delta$ ) and tip extension ( $\varepsilon$ ) were varied. First, the sidewall gap was considered independent of the extension. The values tested were chosen for the sake of consistency with previous research into the viscous damping effects [71], namely  $\delta = 1, 2, 3, 4, 6, 8, 10$ , and  $15$  mm. For this first set of experiments, the tip extension was approximately  $25$  mm inside the sidewalls ( $\varepsilon = -25$  mm). The second set of experiments focused on the effect of tip extension, and only a subset of the sidewall gaps were considered, namely  $\delta = 1, 2$  and  $3$  mm. It was desired that a reasonable progression from a fully enclosed condition to a sufficiently large tip extended be observed, therefore tip extensions in the range of  $-10 \leq \varepsilon \leq 15$  mm (a total of 14 points) were considered. This gave a good representation of the progression of the thrust and power requirements that resulted as the tip extension was varied.

In experimental work, uncertainty in measurements is always a concern. To quantify the overall uncertainty, two tests consisting of five runs each were conducted: 1) where the test was repeated with zero change in the setup to quantify the repeatability error and 2) where the sidewalls were moved and repositioned to give the worst case scenario of human error. For the uncertainty quantification,  $A = 5$  mm,  $\delta = 1$  mm, the driving frequency was  $61$  Hz and  $\varepsilon = 0$ . Uncertainty was found using a simple t-test for both power and thrust. The power uncertainty was  $0.038$  mW and  $0.21$  mW for the first and second tests respectively. The thrust uncertainty was  $0.0028$  mN and  $0.0047$  mN for the first and second tests respectively. Taking the square root of the sum of the squares for these two tests yields an overall uncertainty of  $0.0055$  mN and  $0.22$  mW for thrust and power respectively. Note that these values should be considered the absolute worst case scenario, since they include the error present from repositioning the sidewalls, something that was avoided during the majority of the tests. However, even when adopting this

overly conservative uncertainty, this represents an error that ranges between 2.9% and 5.1% for the thrust and 3.1% and 6.1% for the power when considering the experimental data from all tests.

## **5.2 THRUST ENHANCEMENT WITH SIDEWALLS**

### **5.2.1 Sidewall Gap Spacing**

Thrust data is shown in Figure 55, which reveals that, when fixing the amplitude, there is virtually no thrust enhancement due to the sidewalls until they are very close to the fan blade ( $\delta < 2$  mm). This essentially means that the sidewalls are not actually helping to direct the flow until they are right next to the fan. It is interesting to compare this finding to a previous study focused on the aerodynamic loading from the sidewalls [71], where the natural frequency was found to be insensitive to the sidewall gap for  $\delta > 3$  mm. This change in resonance frequency is due to the added mass from the air. It stands to reason that if the increase in added mass is not present for a given configuration, then additional flow, manifested by an increase in thrust, would also be limited.

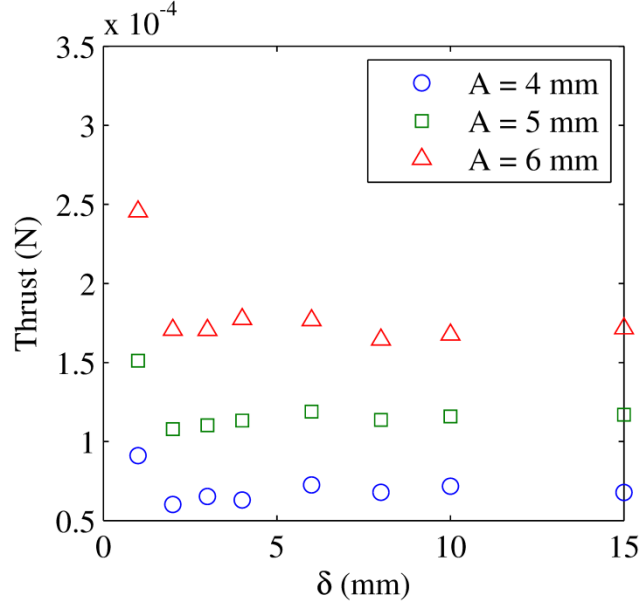


**Figure 55: Thrust force as a function of the gap distance for three fixed amplitudes.**

Armed only with the information from Figure 55, one may assume that the influence of the wall is only felt for very small values of  $\delta$ . However, the full picture of the impact can only be seen once the power consumption is also quantified. This data is shown in Figure 56, where the power is determined from the following expression [73]:

$$P = IV \cos(\phi) \quad (24)$$

where  $I$  is the rms input current and  $\phi$  is the phase difference between the voltage and current input signals. Note that the trends in power consumption show this quantity begins to feel the effect of the sidewalls from farther away (near  $\delta \sim 5$  mm), when compared to the data shown in Figure 55. It is interesting to note that just as the thrust data from Figure 55 could be explained through analyzing the added mass effect, the power consumption data from Figure 56 reveal trends that mimic the added damping effect [71]. From Figure 55 and Figure 56, one quickly realizes there is a range of gap distances ( $2 \text{ mm} < \delta < 5 \text{ mm}$ ) where no thrust enhancement is

seen, and yet more power is required due to the increase in viscous damping. This would recommend the decision process for location of boundaries to essentially take one of two routes. The sidewalls could be located as close as possible to take advantage of the flow enhancement, or the sidewalls should be removed altogether.

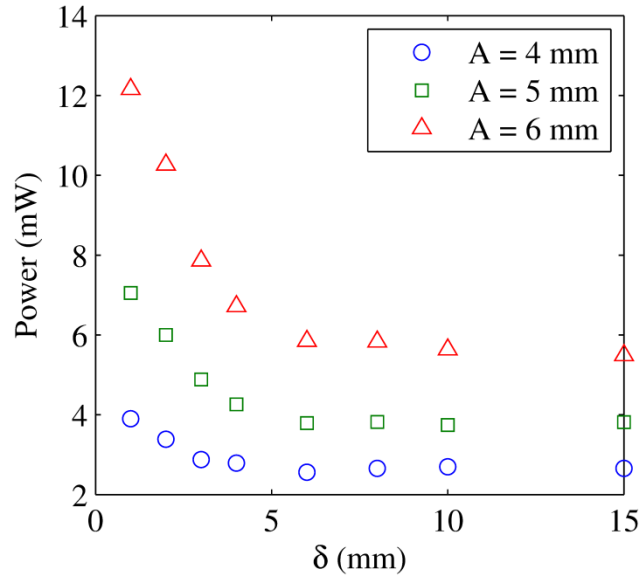


**Figure 56: Power as a function of gap distance for three fixed amplitudes.**

It is important to quantify the performance (enhanced thrust) in light of drawbacks (increase in power requirements). Here, we define the efficiency ( $\eta$ ) as the ratio of thrust to power according to the following expression:

$$\eta = \frac{TD\omega}{P} \quad (25)$$

Note that  $\omega$  and  $D$  (both constants in this study) have been included in the numerator of Eq. (25) in order to express  $\eta$  in dimensionless form. The result of this analysis is shown in Figure 57. This figure demonstrates that, even though there is a thrust enhancement, the amount of extra power consumption increases by a higher percentage than the thrust. Thus, it is less efficient on a

thrust per watt basis to have sidewalls at all. This would indicate that any sidewalls near a piezoelectric fan in a power sensitive cooling system are detrimental. However, it should be noted that the piezoelectric fan is fully covered by the sidewalls. The tip is approximately 25 mm from the closest edge ( $\varepsilon = -25$  mm). Therefore, the next step in this analysis was to investigate the effect of the tip extension in an effort to more comprehensively determine whether sidewalls can yield any extra benefit.

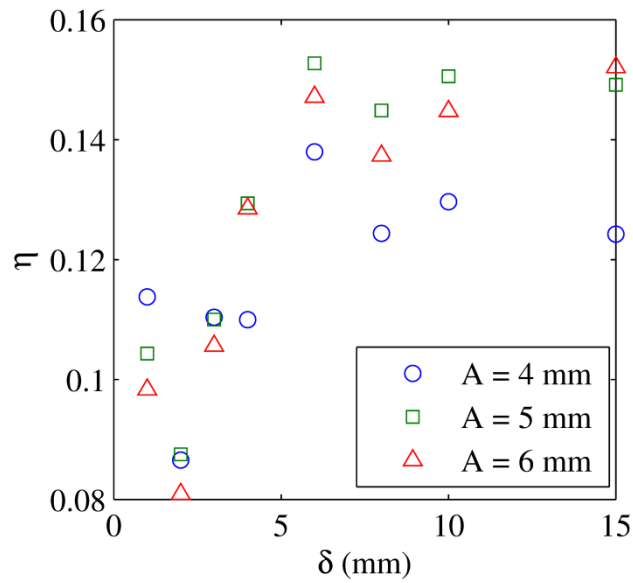


**Figure 57: Efficiency of thrust as a function of gap distance for three fixed amplitudes.**

### 5.2.2 Tip Extension Distance

In order to obtain information on the effect of tip extension, additional experiments were conducted at the three smallest gap distances ( $\delta = 1, 2$  and  $3$  mm). For these specific tests, values of  $\varepsilon$  ranging from  $-10$  mm to  $+15$  mm were considered, with only a single amplitude ( $A = 5$  mm). The thrust measurements from these experiments are shown in Figure 58 and reveal higher levels

of thrust as the gap becomes smaller (similar to the conclusion reached from Figure 55). Although some enhancement exists from the  $\delta = 3$  mm case to the  $\delta = 2$  mm case, the enhancement is much larger for the  $\delta = 1$  mm data, where the highest thrust occurs across the entire tip extension range considered. It is expected that the three curves will eventually converge at a sufficiently large tip extension. In fact, they should converge to the dashed line shown in Figure 58, which represents thrust from an unbounded cantilever. To validate this expectation, additional measurements would need to be collected for  $\varepsilon > 15$  mm. Although the current experimental setup prevented this from being achieved, the range was chosen in order to target values relevant to realistic applications, and based on the data, captures the important thrust enhancement trends which are the focus of this work. For the  $\delta = 1$  mm case, the performance is maximized near  $\varepsilon = 0$ , and represents a 61% improvement over the unbounded cantilever case. The  $\delta = 2$  mm case yields an optimum at roughly  $\varepsilon = 10$  to 12 mm and remains within 10% of the unbounded flow for  $\varepsilon < -4$  mm. The trend in the  $\delta = 2$  mm thrust case may indicate that there is some thrust enhancement from the sidewalls that was not observed from the fully enclosed case. This is indicated by the fact that from  $\varepsilon = 0$  to 12 mm the thrust remains roughly 15% higher than the unbounded case. Although it was found in Figure 55 that the  $\delta = 2$  mm gap did not display a noticeable increase, it is possible that the effect was inhibited from the boundary effect of the downstream section of sidewall. The  $\delta = 3$  mm data reveals thrust values within 9% of the unbounded flow, suggesting that, by this gap distance, there is only a negligible enhancement available from the sidewalls.



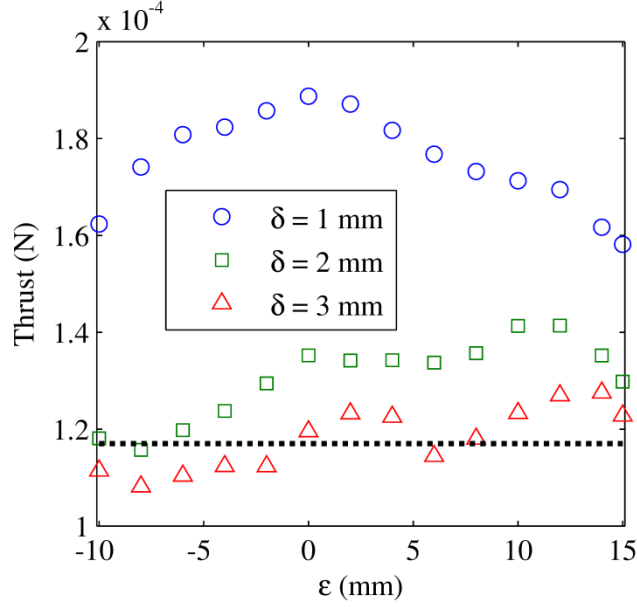


**Figure 58: Thrust as a function of tip extension for a fixed amplitude of  $A = 5$  mm. The horizontal line indicates the thrust generated in the absence of sidewalls.**

Regarding the maximized performance seen for  $\delta = 1$  mm and  $\varepsilon = 0$  in Figure 58, it is interesting to note previous efforts to quantify the pressure and flow rate capabilities of oscillating cantilevers [42] included testing near these conditions ( $\delta \approx 1.15$  mm and  $\varepsilon \approx 0$ ), and saw the pressure maximized in this case. It is clear from the  $\delta = 1$  mm data in Figure 58 that the performance begins to decrease beyond the  $\varepsilon = 0$  point. This is primarily due to the fact that flow begins to be lost laterally off of the side edges of the fan.

The performance at a tip extension value of  $\varepsilon = 0$  becomes more interesting when considering the power consumption data shown in Figure 59. Although data for  $\varepsilon < 0$  follows the trend one would naturally expect, a drop in power is observed for  $\delta = 1$  mm once  $\varepsilon \geq 0$ . In fact, the power consumption in this  $\varepsilon$  range is nearly identical for the  $\delta = 1$  mm and 2 mm cases. Although this is exactly expected for extremely large  $\varepsilon$  ( $\delta$  becomes insignificant as  $\varepsilon \rightarrow \infty$  and

can be observed for  $\varepsilon > 10$  mm), the fact that this occurs for relative small  $\varepsilon$  indicates that through decreasing the sidewall distance, extra thrust is available without increasing the power consumption. There also appears to be a steeper drop for  $\delta = 1$  mm and 2 mm from  $\varepsilon = 6$  to 10 mm than from  $\varepsilon = 0$  to 4 mm.

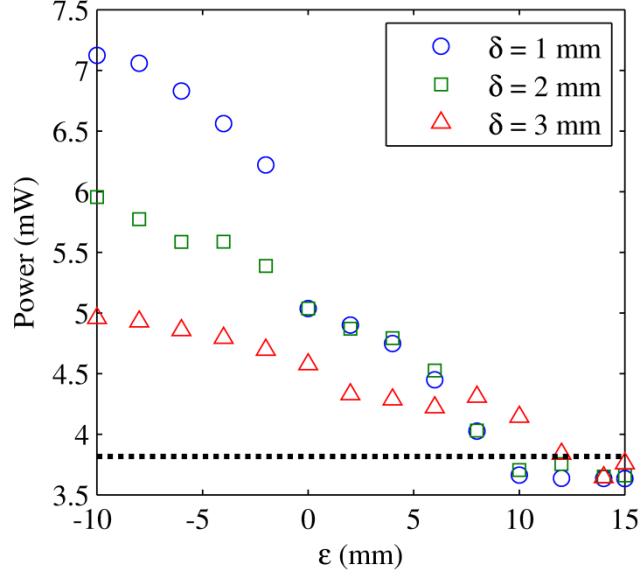


**Figure 59: Power as a function of tip extension for a fixed amplitude of  $A = 5$  mm. The horizontal dashed line represents the power consumption at a no sidewall effect condition.**

One would be remiss to not wonder what is causing such a drastic change in power consumption. According to Eq. (24), three variables could explain the power consumption data, namely the voltage and current inputs, and the phase difference between these two signals. When observing the voltage and current draw from the piezoelectric fan in Figure 60 and Figure 61, respectively, it can be seen that these both exhibit the same trend. Both the voltage and current for the  $\delta = 1$  mm case are greater than the  $\delta = 2$  mm case. As we look specifically at the  $\varepsilon = 0$  data point, the input voltage is  $74.7 V_{\text{rms}}$  and  $70.3 V_{\text{rms}}$  and the current draw is  $0.348 \text{ mA}_{\text{rms}}$  and  $0.340 \text{ mA}_{\text{rms}}$  for  $\delta = 1$  mm and  $\delta = 2$  mm, respectively. The voltage-current product (without

accounting for the phase difference) then becomes 26.0 and 23.9 mW for  $\delta = 1$  mm and  $\delta = 2$  mm, respectively. Thus, there is another factor that causes the drop in power for the smaller gap.

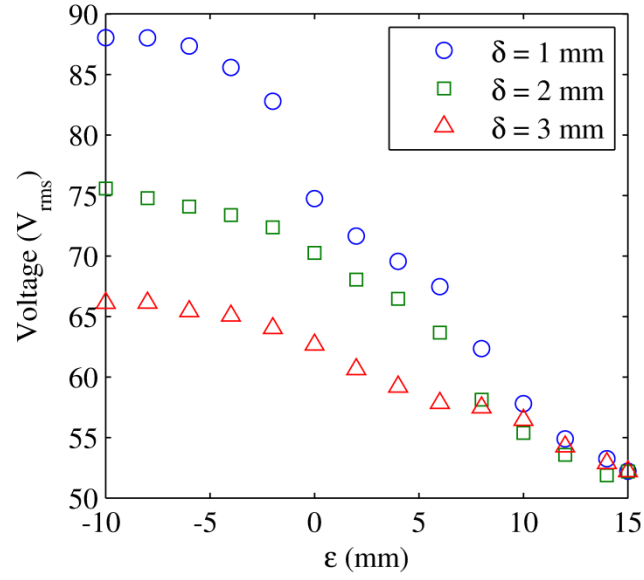


**Figure 60: Voltage as a function of tip extension for a fixed amplitude of  $A = 5$  mm.**

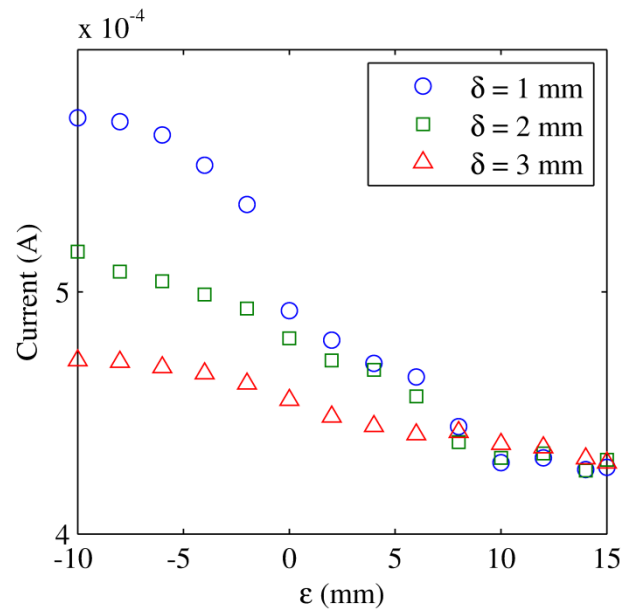


**Figure 61: Current as a function of tip extension for a fixed amplitude of  $A = 5$  mm.**

The phase difference is the last component of the power consumption to investigate, and can be found in Figure 62. Although for a given value of  $\delta$ , the phase difference does vary slightly across the  $\varepsilon$  range shown, the trends are all very similar for all three data sets, just simply offset from one another by some small amount. As the gap decreases, the phase decreases in magnitude which causes the cosine part of the oscillating signal power equation to decrease. This is the primary reason why the power for both gap distances ( $\delta = 1$  and 2 mm) are the same for positive extension values. As expected, when  $\varepsilon$  becomes very large, the three curves begin to converge to the same value.

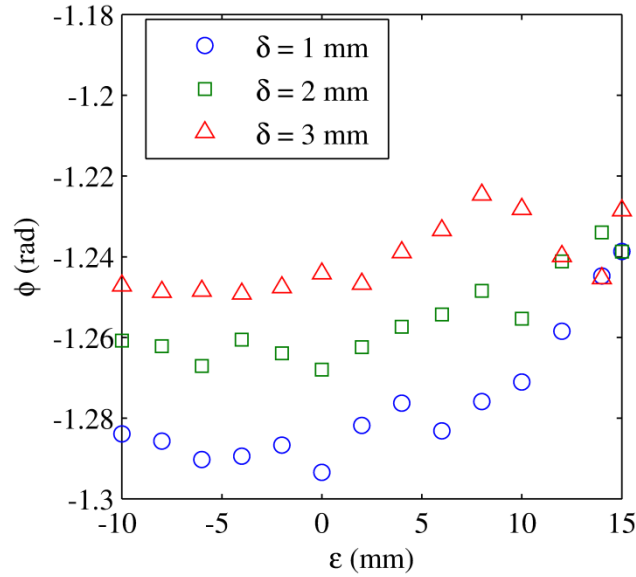


**Figure 62: Phase as a function of tip extension for a fixed amplitude of  $A = 5$  mm.**

Although the preceding analysis provides a quantitative look at the nearly identical power consumption for  $\delta = 1$  and 2 mm when  $\varepsilon = 0$ , it is also interesting to note the abrupt drop in power consumption shown in Figure 61 between  $\varepsilon = -1$  mm and 0, a phenomenon only observed for the  $\delta = 1$  mm data. In terms of the flow physics that influence the power consumption trends,

one could think of the fan as a pump with air as the working fluid. In Kimber et al. [42], the primary goal was to develop pump curves (pressure vs. flow rate) for piezoelectric fans, similar to well-accepted characterization tools used for more traditional fans and pumps. When one introduces boundaries (i.e. sidewalls, channels, etc.), it creates an additional pressure drop, since the fan must now push the flow through this path. As the flow near the fan tip becomes unrestricted, the frictional flow losses would decrease and require less of an increase in voltage (and consequently current) to maintain a specific amplitude. To verify the connection between the effective pump curve of the piezoelectric fan and the available thrust and power requirements, further tests should be conducted.

Taking all of this into account, it is then no surprise that, when considering the thrust efficiency ( $\eta$ ), shown in Figure 63, the  $\delta = 1$  mm case becomes the clear choice. The extra thrust delivered more than makes up for the increase in power that might be needed to maintain an amplitude of  $A = 5$  mm. This is the case even for  $\varepsilon < 0$ , however there is a substantial jump at  $\varepsilon = 0$ , where the true benefits of the sidewall begin to be realized. As observed in Figure 59, the second jump from  $e = 6$  mm  $\leq \varepsilon \leq 10$  mm is even more apparent. Although more analysis is required to determine a conclusive reason for these jumps, it is possible that the first is the result of allowing the flow entrainment seen in our flow field analysis. The second jump could be the possible result of a transition in the resulting  $x$ -directional flow. The maximum efficiency can be observed for  $\varepsilon = 10$  mm before the efficiency begins to decline. For  $-8$  mm  $\leq \varepsilon \leq 15$  mm, a substantial benefit exists for the  $\delta = 1$  mm case, when compared to either the  $\delta = 2$  or 3 mm data. Additional fan geometries and materials should be tested, along with further variations of  $\delta$ , since such a drastic change is observed between  $\delta = 1$  and 2 mm. This would enable a more

comprehensive understanding of the metrics of interest in terms of all applicable design variables (frequency, width, length, etc.).

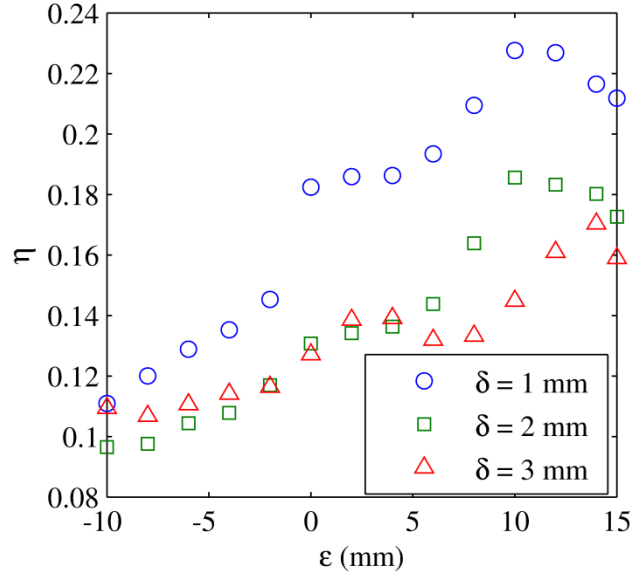


**Figure 63: Efficiency of thrust as a function of tip extension for a fixed amplitude of  $A = 5$  mm.**

### 5.3 CONCLUSION

After all of the fundamental analysis was conducted to understand the nature of the performance and baseline values present in an oscillating cantilever, thrust enhancement could be undertaken in a thoughtful and targeted manner. Thrust and power data was collected for oscillating cantilevers operating at resonance near sidewalls. Those sidewalls were varied in both gap distance between the walls and the fan edges ( $\delta$ ) and in the location of the oscillating tip to the downstream edge of the sidewalls ( $\epsilon$ ). It was found that the location of the sidewalls in relation to the edge and tip of the cantilever can play a significant role in performance.

When isolating the effect of sidewall gap, it was found that the spacing has very limited effect on the thrust for  $\delta > \sim 2$  mm. The indication this provides is that there is negligible added mass to the system unless the sidewalls are very close to the oscillating cantilever. This added mass to the system is likely the cause of the added thrust. However, when keeping the amplitude fixed, additional power must be supplied and tends to outweigh the benefit of extra thrust, at least from an efficiency standpoint (thrust per watt).

The location of the oscillating tip in relation to the sidewall edge proved to be extremely important. Once the tip reaches and extends past the edge of the sidewall, the power consumption difference between a gap of 1 and 2 mm is reduced to zero. This is after a sharp drop in power consumption as  $\varepsilon$  approached 0. This finding demonstrates that there is an orientation where thrust can be substantially enhanced with essentially no increase in power requirements. The likely cause is potentially linked to the detrimental impact of the sidewalls themselves on the downstream flow produced by the oscillating cantilever. Further studies should be conducted to clarify the physics that explain this phenomenon.

These findings now provide a basis for understanding design approaches for an enclosure surrounding an oscillating cantilever. In the future, more research should be conducted, including the pressure and flow rate performance, in order to fully understand the effects of walls on all metrics of interest.

## 6.0 FINAL REMARKS

Multiple piezoelectrically oscillating cantilevers have been analyzed in various situations. Although the driving mechanism was a piezoelectric for our studies, the resulting outcome from the overall motion of the cantilever can reasonably be attributed to other oscillation mechanisms. The flow field was inspected for a cantilever with no observable boundaries in both the  $x$ - $y$  and  $y$ - $z$  planes. The inlet regions were found to be upstream and above and below the face of the fan. It was also found that there was a flow towards the fan from the sides near the tip. Our observations also found that the location of maximum flow off the tip of the fan came at the midpoints between the center of the fan and the edges. This yielded an understanding of the locations of inward and outward flow, which provided clues to proper boundary placement.

The resulting thrust was then measured for multiple piezofans to develop an understanding of the factors that contribute to its effectiveness. The study found that one can accurately predict the resulting thrust force with the oscillation amplitude, frequency and cantilever width. This acted as a baseline from which to compare a sidewall bounded flow.

Sidewalls were then introduced to help in determining an understanding of the viscous damping, power consumption and thrust force resulting from the proximity and location of the boundaries. The damping was found to inevitably increase as the gap distance decreased. The resonant frequency, however, did not change until the gap spacing was very small. It was discovered that the effect of thrust enhancement does not occur until the sidewalls are very close



to the cantilever. The power consumption did as well, but would start to increase at a larger gap distance. However, the power consumption would decrease when the oscillating tip was close to the edge of the sidewalls. Additionally, at the cantilever position where the tip was in line with the sidewall edge or extended from it, the power requirement for the smallest gap spacing decreased by a large amount that caused it to be of the same magnitude as the larger gap spacing. This meant that one could essentially maintain a higher thrust for the same power requirement as was found with the larger gap spacing.

## **6.1 FUTURE WORK**

There is a large amount of potential future work that can be deduced from the findings in this work. Further analysis can go into looking into the flow field with a fully three dimensional flow field analysis. This would require new equipment that could render velocity vectors in an entire volume of fluid. Only a single sidewall shape was tested in this work. It was postulated that there may be a more effective sidewall shape based on the inlet and outlet flow areas off the side of the cantilever. This is even more apparent when we consider that the relation of the cantilever tip to a sidewall edge had such a dramatic effect on power consumption.

There is also possibility to study the effect of multiple fan interactions on the flow field and thrust. This is in the same vein of sidewalls as there is the possibility that fan interaction could either help or hurt propulsion capabilities. As there are multiple possible orientations (edge to edge, face to face and combinations thereof), the possibilities are numerous.

As the focus of much of this work was geared mostly to propulsion, the application of another fluid to see its effects would be prudent. One of the possible applications is aquatic

propulsion, so working towards the introduction of water would be a logical step. This would require new thrust tests and could ultimately lead to a potential prototype.

## **APPENDIX A**

### **PARTICLE IMAGE VELOCIMETRY (PIV) SYSTEM INTRICACIES**

A particle image velocimetry (PIV) system is a very useful system that allows virtually undisturbed monitoring of flow fields. The system takes a pair of images of the flow that are illuminated by a laser sheet. The transparent fluid is seeded with small, preferably neutrally buoyant, particles that are illuminated by the laser sheet. The two images, being taken a set amount of time apart, are statistically compared by subdividing the image into smaller subwindows (e.g., 16 x 16 pixels). Marching across the image with this subwindow analysis yields an average magnitude and velocity direction for each location analyzed. Product documentation can provide a much more in depth walkthrough of the process, including the statistical analysis algorithms. The purpose of this section is to provide a guide to the nuances that will hopefully allow for the most accurate replication of the findings found in this work. The default capture settings can be found in Table 4.

**Table 4: List of the default PIV image capture settings.**

Setting	Value
PIV Frame Mode	Straddle
Pulse Rep Rate	14.5 Hz
Laser Pulse Delay	400 $\mu$ s
Delta T	16 $\mu$ s
PIV Exposure	405 $\mu$ s

### **A.1 ORIENTATION AND CALIBRATION**

In a simple, one camera setup, the most optimal orientation is where the camera is positioned perpendicular to the laser sheet. A non-perpendicular orientation can be used if required by the nature of the system that is studied, but the calibration process becomes more complicated. Regardless of the orientation, it is recommended that a calibration plate be used in order to properly quantify the mm to pixel ratio. Post collection calibration can be accomplished, but it is difficult and more time consuming than doing it beforehand.

Keeping a good focus with the camera lens is also important to the overall outcome of the data. As one is focusing on a thin laser sheet, a small movement in focus can greatly reduce overall visibility of the seeding particles. This is also a time to check for proper orientation, as all sections will either be in or out of focus at one time if placed correctly. The recommended focusing procedure is to first focus on the object that is generating the fluid motion if applicable (in our case it is the fan blade). Once that has been set, the seeding particles should be

illuminated by the laser sheet which will allow for the fine tuning of the lens focus. The first step can be omitted, but it will help the user start out close to the correct focus.

## **A.2 SEEDING PARTICLES**

Proper application of seeding particles is the most integral part of an accurate velocity field. As stated previously, the seeding particles should be as close to neutrally buoyant as possible to avoid the problem of settling or layering of the seeding particle density. The two methods that have been employed during this research are glycerin fog and smoke particles. Both of these seeding particles produce comparable results with the flow field. The fog was used first and had some very problematic drawbacks. First, seeding density was very difficult to control and often necessitated waiting long periods of time for some of the particles to dissipate or combine with each other. When the particles combine, it can create variations in particle size which could be a problem in certain circumstances. The second problem is that glycerin is sticky and does not dry out adequately between tests. This means that components would be covered in a layer of glycerin and would have to be cleaned off. The second type of seeding particle that was used (smoke) did away with much of the problems found with the glycerin. The delivery system was much smaller so that particle density was much easier to control. Additionally, the smoke is inherently dry which means that cleaning can be adequately accomplished with compressed air if need be.

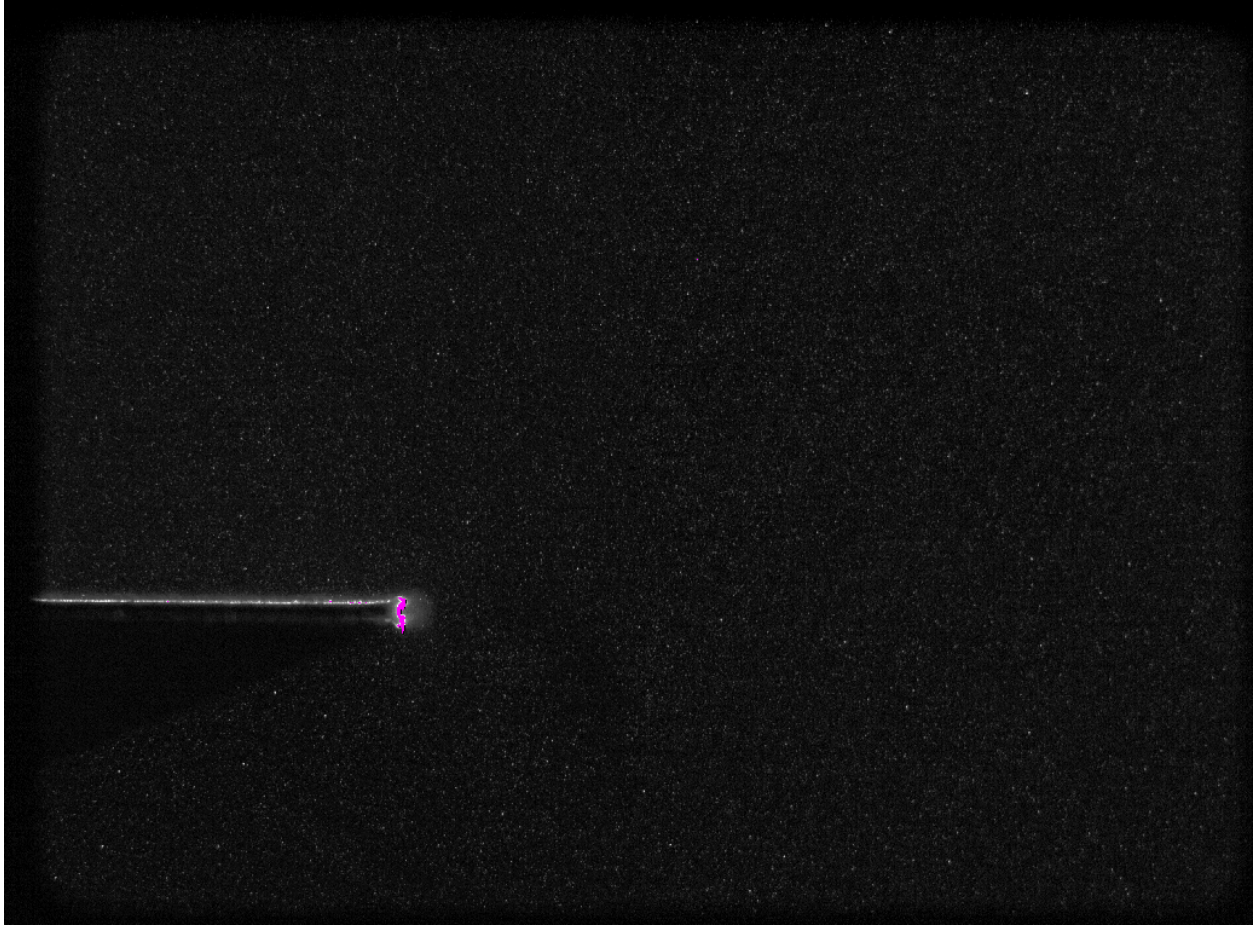


**Figure 64: An image of a proper seeding particle density obtained with a smoke pen.**

An example of proper seeding can be seen in Figure 64. For the best velocity field outcome, the seeding particles should be large enough to show up on the screen, but no larger than a few pixels. The number of pixels that a particle can reside in is somewhat related to the size of the grid, or subwindow used. Typically, it would not be recommended that grid size be reduced to less than 16 by 16 pixels as each grid should be able to contain more than one or two particles. The timing between the two images should be such that the movement is only a few pixels. A good way to determine a proper timing is that one should be able to observe the movement by eye when switching between the two images. For reference, the timing of the laser pulses in this research is 16  $\mu$ s.

It is recommended that there be some sort of check to ensure that the seeding is adequate. The method used during the testing for this paper is simply to process a single set of images using default settings (it should be noted here that, other than the actual grid size, all other settings are essentially kept as default). A processed set of images yields a single velocity field and an example can be seen in Figure 65. Note that the direction and length of the green arrows indicate the velocity vector. Red vectors did not meet the cutoff criterion, and should be carefully scrutinized. Locations where these vectors are likely to show up and also be disregarded include those areas not illuminated by the laser sheet (e.g., under the fan in Figure 65) and the edges of the image. Even if these locations show a vector that looks reasonable in terms of its magnitude and direction, it is still good practice to disregard them.



**Figure 65: Image of a good velocity vector field resulting from a satisfactory density of seeding particles.**



## APPENDIX B

### UNCERTAINTY CALCUATIONS

#### B.1 GENERAL PROCESS

Quantifying the uncertainty in a set of data allows one to inform the reader of the confidence interval they can assign to the numbers. It also provides an indication of the impact associated with individual uncertainties from different sensors. The following is a generalized walkthrough of how all the uncertainty for the data collected in this research was determined.

In a normal distribution of data, the collection of multiple points of data should fall about a mean with an occurrence that follows a Gaussian curve. Estimating the repeatability uncertainty is done by making use of the student's t-test as seen in the following equation:

$$u = \frac{t_{\nu,C} S}{\sqrt{N}} \quad (26)$$

where  $u$  is the uncertainty,  $S$  is the standard deviation,  $N$  is the number of samples, and  $t$  is the value based on the t-distribution and related to the number of samples taken. The subscript  $\nu$  is the degrees of freedom and the subscript  $C$  is the confidence (in our case 95%). This can give a basic repeatability uncertainty for the recorded values.

In addition to repeatability uncertainty, there are also other factors that should be included in the overall uncertainty. This includes precision of the measurement equipment and sensors and errors tied to background noise, hysteresis, linearity and other common sources of uncertainty. Each of these factors can be determined and are combined using standard analysis as shown below [74].

$$u_t = \sqrt{(u_r^2 + u_1^2 + \dots + u_n^2)} \quad (27)$$

where the r subscript relates to the repeatability uncertainty, the n subscript represents any number of other uncertainties sources.

Often times, the ultimate metric of interest in experiments is something computed from separate independent signals from different sensors. The functional dependence of this metric on those signals is key in quantifying the propagation of uncertainty. Based on the accepted definition, the variances can be combined using the following expression:

$$S = \sqrt{\left(S_{x_1} \frac{\partial f(x)}{\partial x_1}\right)^2 + \left(S_{x_2} \frac{\partial f(x)}{\partial x_2}\right)^2 + \dots + \left(S_{x_n} \frac{\partial f(x)}{\partial x_n}\right)^2} \quad (28)$$

If we follow the assumption that the data is a Gaussian or normal distribution (as is the assumption with most data collection systems), the variables are independent and uncorrelated, Eq. (28) can be cast in terms of uncertainty instead of variance according to the following:

$$u = \sqrt{\left(u_{x_1} \frac{\partial f(x)}{\partial x_1}\right)^2 + \left(u_{x_2} \frac{\partial f(x)}{\partial x_2}\right)^2 + \dots + \left(u_{x_n} \frac{\partial f(x)}{\partial x_n}\right)^2} \quad (29)$$

This means that, in order to understand the overall uncertainty, all we must know is the uncertainty of the variables that make up the function that we are trying to analyze. An example of this analysis is provided in the next section for the vorticity plots computed from the 2D PIV velocity fields.

## B.2 PIV UNCERTAINTY

Determining the scope of the uncertainty related to the PIV measurements is important as, at times, we can be dealing with flow that may be hard to control and thus inconsistent or with data collection instruments that may not have a high enough precision. In many of the images found in this work, there are areas that show some small amount of vorticity. It is important to determine whether these sections are the result of some actual vorticity in the flow caused by the turbulent flow field or if it is simply a product of the noise inherent in the PIV data collection and analysis process.

Determining this uncertainty begins with Eq. (29). Using a central differencing scheme to approximate each of the partial derivatives of the vorticity expression, the following is the result:

$$\Omega = \frac{U_{y_W} - U_{y_E}}{2\Delta x} - \frac{U_{x_S} - U_{x_N}}{2\Delta y} \quad (30)$$

Therefore, the vorticity calculation for each location within the domain is a function of its neighboring velocity values (north, south, east and west velocities). The uncertainty propagation equation is then applied, resulting in the uncertainty expression shown below:

$$u_{\Omega} = \sqrt{\frac{u_{y_W}^2}{4(\Delta x)^2} + \frac{u_{y_E}^2}{4(\Delta x)^2} + \frac{u_{x_N}^2}{4(\Delta y)^2} + \frac{u_{x_S}^2}{4(\Delta y)^2}} \quad (31)$$

Eq. (31) can be applied to finding both the precision and repeatability error, which can then be combined using the square root of the sum of the squares. Figure 66 presents a comparison of the vorticity and velocity field (Figure 66 (a)) and the corresponding uncertainty field due to the repeatability error (Figure 66 (b)). This uncertainty was gathered by finding the standard deviation for each velocity component from a total of 50 separate velocity fields. The flow field

used was the y-z plane at  $x = -2$  mm with a phase of 135 degrees. As previously noted, the curl is found using a central difference scheme provided in Matlab. Consistent with other theoretical and numerical work [75], the location of highest uncertainty corresponds to the actual vortex location.

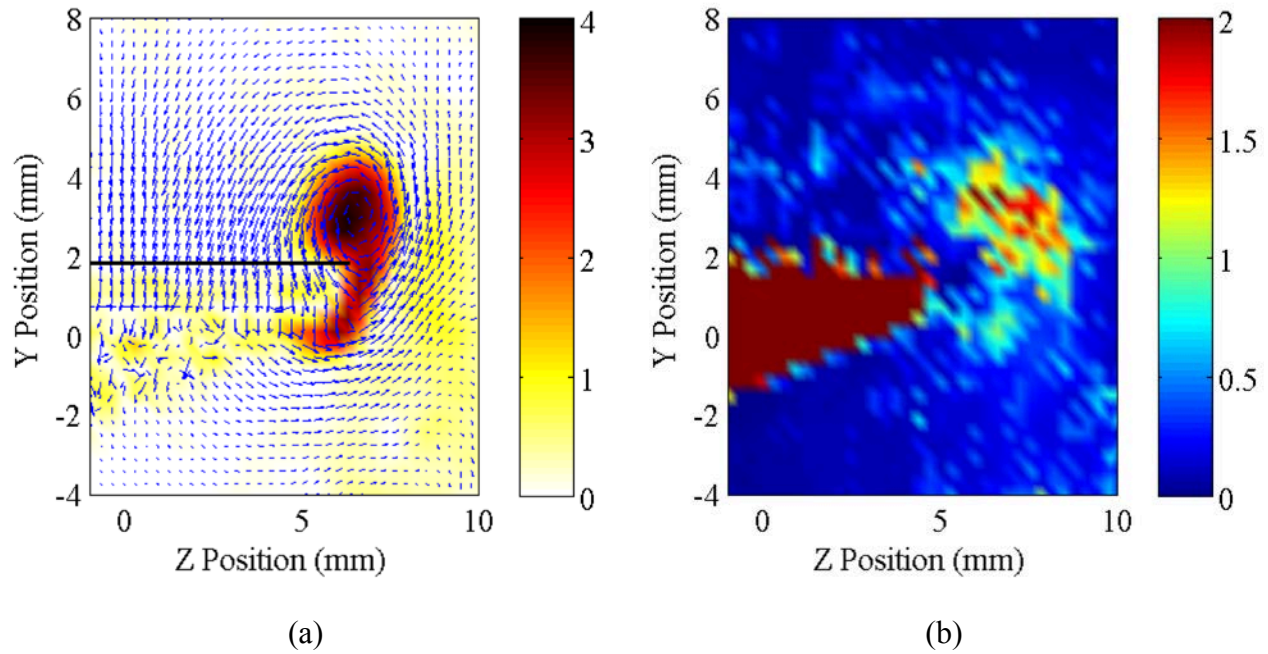


**Figure 66: Comparison of the repeatability uncertainty (b) to the vorticity (a) in the  $x = -2$  mm velocity field.**

**The both of the colorbars have units of 1/s indicating vorticity.**

Additionally, the region that has the low magnitude vorticity has uncertainties that range from 0.1 to 0.5 1/s. When compared to the vorticity magnitude in that area, this can be a significant contributing factor. Since the uncertainty is on the same order, or in some cases larger than the actual vorticity, this confirms that the uncertainty inherent in the PIV analysis generates the numerical noise seen in many of the experimental vorticity fields.

The equipment precision error is also a concern when faced with errant vorticity that has a small magnitude. If we were to consider the manufacturer's stated nominal uncertainty of 7%

for each velocity field and combined it with the average velocity field used in Figure 66, we would get the following uncertainty map (Figure 67(b)).

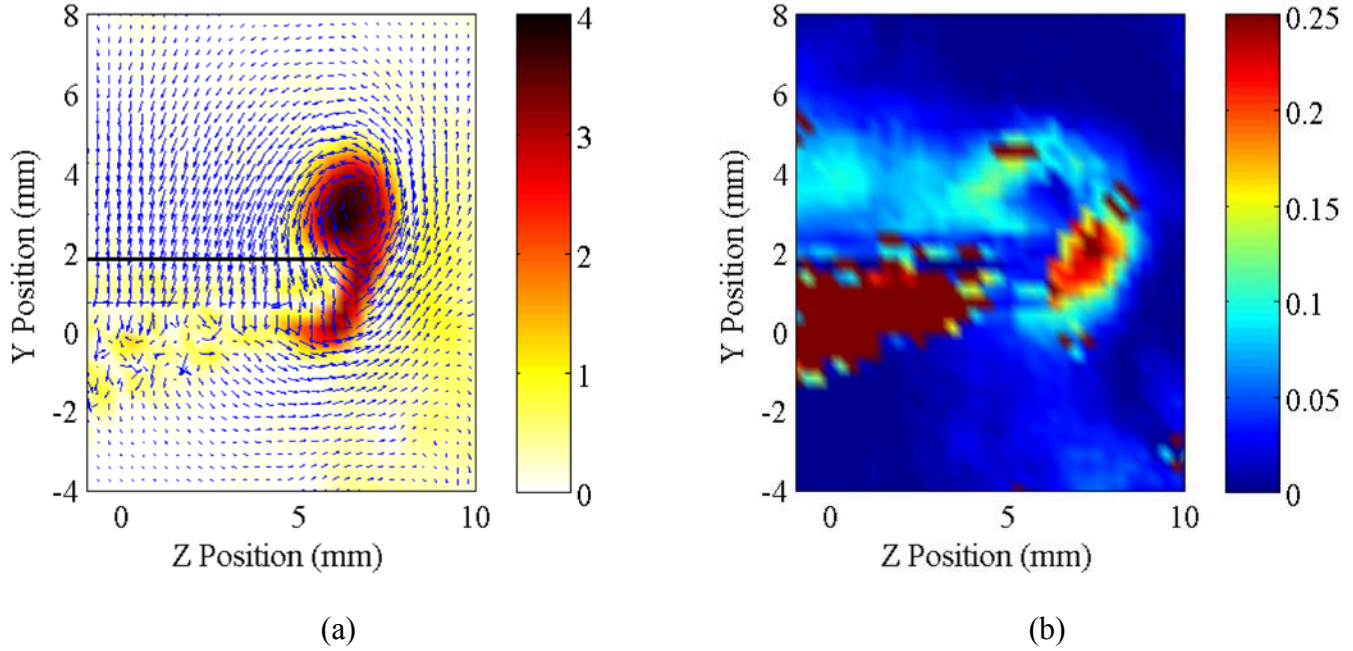


**Figure 67: Comparison of the precision error (b) to the vorticity (a) in the  $x = -2$  mm velocity field. The both of the colorbars have units of  $1/s$  indicating vorticity.**

It is apparent when comparing Figure 66 (b) and Figure 67(b) that the magnitude of the repeatability error is, on a whole higher than the precision error. It can also be seen in Figure 67(b) that the highest uncertainty is concentrated near the tip of the fan.

The two sources of error can be combined by applying the square root to the sum of the squares. Presenting this in the form of an image map, we get Figure 68. It is apparent that repeatability is the most dominant source of error.

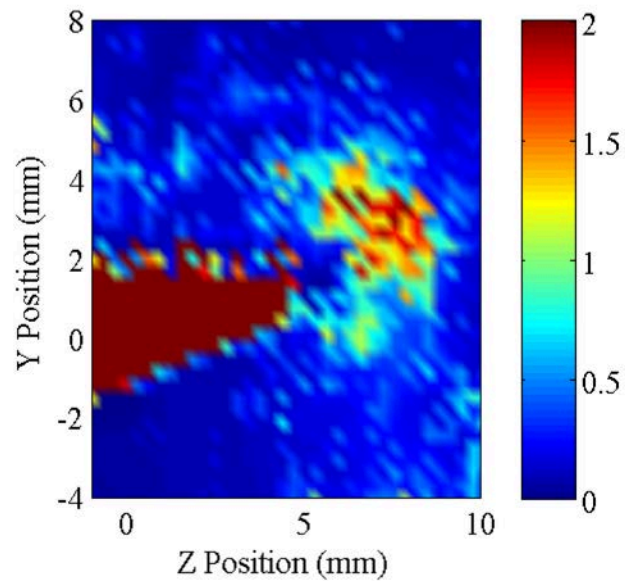


**Figure 68:** The representation of the combined repeatability and precision error in the  $x = -2$  mm velocity field. The colorbar has units of  $1/s$  indicating vorticity.

## BIBLIOGRAPHY

1. Warrick, D.R., B.W. Tobalske, and D.R. Powers, *Aerodynamics of the Hovering Hummingbird*. Nature, 2005. **435**: p. 1094-1097.
2. Ramamurti, R. and W.C. Sandberg, *A Three-Dimensional Computational Study of the Aerodynamic Mechanisms of Insect Flight*. The Journal of Experimental Biology, 2002. **205**: p. 1507-1518.
3. Weis-Fogh, T. and M. Jensen, *Biology and Physics of Locust Flight. I. Basic Principles in Insect Flight. A Critical Review*. Philosophical Transactions of the Royal Society of London. Series B, Biological, 1956. **239**(667): p. 415-458.
4. Koehl, M.A.R. and M.A. Reidenbach, *Swimming by Microscopic Organisms in Ambient Water Flow*. Experiments in Fluids, 2007. **43**: p. 755-768.
5. Lighthill, M.J., *Hydromechanics of Aquatic Propulsion*. Annual Review of Fluid Mechanics, 1969. **1**: p. 413-446.
6. Sfakiotakis, M., D.M. Lane, and B.C. Davies, *Review of Fish Swimming Modes for Aquatic Locomotion*. Journal of Oceanic Engineering, 1999. **24**(2): p. 237-252.
7. Dabiri, J.O., *On the Estimation of Swimming and Flying Forces from Wake Measurements*. The Journal of Experimental Biology, 2005. **208**: p. 3519-3532.
8. Epps, B.P. and A.H. Techet, *Impulse Generated During Unsteady Maneuvering of Swimming Fish*. Experiments in Fluids, 2007. **43**: p. 691-700.
9. Cisneros, L.H., et al., *Fluid Dynamics of Self-Propelled Microorganisms, From Individuals to Concentrated Populations*. Experiments in Fluids, 2007. **43**: p. 737-753.
10. Hughes, G.M., *The Co-Ordination of Insect Movements III. Swimming in Dytiscus, Hydrophilus, and a Dragonfly Nymph*. The Journal of Experimental Biology, 1958. **35**(3): p. 567-583.
11. Edd, J., et al., *Biomimetic Propulsion for a Swimming Surgical Micro-Robot*, in *IEEE/RSJ Intelligent Robotics and Systems Conference* 2003: Las Vegas, Nevada.

12. Tan, G.-K., G.-X. Shen, and S.-Q. Huang, *Investigation of Flow Mechanism of a Robotic Fish Swimming by Using Flow Visualization Synchronized with Hydrodynamic Force Measurement*. Experiments in Fluids, 2007. **43**: p. 811-821.
13. Zhang, Y., et al., *Development of an Underwater Oscillatory Propulsion System Using Shape Memory Alloy*, in *International Conference on Mechatronics and Automation* 2005: Niagara Falls, Canada. p. 1878-1883.
14. Yu, J., et al., *Development of a Biomimetic Robotic Fish and Its Control Algorithm*. IEEE Transactions of Systems, Man, and Cybernetics - Part B: Cybernetics, 2004. **34**(4): p. 1798-1810.
15. Morgansen, K.A., T.M.L. Fond, and J.X. Zhang, *Agile Maneuvering for Fin-Actuated Underwater Vehicles*, in *Second International Symposium on Communications, Control and Signal Processing* 2006: Marrakech, Morocco. p. 1-4.
16. Low, K.H., et al. *Initial prototype design and investigation of an undulating body by SMA*. in *Automation Science and Engineering, 2006. CASE'06. IEEE International Conference on*. 2006. IEEE.
17. Whittlesey, R.W., S. Liska, and J.O. Dabiri, *Fish Schooling as a Basis for Vertical Axis Wind Turbine Farm Design*. Bioinspiration and Biomimetics, 2010. **5**(3): p. 1-6.
18. Vatanabe, S.L., et al., *Design and Characterization of a Biomimetic Piezoelectric Pump Inspired on Group Fish Swimming Effect*. Journal of Intelligent Material Systems and Structures, 2009. **21**: p. 133-147.
19. Tyell, E.D., *Do Trout Swim Better than Eels? Challenges for Estimating Performance Based on the Wake of Self-Propelled Bodies*. Experiments in Fluids, 2007. **43**: p. 701-712.
20. Triantafyllou, M.S., G.S. Triantafyllou, and D.K.P. Yue, *Hydrodynamics of Fishlike Swimming*. Annual Review of Fluid Mechanics, 2000. **32**: p. 33-53.
21. Triantafyllou, M.S., A.H. Techet, and F.S. Hover, *Review of Experimental Work in Biomimetic Foils*. IEEE Journal of Oceanic Engineering, 2004. **29**(3): p. 585-594.
22. Kosa, G., M. Shoham, and M. Zaaroor, *Propulsion Method for Swimming Microrobots*. IEEE Transactions on Robotics, 2007. **23**(1): p. 137-150.
23. Behkam, B. and M. Sitti, *Design Methodology for Biomimetic Propulsion of Miniature Swimming Robots*. 2004 ASME International Mechanical Engineering Congress and Exposition, 2006. **128**: p. 36-43.
24. Schouveiler, L., F.S. Hover, and M.S. Triantafyllou, *Performance of Flapping Foil Propulsion*. Journal of Fluids and Structures, 2005. **20**: p. 949-959.



25. Anderson, J.M., et al., *Oscillating Foils of High Propulsive Efficiency*. Journal of Fluid Mechanics, 1998. **360**: p. 41-72.
26. Read, D.A., F.S. Hover, and M.S. Triantafyllou, *Forces on Oscillating Foils for Propulsion and Maneuvering*. Journal of Fluids and Structures, 2003. **17**: p. 163-183.
27. Young, J. and J.C.S. Lai, *Mechanisms Influencing the Efficiency of Oscillating Airfoil Propulsion*. AIAA Journal, 2007. **45**(7): p. 1695-1702.
28. Heathcote, S., D. martin, and I. Gursul, *Flexible Flapping Airfoil Propulsion at Zero Freestream Velocity*. AIAA, 2004. **42**(11): p. 2196-2204.
29. Shinjo, N. and G.W. Swain, *Use of a Shape Memory Alloy for the Design of an Oscillatory Propulsion System*. IEEE Journal of Oceanic Engineering, 2004. **29**(3): p. 750-755.
30. Garner, L.J., et al., *Development of a Shape Memory Alloy Actuated Biomimetic Vehicle*. Smart Material Structures, 2000. **9**: p. 673-683.
31. Rediniotis, O.K., et al., *Development of a Shape-Memory-Alloy Actuated Biomimetic Hydrofoil*. Journal of Intelligent Material Systems and Structures, 2002. **13**: p. 35-49.
32. Suleman, A. and C. Crawford, *Design and Testing of a Biomimetic Tuna Using Shape Memory Alloy Induced Propulsion*. Computers and Structures, 2008. **86**: p. 491-499.
33. Gupta, A.K., et al., *Anomalous Resonance in a Nanomechanical Biosensor*. Proceedings of the National Academy of Sciences of the United States of America, 2006. **103**: p. 13362-13367.
34. Binnig, G., C.F. Quate, and C. Gerber, *Atomic Force Microscope*. Physical Review Letters, 1986. **56**(9): p. 930-933.
35. Hetrick, R.E., *Vibrating Cantilever Mass Flow Sensor*. Sensors and Actuators A, 1990. **21-23**: p. 373-376.
36. Boskovic, S., et al., *Rheological Measurements Using Microcantilevers*. Journal of Rheology, 2002. **46**: p. 891-899.
37. Toda, M. and S. Osaka, *Vibrational Fan Using Piezoelectric Polymer PVF<sub>2</sub>*. Proceedings of the IEEE, 1979. **67**(8): p. 1171-1173.
38. Yorinaga, M., et al. *A Piezoelectric Fan Using PZT Ceramics*. in *5th Meeting of Ferroelectric Materials and Their Applications*. 1985. Kyoto, Japan.
39. Sheu, W.-J., R.-T. Huang, and C.-C. Wang, *Influence of bonding glues on the vibration of piezoelectric fans*. Sensors and Actuators A, 2008. **148**(1): p. 7.

40. Yao, K. and K. Uchino, *Analysis on a composite cantilever beam coupling a piezoelectric bimorph to an elastic blade*. Sensors and Actuators A, 2001. **89**(3): p. 7.
41. Ergin, A. and B. Ugurlu, *Linear Vibration Analysis of Cantilever Plates Partially Submerged in Fluid*. Journal of Fluids and Structures, 2003. **17**: p. 927-939.
42. Kimber, M., et al., *Pressure and Flow Rate Performance of Piezoelectric Fans*. IEEE Transactions on Components and Packaging Technologies, 2009. **32**(4): p. 766-775.
43. Kimber, M., S.V. Garimella, and A. Raman. *An Experimental Study of Fluidic Coupling Between Multiple Piezoelectric Fans*. in *Thermal and Thermomechanical Phenomena in Electronics Systems, 2006. ITherm'06. The Tenth Intersociety Conference on*. 2006. IEEE.
44. Ihara, A. and H. Watanabe, *On the flow around flexible plates, oscillating with large amplitude*. Journal of Fluids and Structures, 1994. **8**(7): p. 19.
45. Kimber, M., R. Lonergan, and S.V. Garimella, *Experimental Study of Aerodynamic Damping in Arrays of Vibrating Cantilevers*. Journal of Fluids and Structures, 2009. **25**: p. 1334-1347.
46. Shoemaker, M.W., *Performance Analysis of the Air Moving Capabilities of Piezoelectric Fan Arrays*, in *Mechanical Engineering 2011*, University of Illinois at Urbana-Champaign: Urbana, Illinois. p. 64.
47. Yoo, J.H., J.I. Hong, and W. Cao, *Piezoelectric ceramic bimorph coupled to thin metal plate as cooling fan for electronic devices*. Sensors and Actuators A, 2000. **79**(1): p. 8-12.
48. Acikalin, T., et al., *Experimental Investigation of the Thermal Performance of Piezoelectric Fans*. Heat Transfer Engineering, 2004. **25**(1): p. 4-14.
49. Acikalin, T., et al., *Characterization and Optimization of the Thermal Performance of Miniature Piezoelectric Fans*. International Journal of Heat and Fluid Flow, 2007. **28**: p. 806 - 820.
50. Wait, S.M., et al., *Piezoelectric Fans Using Higher Flexural Modes for Electronics Cooling Applications*. IEEE Transactions on Components and Packaging Technologies, 2007. **30**(1): p. 119-128.
51. Kimber, M. and S.V. Garimella, *Measurement and Prediction of the Cooling Characteristics of a Generalized Vibrating Piezoelectric Fan*. International Journal of Heat and Mass Transfer, 2009. **52**(19-20): p. 4470-4478.
52. Kim, Y.H., S.T. Wereley, and C.-H. Chun, *Phase-resolved flow field produced by a vibrating cantilever plate between two endplates*. Physics of Fluids, 2004. **16**(1): p. 145-162.

53. Choi, M., C. Cierpka, and Y.-H. Kim, *Vortex Formation by a Vibrating Cantilever*. Journal of Fluids and Structures, 2012. **31**: p. 76-78.
54. Kim, Y.H., C. Cierpka, and S.T. Wereley, *Flow Field Around a Vibrating Cantilever: Coherent Structure Education by Continuous Wavelet Transform and Proper Orthogonal Decomposition*. Journal of Fluid Mechanics, 2011. **669**: p. 584-606.
55. Acikalin, T., A. Raman, and S.V. Garimella, *Two-dimensional streaming flows induced by resonating thin beams*. Journal of the Acoustical Society of America, 2003. **114**(4 I): p. 11.
56. Bidkar, R., et al., *Nonlinear Aerodynamic Damping of Sharp-Edged Flexible Beams Oscillating at Low Keulegan-Carpenter Numbers*. Journal of Fluid Mechanics, 2009. **634**: p. 269-289.
57. Keulegan, G.H. and L.H. Carpenter, *Forces of Cylinders and Plates in an Oscillating Fluid*. Journal of Research of the National Bureau of Standards, 1958. **60**: p. 423-440.
58. Clemons, L., H. Igarashi, and H. Hu, *An Experimental Study of Unsteady Vortex Structures in the Wake of a Piezoelectric Flapping Wing*, in *48th AIAA Aerospace Sciences Meeting Including the New Horizon Forum and Aerospace Exposition* 2010: Orlando, Florida. p. 1-13.
59. Peterson, S.D., M. Porfiri, and A. Rovardi, *A Particle Image Velocimetry Study of Vibrating Ionic Polymer Metal Composites in Aqueous Environments*. IEEE/ASME Transactions on Mechatronics, 2009. **14**(4): p. 474-483.
60. Krueger, P.S., *The Significance of Vortex Ring Formation and Nozzle Exit Over-Pressure to Pulsatile Jet Propulsion*, in *Aeronautics* 2001, California Institute of Technology: Pasadena. p. 234.
61. Dabiri, J.O. and M. Gharib, *Delay of vortex ring pinchoff by an imposed bulk counterflow*. Physics of Fluids, 2004. **16**(4): p. 3.
62. Dabiri, J.O., *Optimal Vortex Formation as a Unifying Principle in Biological Propulsion*. Annual Review of Fluid Mechanics, 2009. **41**: p. 17-33.
63. Chung, H.-C., et al., *Coupled piezoelectric fans with two degree of freedom motion for the application of flapping micro aerial vehicles*. Sensors and Actuators A, 2008. **147**(2): p. 607-612.
64. Ming, A., et al., *Development of Underwater Robots Using Piezoelectric Fiber Composite*, in *2009 IEEE International Conference on Robotics and Automation* 2009: Kobe, Japan. p. 3821-3826.
65. Mukherjee, S. and R. Ganguli, *A Comparative Study of Dragonfly Inspired Flapping Wings Actuated by Single Crystal Piezoceramic*. Smart Structures and Systems, 2010. **10**(1): p. 67-87.

66. Fish, F.E. and G.V. Lauder, *Passive and Active Flow Control by Swimming Fishes and Mammals*. Annual Review of Fluid Mechanics, 2006. **38**: p. 193-224.
67. Lauder, G.V., et al., *Locomotion with Flexible Propulsors: I. Experimental Analysis of Pectoral Fin Swimming in Sunfish*. Bioinspiration & Biomimetics, 2006. **1**: p. S25-S34.
68. Ellenrieder, K.D. and S. Pothos, *PIV Measurements of the Asymmetric Wake of a Two Dimensional Heaving Hydrofoil*. Experiments in Fluids, 2008. **44**: p. 733-745.
69. Eastman, A. and M. Kimber, *Flow Field Analysis of a Single Piezoelectric Fan*, in *ASME 2009 International Mechanical Engineering Congress and Exposition 2009*, ASME: Lake Buena Vista, Florida. p. 1429-1436.
70. Eastman, A., J. Kiefer, and M. Kimber, *Thrust Measurements and Flow Field Analysis of a Piezoelectrically Actuated Oscillating Cantilever*. Experiments in Fluids, 2012. **53**(5): p. 1533-1543.
71. Eastman, A. and M. Kimber, *Aerodynamic Damping of Sidewall Bounded Oscillating Cantilevers*. Journal of Fluids and Structures, 2014. **(In Review)**.
72. Jones, M.A., *The Separated Flow of an Inviscid Fluid Around a Moving Flat Plate*. Journal of Fluid Mechanics, 2003. **496**: p. 405 - 441.
73. Jordan, T., et al. *Electrical properties and power considerations of a piezoelectric actuator*. in *MRS Proceedings*. 1999. Cambridge Univ Press.
74. Figliola, R.S., D.E. Beasley, and R.S. Figliola, *Theory and Design for Mechanical Measurements* 1995, New York: Wiley.
75. Etebari, A. and P.P. Vlachos, *Improvements of the Accuracy of Derivative Estimation from DPIV Velocity Measurements*. Experiments in Fluids, 2005. **39**: p. 1040-1050.